Master Thesis of Science

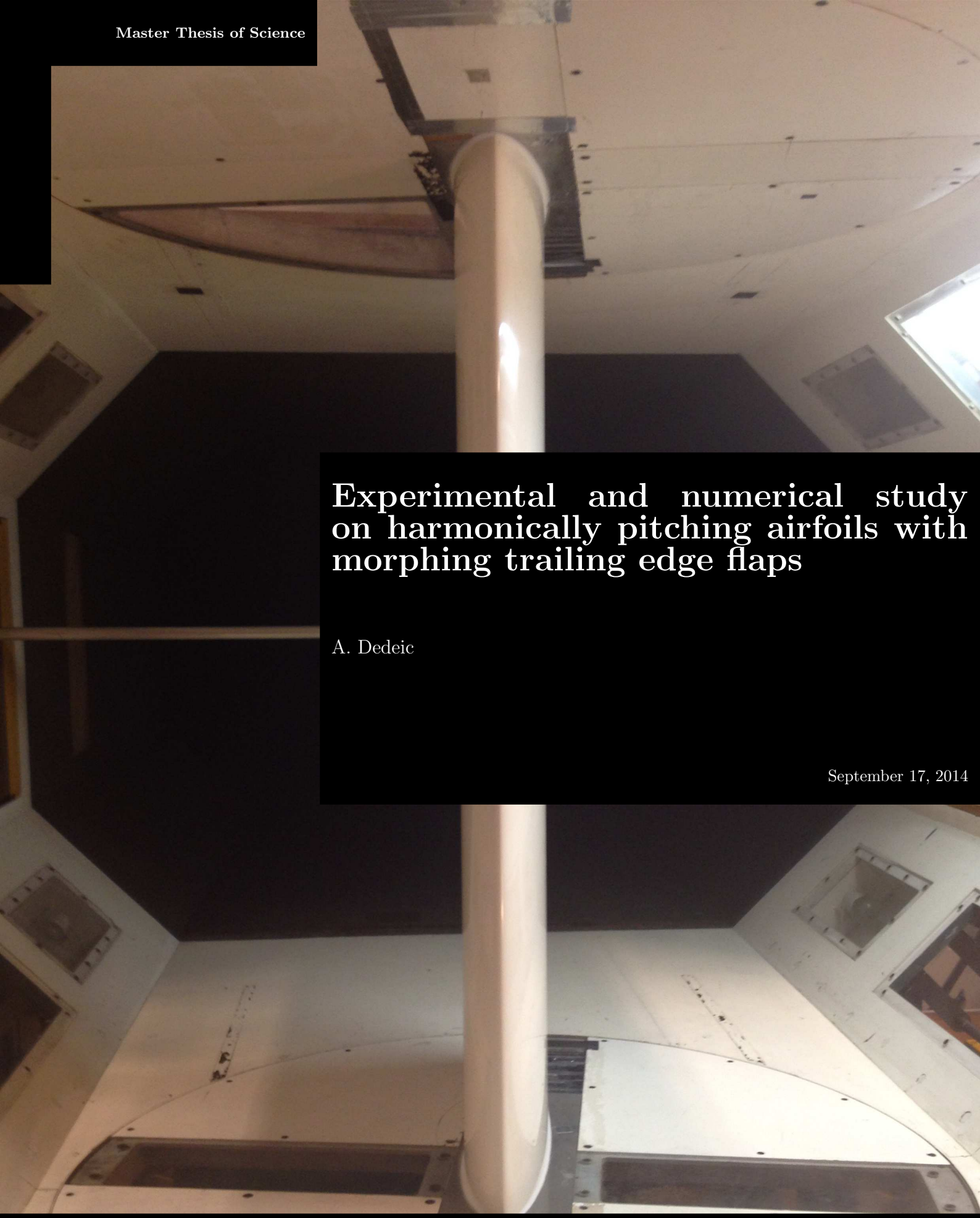

Experimental and numerical study on harmonically pitching airfoils with morphing trailing edge flaps

A. Dedeic

September 17, 2014

European Wind Energy Master - EWEM- Rotor Design Track

Experimental and numerical study on harmonically pitching airfoils with morphing trailing edge flaps

Master of Science Thesis

For obtaining the degree of Master of Science in
Aerospace Engineering at Delft University of Technology and
Wind Energy at Technical University of Denmark

A. Dedeic

September 17, 2014

European Wind Energy Master - EWEM
Delft University of Technology
Denmark Technical University

European Wind Energy Master - EWEM
Of
Rotor Design Track

The undersigned hereby certify that they have read and recommend to the European Wind Energy Master - EWEM for acceptance a thesis entitled **"Experimental and numerical study on harmonically pitching airfoils with morphing trailing edge flaps"** by **A. Dedeic** in partial fulfillment of the requirements for the degree of **Master of Science**.

Dated: September 17, 2014

Supervisor: _____
Dr.ir. C.J. Simão Ferreira of TU Delft

Supervisor: _____
Prof.dr.ir J.N Sørensen of DTU

Reader: _____
ir. T. Gillebaart of TU Delft

Reader: _____
Prof.dr. G.J.W. van Bussel of TU Delft

Abstract

The main objective of this thesis is to contribute to the existing knowledge of unsteady flow effects over airfoils. This is done by first obtaining experimental wind tunnel data for a harmonically pitching airfoil and for an oscillating trailing edge flap. Additionally, the goal is to validate two numerical methods by means of comparing them to the experimentally obtained wind tunnel data. The unsteady pressure measurements are conducted in two different wind tunnels using two airfoils and two motion types. The used numerical methods are a viscous-inviscid interaction code [4] and the computational fluid dynamics solver OpenFOAM.

A theoretical background on the basis of the two numerical methods is presented first. Next the experimental methodology is described for both measurement campaigns with different types of wind tunnels, airfoils and motions. Then a more model-specific and in depth discussion of the two models is given, highlighting that the viscous-inviscid model uses a Lagrangian description of the flow whilst the CFD model, in principle, approaches the flow from a Eulerian point of view.

The results focus on the unsteady lift loops and the comparison between experimental and numerical data. The unsteady pitching airfoil motion at $Re = 4.2 \cdot 10^5$ was well captured by Q^{3}UIC but OpenFOAM had more difficulties in successfully capturing the flow behaviour around the stall angle of attack.
The flap measurements at $Re = 10^6$ showed more satisfying outcomes in the case of OpenFOAM. Apart from a steady-state offset, the loops are all captured accurately. Only at the highest angle of attack of 18° the results show some dissimilarities due to large separation regions and the shedding of many vortices into the wake.
Q^{3}UIC shows good results for the lower angle of attack range, but around the stall angle of attack, attached and separated flow conditions are not simulated accurately with respect to the measurements. The OpenFOAM results only consist of boundary layer simulations where transition is forced. A fully working free transition model can not be implemented until the forced transition model is validated, which is also part of this study.

Acknowledgements

My time as a student at TU Delft has been a challenging and exciting time. From my first year which I started in September 2007 until today seven years have passed. I will not easily forget the many things I have learned and all the people I have met. In this final phase of my study, the past nine months were mostly dedicated to this paper in front of you.

I want to acknowledge the main characters – who also happen to be my supervisors – that made this possible, Carlos Simão Ferreira and Jens Nørkær Sørensen. Thank you for giving me the opportunity to perform this interesting study.
My direct supervisors Thijs Gillebaart and Néstor Ramos García deserve a big thank you. Without them I would have been nowhere. They provided me with a lot of help and advice during all the struggles I have faced with my simulations. For setting up the experimental campaigns I would like to thank Stefan Bernardy and Robert Mikkelsen.

Apart from the academic staff my gratitude goes out to my friends and family for supporting me during this period. In particular room 2.15, Lukas Kuijken and Kumayl Sarwar, it would be a much lonelier journey without you guys. I still do wonder who Kees is. Also I would like to thank Bram Lof for the OpenFOAM discussions and Dieter Castelein for the occasional stop by at the office. Additionally I would like to thank Martijn Rosenstok for helping me out in the last two weeks, and especially the last night before the deadline. My final thanks goes out to my sister, Aida Kristina Dedeic for proofreading this thesis, which was quite a challenge considering her philosophical background.

Delft, The Netherlands — A. Dedeic
September 17, 2014

Contents

Abstract **v**

Acknowledgements **vii**

List of Figures **xv**

List of Tables **xvii**

List of Symbols **xix**

1 Introduction **1**

1.1 Morphing wings 1

1.2 Motivation and objectives 2

1.3 Methodology and thesis outline 3

2 Theoretical background **5**

2.1 Velocity potential and vortex flow 5

2.2 Unsteady aerodynamics and dynamic stall 6

2.3 Viscous flow 9

2.4 Boundary layer equations and transition process 10

2.5 Kutta condition 13

2.6 Navier-Stokes 14

2.6.1 Governing equations 15

2.6.2 RANS 17

3 Experimental methods **19**
3.1 DTU measurements on a pitching airfoil . . . 19
3.1.1 NACA 64-418 . . . 19
3.1.2 Open-return wind tunnel . . . 21
3.1.3 Instrumentation . . . 22
3.1.4 Test cases . . . 23
3.2 TU Delft measurements on a morphing flap . . . 26
3.2.1 DU 95-W-180 . . . 26
3.2.2 Low-Speed Low-Turbulence Wind Tunnel (LTT) . . . 26
3.2.3 Instrumentation . . . 27
3.2.4 Test cases . . . 28

4 Numerical methods **31**
4.1 Q^3UIC – Lagrangian approach . . . 31
4.1.1 Theory . . . 31
4.1.2 Structure and solving procedure . . . 32
4.1.3 Flap deflection . . . 34
4.1.4 Inputs . . . 34
4.2 OpenFOAM – Eulerian approach . . . 36
4.2.1 Theory and turbulence models . . . 36
4.2.2 Model specific inputs . . . 38
4.2.3 Mesh topology and deformation due to flap deflection . . . 38
4.2.4 Mesh independence . . . 38
4.2.5 Turbulent inflow parameters . . . 40
4.2.6 Time step . . . 41

5 Results – Pitching airfoil **43**
5.1 Experimental results of the NACA 64-418 airfoil . . . 43
5.1.1 Steady measurements . . . 43
5.1.2 Unsteady measurements . . . 45
5.2 Simulations . . . 45
5.2.1 Convergence study . . . 50
5.2.2 Steady results . . . 53
5.2.3 Unsteady results . . . 58
5.3 Conclusive remarks . . . 59

6 Results – Morphing flap **67**
6.1 Experimental results of the DU 95-W-180 airfoil . . . 67
6.1.1 Steady measurements . . . 67
6.1.2 Unsteady measurements . . . 68
6.2 Simulations . . . 76
6.2.1 Convergence study . . . 76
6.2.2 Steady results . . . 78
6.2.3 Unsteady results . . . 79
6.3 Conclusive remarks . . . 87

7 Conclusions and recommendations **89**
7.1 Conclusions 89
7.2 Recommendations 92

Bibliography **93**

A Free LTT flap measurements at $\alpha = 10^\circ$ **97**

List of Figures

2.1 Dynamic and static lift coefficients. 7
2.2 Dynamic stall explained [5]. 8
2.3 Displacement thickness δ^* [2]. 10
2.4 Relation between shape factor, displacement thickness and momentum thickness [3]. 11
2.5 Boundary layer transition process [2]. 12
2.6 Pressure gradients and resulting velocity profiles [3]. 12
2.7 Kutta condition for finite TE angle and cusped TE [1]. 13
2.8 Bound airfoil circulation and starting vortex being shed into the wake [2]. 14

3.1 Instrumentation inside of the wing: pressure scanners, flap linear motor, and tubing. 20
3.2 NACA 64-418 airfoil showing the pressure tab distribution located at a span wise position of 45%. 20
3.3 Closed wing as used during measurements. 20
3.4 Layout and dimensions of wind tunnel in meters [6]. 21
3.5 Experimental set-up DTU wind tunnel. 22
3.6 Servomotor motion translated to $\alpha(t)$ benchmarked against a sine function. 24
3.7 Trip wires used to force an early boundary layer transition at $x/c \approx 5\%$. . 24
3.8 Trailing edge flap and servo motor on the DU 95-W-180 experimental model. 26
3.9 LTT characteristics and components [7]. 27
3.10 Experimental set-up LTT. 28

4.1 Airfoil surface discretisation in panels using cosine distribution. 32
4.2 Linear and polynomial flap deflections [6]. Q^3UIC uses linear deflection for unsteady flap motion. 35

4.3 Mesh deformation at maximum flap deflection. 39
4.4 Determination of suitable mesh using Richardson extrapolation. 40

5.1 NACA 64-418, measured steady lift polars for free and tripped transition. 44
5.2 Experimental $C_l(\alpha)$ for $\alpha = 0°$, $\Delta\alpha = 4°, 8°$, $k = 0.0314, 0.0628$. Forced transition left and free transition right. 46
5.3 Experimental $C_l(\alpha)$ for $\alpha = 4°$, $\Delta\alpha = 4°, 8°$, $k = 0.0314, 0.0628$. Forced transition left and free transition right. 47
5.4 Experimental $C_l(\alpha)$ for $\alpha = 8°$, $\Delta\alpha = 4°, 8°$, $k = 0.0314, 0.0628$. Forced transition left and free transition right. 48
5.5 Experimental $C_l(\alpha)$ for $\alpha = 12°$, $\Delta\alpha = 4°, 8°$, $k = 0.0314, 0.0628$. Forced transition left and free transition right. 49
5.6 Sparsity of meshes used for mesh convergence study on NACA 64-418. . . 51
5.7 Values of steady C_y and C_x components for meshes with N $\approx$ [2e4; 4e4; 8e4; ∞] cells. 52
5.8 Steady free boundary layer comparisons between lift, separation and transition. 54
5.9 Pressure coefficient over airfoil for $\alpha = [0°, 4°, 8°, 12°]$ and a free boundary layer transition. 55
5.10 Steady tripped boundary layer comparisons between lift, separation and transition. 56
5.11 Pressure coefficient over airfoil for $\alpha = [0°, 4°, 8°, 12°]$ and a tripped boundary layer transition. 57
5.12 Experimental and numerical $C_l(\alpha)$ for $\alpha = 0°$, $\Delta\alpha = 4°, 8°$, $k = 0.0314, 0.0628$. Forced transition left and free transition right. 60
5.13 Experimental and numerical $C_l(\alpha)$ for $\alpha = 4°$, $\Delta\alpha = 4°, 8°$, $k = 0.0314, 0.0628$. Forced transition left and free transition right. 61
5.14 Experimental and numerical $C_l(\alpha)$ for $\alpha = 8°$, $\Delta\alpha = 4°, 8°$, $k = 0.0314, 0.0628$. Forced transition left and free transition right. 62
5.15 Experimental and numerical $C_l(\alpha)$ for $\alpha = 12°$, $\Delta\alpha = 4°, 8°$, $k = 0.0314, 0.0628$. Forced transition left and free transition right. 63
5.16 All NACA 64-418 steady polars and effect of the wall correction in Q^3UIC. 64
5.17 Steady and unsteady pressure distributions around 14-15 degrees. 65
5.18 Pressure, velocity and turbulent kinetic energy fields for NACA 64-418 case at $\alpha_m = 8°$, $\alpha_A = 8°$ and $k = 0.0628$. 66

6.1 Lift and drag steady polars, forced and free transition. $Re = 10^6$. 68
6.2 Experimental $C_l(\beta)$ for $\alpha = 0°, \Delta\beta = 5°$, $k = 0.01, 0.05$ and 0.10. 70
6.3 Experimental $C_l(\beta)$ for $\alpha = 0°, \Delta\beta = 10°$, $k = 0.01, 0.05$ and 0.10. 71
6.4 Experimental $C_l(\beta)$ for $\alpha = 8°, \Delta\beta = 5°$, $k = 0.01, 0.05$ and 0.10. 72
6.5 Experimental $C_l(\beta)$ for $\alpha = 8°, \Delta\beta = 10°$, $k = 0.01, 0.05$ and 0.10. 73
6.6 Experimental $C_l(\beta)$ for $\alpha = 18°, \Delta\beta = 5°$, $k = 0.01, 0.05$ and 0.10. 74
6.7 Experimental $C_l(\beta)$ for $\alpha = 18°, \Delta\beta = 10°$, $k = 0.01, 0.05$ and 0.10. 75

6.8 Sparsity of meshes used for the convergence study. 77
6.9 Values of steady C_y and C_x components for meshes with N = [5248; 13446; 48522; ∞] $\sim 1/\sqrt{N}$=[0.0138, 0.0086, 0.0045, 0]. 77
6.10 Entire mesh of 48522 cells and a more detailed view of trailing edge region. 77
6.11 Flap angles and corresponding mesh deformation in OpenFOAM. 78
6.12 Steady lift polars free and forced transition combined. Numerical and experimental. 79
6.13 Experimental and numerical $C_l(\beta)$ for $\alpha = 0°, \Delta\beta = 5°$, $k = 0.01, 0.05$ and 0.10. 81
6.14 Experimental and numerical $C_l(\beta)$ for $\alpha = 0°, \Delta\beta = 10°$, $k = 0.01, 0.05$ and 0.10. 82
6.15 Experimental and numerical $C_l(\beta)$ for $\alpha = 8°, \Delta\beta = 5°$, $k = 0.01, 0.05$ and 0.10. 83
6.16 Experimental and numerical $C_l(\beta)$ for $\alpha = 8°, \Delta\beta = 10°$, $k = 0.01, 0.05$ and 0.10. 84
6.17 Experimental and numerical $C_l(\beta)$ for $\alpha = 18°, \Delta\beta = 5°$, $k = 0.01, 0.05$ and 0.10. 85
6.18 Experimental and numerical $C_l(\beta)$ for $\alpha = 18°, \Delta\beta = 10°$, $k = 0.01, 0.05$ and 0.10. 86

A.1 $C_l(\beta)$ for $\alpha = 10°, \Delta\beta = 5°$ and 10°, $k = 0.01, 0.05$ and 0.10. $Re = 10^6$ . . 98

List of Tables

2.1 Flow states as function of reduced frequency. 9

3.1 Steady test cases NACA 64-418. 25
3.2 Unsteady test cases, NACA 64-418 pitch measurements. 25
3.3 LTT characteristics and dimensions. 27
3.4 Unsteady test cases, DU 95-W-180 flap measuerements. 29

4.1 Richardson extrapolation to find C_y value for a mesh with an infinite number of cells. 40
4.2 Mesh size and percentage difference between the different meshes and final extrapolated C_y value. 40

5.1 Q^3UIC main inputs parameters. 50
5.2 Mesh variables NACA 64-618 used for convergence study in Pointwise. . . 52

6.1 Mesh variables DU 95-W-180 used for convergence study in Pointwise. . . 76
6.2 Time steps used for DU 95-W-180 simulations. 78

List of Symbols

Latin Symbols

b	Semi-chord	[m]
b	Wing span	[m]
c	Chord	[m]
C_d	Drag coefficient	[–]
C_f	Skin friction coefficient	[–]
C_l	Lift coefficient	[–]
C_m	Moment coefficient	[–]
Co	Courant number	[–]
C_p	Pressure coefficient	[–]
C_x	Horizontal force coefficient	[–]
C_y	Vertical force coefficient	[–]
$\mathbf{F}$	Force vector	[N]
f	Frequency	[Hz]
H	Shape factor	[–]
h	Step size in Richardson extrapolation	[–]
k	Reduced frequency	[–]
k	Turbulent kinetic energy	$[\mathrm{m^2\,s^{-2}}]$
L	Length scale	[m]
L'	Lift per unit span	$[\mathrm{N\,m^{-1}}]$
$\mathbf{n}$	Normal vector	[–]
p	Local static pressure	$[\mathrm{N\,m^{-2}}]$

p_∞	Free stream static pressure	$[\mathrm{N\,m^{-2}}]$
R	Specific gas constant	$[\mathrm{J\,mol^{-1}\,K^{-1}}]$
Re	Reynolds number	[–]
S_f	Face surface area normal	$[\mathrm{m^2}]$
St	Strouhal number	[–]
t	Time	[s]
$\mathbf{u}$	Flow velocity vector	$[\mathrm{m\,s^{-1}}]$
u, v, w	Boundary layer velocities	$[\mathrm{m\,s^{-1}}]$
u_e	Boundary layer edge velocity	$[\mathrm{m\,s^{-1}}]$
u_{ind}	Body induced velocity	$[\mathrm{m\,s^{-1}}]$
u_{mean}	Reynolds averaged mean velocity	$[\mathrm{m\,s^{-1}}]$
u_{rms}	Root mean square of turbulent velocity fluctuations	$[\mathrm{m\,s^{-1}}]$
u_w	Wake induced velocity	$[\mathrm{m\,s^{-1}}]$
U_P	Velocity at any point P	$[\mathrm{m\,s^{-1}}]$
U_∞	Free stream velocity	$[\mathrm{m\,s^{-1}}]$
$\mathbf{V}$	General velocity vector	$[\mathrm{m\,s^{-1}}]$
w_T	Transpiration velocity	$[\mathrm{m\,s^{-1}}]$

Greek Symbols

α	Angle of attack	[°]
α_A	Pitch amplitude around mean angle of attack	[°]
α_m	Mean angle of attack	[°]
β	Flap angle	[°]
Γ	Circulation	$[\mathrm{m^2\,s^{-1}}]$
δ	Boundary layer thickness	[m]
δ^*	Displacement thickness	[m]
ε	Turbulence dissipation	$[\mathrm{m^2\,s^{-3}}]$
θ	Momentum thickness	[m]
μ	Dynamic viscosity	$[\mathrm{kg\,m^{-1}\,s^{-1}}]$
ν	Kinematic viscosity	$[\mathrm{m^2\,s^{-1}}]$
φ	Phase shift	[rad]
Φ	Velocity potential	[–]
ρ	Air density	$[\mathrm{kg\,m^{-3}}]$
τ_w	Wall shear stress	$[\mathrm{N\,m^{-2}}]$
ω	Angular frequency	$[\mathrm{rad\,s^{-1}}]$
ω	Specific turbulence dissipation	$[\mathrm{s^{-1}}]$

$\boldsymbol{\Omega}$	Vorticity	$[s^{-1}]$

Abbreviations

ALE	Arbitrary Lagrangian–Eulerian
BL	Boundary Layer
CFD	Computational Fluid Dynamics
CFL	Cournat-Friedrichs-Lewy
DES	Detached Eddy Simulation
DGCL	Discrete Geometric Conservation Law
DNS	Direct Numerical Simulation
DTU	Danmarks Tekniske Universitet
LES	Large Eddy Simulation
LE	Leading edge
NACA	National Advisory Committee for Aeronautics
NS	Navier-Stokes
PDE	Partial Differential Equation
PIMPLE	Merged PISO–SIMPLE algorithm
PISO	Pressure Implicit with Splitting of Operators
RANS	Reynolds-Averaged Navier-Stokes
RBF	Radial Basis Function
SIMPLE	Semi–Implicit Method for Pressure–Linked Equations
SST	Shear Stress Transport
TE	Trailing edge
TI	Turbulence Intensity
TU Delft	Delft University of Technology
UAV	Unmanned Aerial Vehicle
URANS	Unsteady Reynolds-Averaged Navier-Stokes

Chapter 1

Introduction

This introductory chapter gives a short background of the thesis topic at hand. A motivation on why this study is undertaken is outlined together with a description of the main objectives and the methodology that is used. At the end, a detailed overview is given on the structure of this thesis where all the chapters are addressed.

1.1 Morphing wings

Birds have the ability to continuously adapt their wings into the most efficient and effective form that satisfies a large range of flight conditions [8]. Unfortunately, this smooth and seamless form adaptation can not be found in many contemporary aircraft wings or rotor blades. The vast majority of these large scale structures is rigid. On a smaller scale though, in the world of UAV's for instance, the number of potential morphing technologies is larger due to the lower aerodynamic loads that act on the structure [9]. Through millions of years of evolution, nature has had the chance to optimise bird flight to a great extent. In that respect it is not surprising that engineers and designers would like to reproduce bird-like wings as closely as possible. However, due to technical incapabilities this is not yet entirely possible.
The use of conventional flaps, or control surfaces such as ailerons or elevators, has proven to work well throughout history and is therefore applied globally with great success [10]. The ease and simplicity of this system is part of its success. In the past, this solution has been chosen because early technologies did not provide the means to design and manufacture complete morphing wings on large scale. This is where complications arise, which are mainly structural problems as described in [11]. In the field of small scale UAV's, morphing wings are widely applied due to the low weight, ease of small scale production, simple control mechanisms and smart materials [12]. On a larger scale, the penalty of weight and size rises and the challenge of how to implement morphing into these large structures becomes apparent [13].

The benefits of morphing structures are numerous and are therefore analysed extensively with many ongoing research projects. In contrast to multi element airfoils, trailing edge flaps with morphing configurations do not have the benefits of e.g. the fresh boundary layer effect or the circulation effect. These effects are commonly found in multi element airfoils [10]. An important disadvantage of multi element airfoils however, is that with the increase in lift also a substantial drag rise occurs, reducing the low lift to drag ratio of the airfoil. This disadvantage is not present with morphing flaps because the entire airfoil consists of a single element capable of assuming various configurations. With the technological advancements of today and more to come in the future, it is becoming increasingly more attainable to reproduce morphing wings as they occur in nature, more closely.

In the wind energy sector, morphing wings, or in this study, wings with a morphing trailing edge flap region, can be used to reduce loads and vibrations caused by turbulent inflow of the wind velocity field. A harmonically oscillating flap can act in phase or out of phase with the wind to cancel out, or reduce unwanted loads and vibrations. By doing so in the long run, the lifetime of the blades and of the turbine as a whole can be extended since there is less exposure to fatigue loads and less stress on vital internal parts such as bearings, shafts and components of the electrical system.

1.2 Motivation and objectives

Technologies, like many other things, evolve over time. In this study, the effects of unsteady flow on morphing airfoils, in particular in the trailing edge region, are addressed. As this morphing manner of shape adaptation is key to improved aerodynamic and structural characteristics of airfoils, the relevance and motivation to investigate airflows experimentally and numerically, arises. For wind turbine applications, flexible trailing edges can be used to reduce the loads and vibrations on the rotor blades. For aircraft and automotive applications, the possibilities of morphing aerodynamic structures can even be applied more extensively.
The main research question of this project is stated as follows:

> How accurate are existing numerical/ computational tools in predicting aerodynamic behaviour of harmonically pitching airfoils with a seamlessly morphing trailing edge flap region?

With subquestions:

- Where do the numerical models differ the most from the experiments and what are the most likely causes for this difference?
- How can the discrepancies between simulations and experiments be reduced?

In order to answer these questions the primary objective of this thesis is to:

> Contribute to the existing knowledge of unsteady effects over airfoils by performing wind tunnel measurements on a harmonically pitching airfoil and an oscillating trailing edge flap. With these results, the validity and accuracy of two numerical models is examined.

Given the motivation, research questions and objectives, and previous studies related to this topic, a clear idea becomes visible on why a continuation on this study is relevant. For instance in [14], a comparison is drawn between different simulation methods, but without an experimental validation. The present study also includes the latter.

1.3 Methodology and thesis outline

Having given the general project description, it is now stated how to go about setting up the experiments, which variables are of interest and how everything should be monitored, processed and analysed.

The theoretical framework of this project consists of a combination of different approaches. First the researcher is familiarised with the fundamental theories of morphing and pitching airfoils and unsteady flow, together with the newest trends in numerical approaches that simulate aerodynamic behaviour of airfoils. Use is made of a computational model that goes by the name of Q^3UIC, designed and written by Ramos García [4]. This is a panel method based on the viscous-inviscid interaction of the flow and is used for the analysis of unsteady flow around the pitching airfoil. To run this code the programming language Fortran is used, together with Matlab to analyse the wind tunnel data and combine and compare the data between the two. Alongside the viscous-inviscid model, CFD simulations are performed using the open source CFD tool OpenFOAM. These numerical methods are discussed in more detail in Chapter 4.

Alongside the two numerical tools described above, this study consists of experimentally obtained data from wind tunnel measurements at Denmark Technical University (DTU) and TU Delft. Both experimental campaigns are performed using pressure measurements, a detailed description of the wind tunnel experiments can be found in Chapter 3.

Before the experimental set up and results are discussed, this thesis starts with a theoretical background of Q^3UIC and OpenFOAM, in Chapter 2. After all the needed information is provided, the results of both experiments and simulations are provided and analysed in Chapters 5 and 6. Finally this study ends with conclusions and recommendations for future work in Chapter 7.

Chapter 2

Theoretical background

The theory in this chapter serves as an introduction to the physics of the numerical models described in Chapter 4. A short overview of the theoretical basis behind concepts as velocity potential and the relation between circulation and lift is presented. Unsteady flow characteristics are described subsequently with a short discussion on dynamic stall. Next, a discussion on viscous flow is given including a description of the boundary layer and the unsteady Kutta condition. Finally a brief discussion is given on the general theory behind the Navier-Stokes equations and Computational Fluid Dynamics.

2.1 Velocity potential and vortex flow

The continuity equation states that for incompressible flow, the relation $\nabla \cdot \mathbf{V} = 0$ holds. If, in addition to that, the flow is inviscid and irrotational, it follows that the circulation per unit area, or vorticity is zero: $\boldsymbol{\Omega} = \nabla \times \mathbf{V} = 0$. Such a flow is characterised by the velocity potential Φ, stating that the velocity at some point can be obtained as the gradient of the velocity potential.

$$\nabla\Phi = \mathbf{V} \tag{2.1}$$

Combining (2.1) and the expressions above, it is shown that the velocity potential satisfies Laplace's equation:

$$\nabla^2\Phi = 0, \tag{2.2}$$

which is a statement of the incompressible continuity equation for an irrotational fluid. The velocity field for an incompressible inviscid irrotational flow can be obtained by solving Laplace's equation for the velocity potential. In order to do so, an important

boundary condition is imposed forcing the velocity component normal to the body surface to be zero.

$$\nabla\Phi \cdot \mathbf{n} = 0 \tag{2.3}$$

An additional boundary condition states that in the far field, as the distance r goes to infinity $r \to \infty$, the influence that the moving body exerts on the flow tends to zero.

$$\lim_{r\to\infty} \nabla\Phi = 0 \tag{2.4}$$

The two-dimensional velocity potential for a source flow can be defined as an integration of the separate source strengths along a path.

$$\Phi(x, y) = \int_a^b \frac{\lambda ds}{2\pi} \ln r, \tag{2.5}$$

where a and b are the start and end point of the integration path, s the path location and λ the source strength per unit length.

In order to create lift, there has to be circulation. The total circulation Γ around a closed contour and over any surface is given by:

$$\Gamma = -\oint_C V ds = -\iint_S (\nabla \times V)\, dS \tag{2.6}$$

This expression relates circulation to vorticity using Stoke's theorem. For vortex flow, which is irrotational at every point except the origin where the vorticity approaches infinity, the strength of a vortex sheet per unit length can be defined as $\gamma = \gamma(s)$. In this case the circulation is expressed by:

$$\Gamma = \int_a^b \gamma ds \tag{2.7}$$

Following from this expression, the total lift per unit span is obtained using the Kutta-Joukowsky theorem:

$$L' = \rho_\infty V_\infty \Gamma \tag{2.8}$$

This theorem shows the direct proportionality between lift and circulation.

2.2 Unsteady aerodynamics and dynamic stall

A harmonic motion of a pitching airfoil is an example of a body immersed in an unsteady flow. The aerodynamic properties change with every time step as the position of the airfoil is continuously shifting. Unsteady aerodynamics can be divided into two parts:

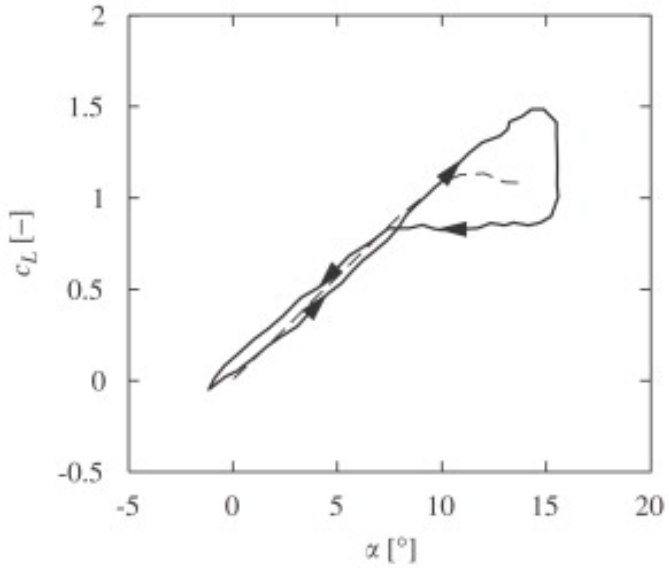

Figure 2.1: *Dynamic and static lift coefficients.*

the Theodorsen effect and dynamic stall [15]. Very basically the Theodorsen effect can be described as a delayed lift effect in conditions of attached flow, and dynamic stall, a delayed lift effect during separated flow.
In the attached flow region, during the up-stroke of a pitching airfoil, a lower lift than in the static case is experienced because the flow is delayed and requires some time to reach the new steady state value. In the down-stroke, the opposite effect occurs, leading to higher lift values than in the static case, as is shown in the left, counter clock-wise loop of Figure 2.1.
The dynamic stall direction of the lift behaviour is opposite to that of the Theodorsen effect. Here the direction of the loop is clock-wise see Figure 2.1, experiencing higher lift for increasing angle of attack in the up-stroke and lower lift in the down-stroke. This is because not only the air loads are delayed, but also the separation point, which has an opposite delayed effect on the lift. The suction effect of a growing vortex is generally the cause of higher lift values for increasing angles of attack. After the vortex has reached past the trailing edge and the flow fully separates, lift values drop below the static case. In contrast to steady static stall, dynamic stall is influenced by a larger range of parameters, making it more difficult to model and analyse [16].

A rapid change in angle of attack can lead to the formation of a separation bubble where a vortex is being formed at the leading edge and the flow reattaches again due to adverse pressure gradients not being strong enough to maintain separated flow. As α increases, the adverse pressure gradient grows, pushing the flow reattachment point downstream towards the trailing edge. This vortex creates an additional lift until it reaches the trailing edge, after which it is shed into the wake, causing an abrupt decrease in lift. After a low enough angle of attack is reached, the flow reattaches and the loop starts over again. This process is visualised in Figure 2.2.

In steady flow, the velocity at any point U_p, is composed of the free stream velocity U_∞ and the body induced velocity u_{ind}. For unsteady flow an additional term u_w is added,

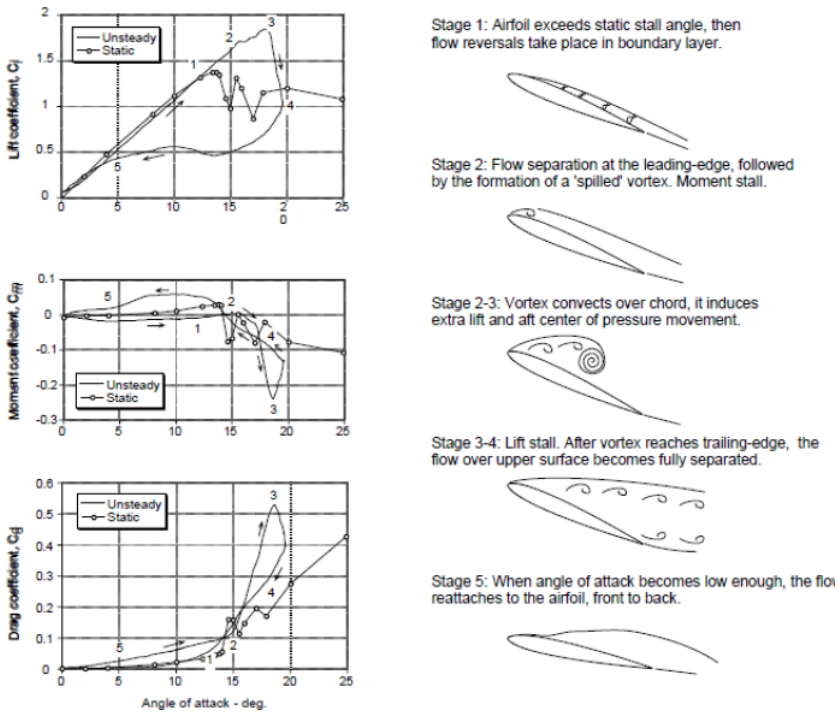

Figure 2.2: *Dynamic stall explained [5].*

representing the influence of the wake.

$$U_p = U_\infty + u_{ind} + u_w \tag{2.9}$$

The wake influence is most pronounced at the trailing edge region of the airfoil and its strength is strongly dependent on the frequency of the body movement. Higher frequencies result in increased unsteady effects characterised by a larger size of, for instance the $C_l(\alpha)$ loops.

An important quantity that is commonly used to describe the motion is the reduced frequency k. It is derived from the angular frequency ω, in the harmonic equation of motion for the angle of attack.

$$\alpha = \alpha_m + \alpha_A \cdot \sin(\omega t - \varphi), \tag{2.10}$$

where α_m is the mean angle of attack, α_A the amplitude and φ the phase shift. The relation between angular frequency and reduced frequency gives the final expression for k.

$$k = \frac{\omega b}{U_\infty} = \frac{2\pi f b}{U_\infty} = \frac{\pi f c}{U_\infty}, \tag{2.11}$$

where $b = c/2$ is the semi-chord. The reduced frequency is often used as a measure to define the steadiness of a flow as shown in Table 2.1.

Too high frequencies will often result in rapid and large differences in circulation between panels and large pressure distributions between upper and lower airfoil surface. In some

Table 2.1: *Flow states as function of reduced frequency.*

Flow type	**Range**
Steady	$k = 0$
Quasi-steady	$0 < k \leq 0.05$
Unsteady	$0.05 < k \leq 0.2$
Highly unsteady	$k \geq 0.2$

numerical models this can eventually lead to a slow numerical convergence. That is to say, if a converging solution is to be reached, there is a limit to which the frequency of the harmonic airfoil movement can be increased as the influence of the wake grows and the addition of viscous effects are added into the potential flow model [4].

2.3 Viscous flow

Viscosity plays an important role close to a body surface and is intrinsically related to the Reynolds number:

$$Re = \frac{\rho U_\infty c}{\mu} = \frac{U_\infty c}{\nu}, \tag{2.12}$$

where μ and ν are the dynamic and kinematic viscosities respectively. Their relation to each other is given by by the air density ρ through $\nu = \frac{\mu}{\rho}$. c is a length scale, which in this study is the chord of the airfoil, and U_∞ the free stream velocity of the flow. The Reynolds number is a non dimensional quantity defined by the ratio of inertial and viscous forces. From (2.12), by looking at the ratio, it can be deduced that for low velocities the relative importance of the viscous forces increases. This is the case close to the body surface where frictional forces are present.
The way in which the boundary layer behaves is highly influenced by the Reynolds number. As Re increases, viscous effects become less important and the boundary layer thickness decreases. In result, due to the thinner boundary layer, the onset of separation is delayed. An increase in Re also leads to a build-up of laminar instabilities and strong adverse pressure gradients. This then results in advancement of the transition to a turbulent boundary layer.

Figure 2.3 illustrates the displacement thickness δ^* as being part of the boundary layer thickness δ. Looking at the relation between inviscid and viscous flow, δ^* is the distance by which streamlines are shifted from the surface to obtain the same flow rates for both types of flow.

A decrement in mass flow due to the presence of the boundary layer is a possible interpretation of the displacement thickness which is described mathematically by the relation below.

$$\delta^* = \int_0^\delta \left(1 - \frac{u}{u_e}\right) dy \tag{2.13}$$

, where u is the boundary layer velocity and u_e the BL edge velocity. A measure for the loss of momentum of the viscous flow due to presence of the boundary layer is defined

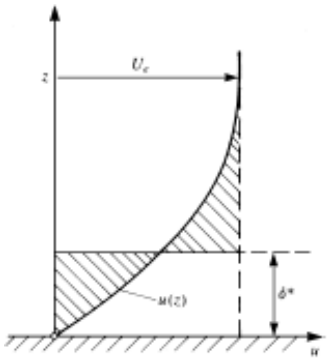

Figure 2.3: *Displacement thickness δ^* [2].*

by the momentum thickness θ. It is also related to the integral drag of a surface and the rate of increase can be seen as a measure for the local skin friction.

$$\theta = \int_0^\delta \frac{u}{u_e}\left(1 - \frac{u}{u_e}\right) dy \tag{2.14}$$

The shape factor provides information about the nature of the flow and is defined as the ratio between the displacement and momentum thickness. Inserting Equations (2.13) and (2.14) into this ratio yields:

$$H = \frac{\delta^*}{\theta} = \frac{\int_0^\delta \left(1 - \frac{u}{u_e}\right) dy}{\int_0^\delta \frac{u}{u_e}\left(1 - \frac{u}{u_e}\right) dy} = \int_0^\delta \frac{u}{u_e} dy \tag{2.15}$$

Where low values of H are representative for turbulent boundary layers and higher values are found in laminar boundary layers. The boundary layer thickness δ does not have an influence on the shape factor, its value is solely based on the displacement and momentum thickness. A visualisation of the relation between these quantities is shown in Figure 2.4.

The wall shear stress, that is significantly higher for turbulent than for laminar flow is given by:

$$\tau_w = \mu \frac{\partial u}{\partial y} \tag{2.16}$$

A higher wall shear stress means that close to the surface, the gradient of the velocity profile $\partial u/\partial y$ is steeper than for a laminar one.

2.4 Boundary layer equations and transition process

The Navier-Stokes (NS) equations (2.17) are capable of describing general fluid motion in great detail, but at the same time they are time demanding to solve for a sufficient accuracy. The two-dimensional boundary layer equations for steady incompressible flow,

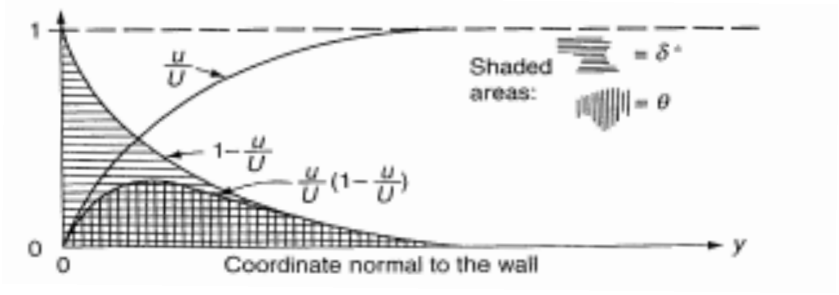

Figure 2.4: *Relation between shape factor, displacement thickness and momentum thickness [3].*

are a simplification of the NS-equations. A more detailed discussion on the NS-equations is given in Section 2.6.

$$\rho' u' \frac{\partial u'}{\partial x'} + \rho' v' \frac{\partial u'}{\partial y'} = -\frac{1}{\gamma_h M_\infty^2} \frac{\partial p'}{\partial x'} + \frac{1}{Re} \frac{\partial}{\partial y'} \left[\mu' \left(\frac{\partial v'}{\partial x'} + \frac{\partial u'}{\partial y'} \right) \right], \tag{2.17}$$

where a prime $'$ denotes that the variable is non-dimensionalised, i.e. $\rho' = \dfrac{\rho}{\rho_\infty}$.
After some simplifications and rearrangements, the two-dimensional boundary layer equations are outlined in (2.18), assuming $\delta \ll c$, and large Reynolds numbers in the order of $Re = 1/\delta^2$.

$$\begin{aligned} \text{Continuity}: \quad & \rho \frac{\partial u}{\partial x} + \rho \frac{\partial v}{\partial y} && = 0 \\ \text{x–momentum}: \quad & \rho u \frac{\partial u}{\partial x} + \rho v \frac{\partial u}{\partial y} && = -\frac{dp}{dx} + \frac{\partial}{\partial y} \left(\mu \frac{\partial u}{\partial y} \right) \\ \text{y–momentum}: \quad & \frac{\partial p}{\partial y} && = 0 \end{aligned} \tag{2.18}$$

The boundary conditions imposed at the surface and at the boundary layer edge state that

$$\text{At surface}: \quad y = 0 \qquad u = 0 \qquad v = 0 \tag{2.19}$$

$$\text{At boundary layer edge}: \quad y = \infty \qquad u = u_e \tag{2.20}$$

The region close to the body surface is viscous and is governed by the simplified NS–equations which are parabolic rather than elliptic as in the full version. This classification follows from the form of standard second-order PDE's:

$$a u_{xx} + b u_{xy} + c u_{yy} = f(x, y; u_x, u_y), \tag{2.21}$$

where the mathematical character of the equations is determined by the determinant $D = b^2 - 4ac$:

$$b^2 - 4ac = \begin{cases} < 0 & \text{elliptic} \\ = 0 & \text{parabolic} \\ > 0 & \text{hyperbolic} \end{cases} \tag{2.22}$$

Because of this parabolic nature, there is no upstream influence, meaning the boundary layer development is determined in downstream direction from an initial station.

A weakness of the classical boundary layer computations is that there is a singularity near separation named after Goldstein, caused by the stable parabolic direction of the equations which changes in reversed flow regions. For mild separation and moderate angles of attack, this singularity can be overcome by applying a strong interaction through transpiration velocity between the inner viscous and the outer inviscid flow [4].

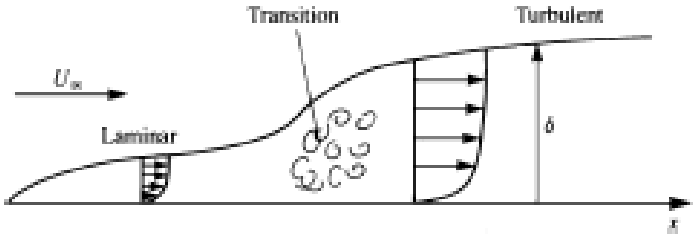

Figure 2.5: *Boundary layer transition process [2].*

A boundary layer usually starts off laminar with streamlines parallel to the surface. Changes in stream-wise position on a body surface, an increase in Reynolds number or surface roughness and pressure gradients can result in the flow becoming increasingly unstable. This is where the laminar flow transitions into a turbulent state, where shear stresses and skin friction are high. The flow is turbulent once the transition point is passed, see Figure 2.5. Upstream of this point the flow is treated as laminar, despite the instability waves of the boundary layer, because they do not affect the mean flow until after the transition point.
In some cases it is desirable to maintain laminar flow because of lower skin friction drag values. On the other hand, turbulent flow has the advantage of keeping the flow attached to the surface longer, which delays the onset of separation and a dramatic increase in pressure drag. It depends on the application which flow type is preferred. In glider aircraft, wings are made extremely smooth to maintain laminar flow as long as possible and hence reduce skin friction drag. In the case of, for example, a golf or tennis ball, turbulent flow is preferred because separation is delayed, resulting in a narrower wake and lower pressure drag.

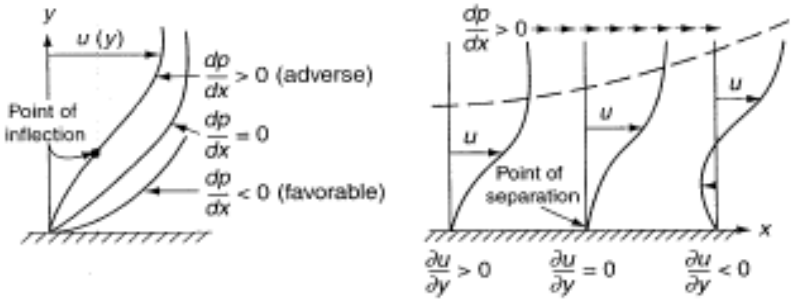

Figure 2.6: *Pressure gradients and resulting velocity profiles [3].*

When adverse pressure gradients become too large, the flow starts to reverse direction, leading to flow separation, see Figure 2.6. Due to their chaotic nature where mixing

is facilitated, turbulent boundary layers are better in transferring energy at the edge between inner and outer flow, preventing the flow from separating.

2.5 Kutta condition

The Kutta condition in short can be summarised by two basic statements. First, it is stated that the flow must leave the trailing edge (TE) smoothly. The second statement depends on the shape of the TE. For a finite TE angle, the tangential upper and lower surface velocities must be zero at the TE. Because physically, there can be no two different velocities with different directions at the same point. So for a finite angle, the trailing edge is a stagnation point. If, on the other hand, the trailing edge is cusped, the upper and lower velocities are equal and finite and leave the trailing edge smoothly parallel to each other as shown in Figure 2.7.

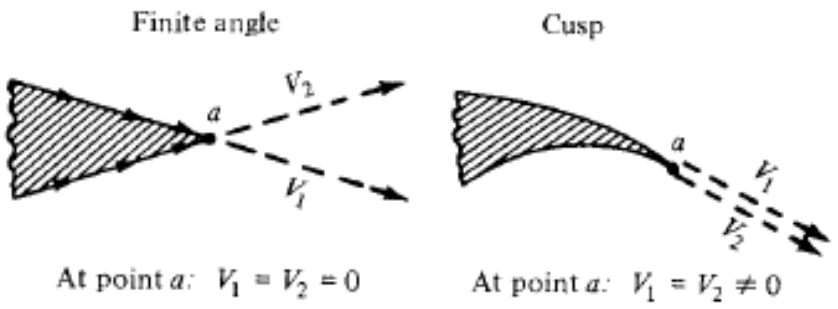

Figure 2.7: *Kutta condition for finite TE angle and cusped TE [1].*

When the flow leaves the airfoil at the trailing edge, a starting vortex is generated which is a measure for the lift as defined by the Kutta-Joukowsky theorem in (2.8). The Kutta condition expressed in pressure difference and vortex sheet strength at the trailing edge yields:

$$\Delta p(TE) = 0 \qquad \text{and} \qquad \gamma(TE) = 0 \tag{2.23}$$

For unsteady flow however, the condition $\Delta p(TE) = 0$ does not hold. In order to maintain zero loading at the trailing edge, a starting vortex is shed into the wake which is equal and opposite in sign to the change in bound vorticity on the airfoil as shown in Figure 2.8.

A discussion on the unsteady Kutta condition is given in [17], where it is stated that for panel methods, a proper Kutta condition specification is more important than any other numerical detail [18]. A more detailed discussion on the unsteady Kutta condition and the numerical implementation into Q^{3}UIC is given in Chapter 4.

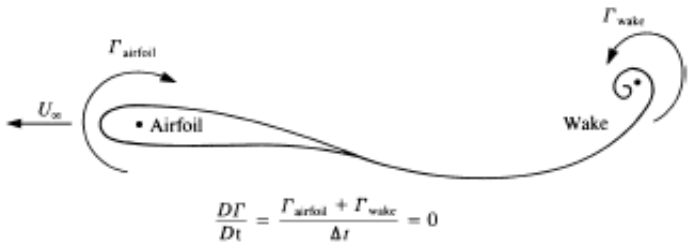

Figure 2.8: *Bound airfoil circulation and starting vortex being shed into the wake [2].*

2.6 Navier-Stokes

This section first focusses on the governing equations that describe fluid motion and then discusses the model that is used for solving the equations. There are basically three ways of solving the NS equations, DNS, LES and RANS. A brief discussion on DNS and LES follows after which RANS is explained in a bit more detail in Section 2.6.2.

DNS

The most accurate and simple way to solve and simulate the NS equations is with Direct Numerical Simulation (DNS). All spatial and temporal scales of turbulence are resolved without the use of turbulence models. The direct nature of this method makes it the most accurate method but also computationally the most expensive. The number of cells is approximated by (2.24), where L is the characteristic length of the biggest turbulent eddy, and η the Kolmogorov length scale.

$$N \approx \left(\frac{L}{\eta}\right)^{\frac{3}{4}} \tag{2.24}$$

Kolmogorov showed that:

$$\frac{L}{\eta} \sim Re^{\frac{3}{4}} \tag{2.25}$$

Following from this, DNS requires a number of mesh points N^3:

$$N^3 = Re^{\frac{9}{4}} \tag{2.26}$$

High Reynolds number flows are not practical to solve because the computational power requirements exceed the capabilities of the most powerful computers that are currently available. Even for low Re simulations, computers that are considered among the most powerful currently available, have their shortcomings.

LES

A bit more manageable method from a computational time point of view, is Large Eddy Simulation (LES). Here a function is used to filter out smaller scales of the solution (sub-grid fluctuations) and to model them while the larger vortices are computed directly. By doing so, the computational time decreases and more complex geometries can be resolved.

Neither of these methods are applicable for this study, mainly because of their computational expense.

2.6.1 Governing equations

A different approach to describe fluid motion around an object is by solving the Navier-Stokes (NS) equations. The common way of solving these complex equations is by using computational fluid dynamics (CFD), an accurate but computationally expensive method.

Conservation laws

The derivation of the Navier-Stokes equations is realised by applying the conservation laws of mass, momentum and energy to a moving fluid:

$$\text{Mass}: \quad \rho\left(\frac{\partial}{\partial t} + \nabla\cdot\mathbf{u}\right) = \quad 0 \tag{2.27}$$

$$\text{Momentum}: \quad \rho\left(\frac{\partial \mathbf{u}}{\partial t} + \nabla\cdot(\mathbf{u}\mathbf{u})\right) = \quad \nabla\sigma \tag{2.28}$$

$$\text{Energy}: \quad \rho\left(\frac{\partial e}{\partial t} + \nabla\cdot(e\mathbf{u})\right) = \quad \nabla\cdot(\sigma\mathbf{u}) - \nabla\mathbf{q} + \rho Q \tag{2.29}$$

Mass conservation follows from the continuity equation and the physical principle that mass can be neither created nor destroyed. Momentum conservation is based on Newton's second law $\mathbf{F} = \frac{d}{dt}(m\mathbf{u}) = m\mathbf{a}$, which in its more general form relies on the principle that force equals the time rate of change of momentum. The body forces are omitted in the momentum equation above. The stress tensor σ represents:

$$\sigma = \begin{bmatrix} \sigma_{xx} & \sigma_{xy} & \sigma_{xz} \\ \sigma_{yx} & \sigma_{yy} & \sigma_{yz} \\ \sigma_{zx} & \sigma_{zy} & \sigma_{zz} \end{bmatrix} \tag{2.30}$$

Finally the conservation of energy entails that energy can change in form but without the possibility of being created or destroyed, known as the first law of thermodynamics. The total specific energy e [$\mathrm{J\,kg^{-1}}$] comes from the more general fluid enthalpy $h = e + \frac{p}{\rho}$, $\mathbf{q}$ [$\mathrm{W\,s^{-1}}$] is the heat flux vector and Q [$\mathrm{J\,m^3\,kg^{-1}}$] the energy generation. The stress tensor defined by normal and viscous stresses on the surface:

$$\sigma = -p\mathbf{I} + \mathbf{T}, \tag{2.31}$$

where $\mathbf{I}$ is the identity matrix and $\mathbf{T}$ the deviatoric stress tensor: $\mathbf{T} = \mathbf{A}(\nabla\mathbf{u})$ with $\mathbf{A}$, being a viscosity tensor. Now $\mathbf{T}$ can be expressed as:

$$\mathbf{T} = 2\mu\mathbf{E} + \mu''\Delta\mathbf{I}, \tag{2.32}$$

where

$$\mathbf{E} = \frac{1}{2}\left(\nabla\mathbf{u} + \nabla\mathbf{u}^T\right) \tag{2.33}$$

is the rate of strain tensor and $\Delta = \nabla \mathbf{u}$ the expansion rate of the flow. Now with $2\mu + 3\mu'' = 0$, the deviatoric stress tensor is expressed as

$$\mathbf{T} = 2\mu \left(\mathbf{E} - \frac{1}{3}\Delta \mathbf{I} \right) \tag{2.34}$$

Finally substituting (2.34) and (2.33) into (2.31) gives the expression for the stress tensor:

$$\begin{aligned} \sigma &= -p\mathbf{I} + \mathbf{T} = -p\mathbf{I} + 2\mu \left(\frac{1}{2} \left(\nabla \mathbf{u} + \nabla \mathbf{u}^T \right) - \frac{1}{3}\Delta \mathbf{I} \right) \\ &= - \left(p + \frac{2}{3}\mu \nabla \mathbf{u} \right) \mathbf{I} + \mu \left(\nabla \mathbf{u} + \nabla \mathbf{u}^T \right) \end{aligned} \tag{2.35}$$

The stress tensor in (2.35) is one of the required constitutive relations to close this set of equations. To close the energy equation, the perfect gas law is used: $p = \rho RT$, and finally Fourier's law relates the heat variables to each other as: $\mathbf{q} = \lambda \nabla T$, where λ [$\mathrm{W\,m^{-1}\,K^{-1}}$] is the heat conductivity.

Incompressible

Considering the airspeed of $25\,\mathrm{m\,s^{-1}}$ used in this study, the Mach number of 0.3 from where flow is assumed compressible, is not reached. This simplifies the NS equations to the unsteady, incompressible form where there is no more need for the energy equation:

$$\nabla \cdot \mathbf{u} = 0 \tag{2.36}$$

$$\overbrace{\underbrace{\frac{\partial \mathbf{u}}{\partial t}}_{\substack{\text{Unsteady} \\ \text{acceleration}}} + \underbrace{\nabla \cdot (\mathbf{u}\mathbf{u})}_{\substack{\text{Convective} \\ \text{acceleration}}}}^{\text{Inertia}} = \overbrace{\underbrace{\nu \nabla^2 \mathbf{u}}_{\text{Viscosity}} - \underbrace{\frac{\nabla p}{\rho}}_{\substack{\text{Pressure} \\ \text{gradient}}}}^{\text{Divergence of stress}} \tag{2.37}$$

Non-dimensional

To reduce the number of parameters and to have better comparing abilities, the next step is to non-dimensionalise the unsteady, incompressible NS-equations. This is done by division of a variable by its reference variable. An example of how the velocity is made dimensionless is shown in (2.38).

$$\mathbf{u}' = \frac{\mathbf{u}}{U_{ref}} \tag{2.38}$$

By doing so for each variable, the dimensionless form of the incompressible, unsteady Navier-Stokes equations is expressed as:

$$\nabla \cdot \mathbf{u}' = 0 \tag{2.39}$$

$$St \frac{\partial \mathbf{u}'}{\partial t} + \nabla(\mathbf{u}'\mathbf{u}') = -\nabla p + \frac{1}{Re} \nabla^2 \mathbf{u}', \tag{2.40}$$

where the dimensionless Strouhal and Reynolds numbers emerge, adjoining the temporal and viscous term respectively.

2.6.2 RANS

Finally, the least expensive but also the least accurate method is the Reynolds-Averaged Navier-Stokes (RANS) equations, where the NS quantities are decomposed into a time-averaged and a fluctuating part.
This simplification leads to additional terms, the so-called apparent, or Reynolds stress components $\rho\overline{u_i' u_j'}$. An option for a closure model is to prescribe the fluid another property: turbulent viscosity. Additionally there is a need to link this to the turbulent kinetic energy and the length scales of turbulence taking into account the flow history.
In order to solve the set of equations, a closure model is needed to account for the transport of turbulent quantities: kinetic energy and the dissipation thereof. There are different models for this, among which the k-ω and k-ε are most common. They represent the turbulent kinetic energy k [$\mathrm{m^2\,s^{-2}}$], the dissipation rate of the turbulent kinetic energy ε [$\mathrm{m^2\,s^{-3}}$] and the specific dissipation ω [$\mathrm{s^{-1}}$]. The turbulent kinetic energy k, is a measure of the kinetic energy per unit mass of the turbulent fluctuations in a flow. The dissipation ε, the rate at which k is converted into thermal energy. And finally the specific dissipation ω indicates at which rate k is converted into thermal energy per unit volume and time, sometimes also referred to as mean frequency of the turbulence.
The relation between these parameters is shown in (2.44) and the turbulence models are discussed in more detail in Section 4.2.1.

$$k = \frac{3}{2}(UI)^2 \tag{2.41}$$

$$\varepsilon = \frac{k^{\frac{3}{2}}}{l} \tag{2.42}$$

$$\omega = \frac{k^{\frac{1}{2}}}{l} \tag{2.43}$$

$$\varepsilon = k^n \omega^m \tag{2.44}$$

where, I the turbulence intensity [$-$] and l the turbulent length scale [m].

Compared to the more accurate DNS and LES models, RANS can fail in proper prediction of the turbulent kinetic energy in the wake region [19].

In short, the choice for the most suitable solver depends heavily on the characteristics of the problem that has to be simulated. In this study the RANS approach is chosen because of its low computational expense.

Chapter 3

Experimental methods

The present chapter describes the experimental methods that are used to study the aerodynamic behaviour of a pitching NACA 64-418 airfoil and a DU 95-W-180 airfoil with a morphing trailing edge flap. The experiments are performed in an open return wind tunnel of DTU Lyngby and a closed return low turbulence wind tunnel at TU Delft.

3.1 DTU measurements on a pitching airfoil

This section gives an overview of the DTU experimental set-up. First, it is described how the wing, wind tunnel and other instrumentation are prepared for testing. Next, a description is given of how the measurements are carried out and which test cases are investigated. Considered are steady and unsteady flow conditions and a free and tripped boundary layer transition for a variety of angles of attack and reduced frequencies.

3.1.1 NACA 64-418

For the experiments, a carbon fibre wing with a NACA 64-418 airfoil is used. The first digit indicates that the airfoil belongs to the NACA 6–series. The chord-wise location of the minimum pressure is 0.4c and is given by the second digit. The design lift coefficient at zero angle of attack is 0.4, shown by the third digit, and the last two digits describe the maximum thickness $t/c = 18\%$.
The wing has a 0.5 m span and a chord of 0.25 m, see Figure 3.3. Prior to the experiments the wing had to be prepared. All pressure tabs, on one end connected to small holes on the suction and pressure sides of the wing, are connected to a designated position on the pressure scanner seen in Figure 3.1. The distribution of the pressure holes which are located at 45% of the wing span is shown in Figure 3.2. The two pressure scanners are connected to a data acquisition system which in turn, is connected to a computer that analyses and processes the data using LabVIEW.

With all the pressure tubes connected, a linear motor to control the flap angle was mounted.

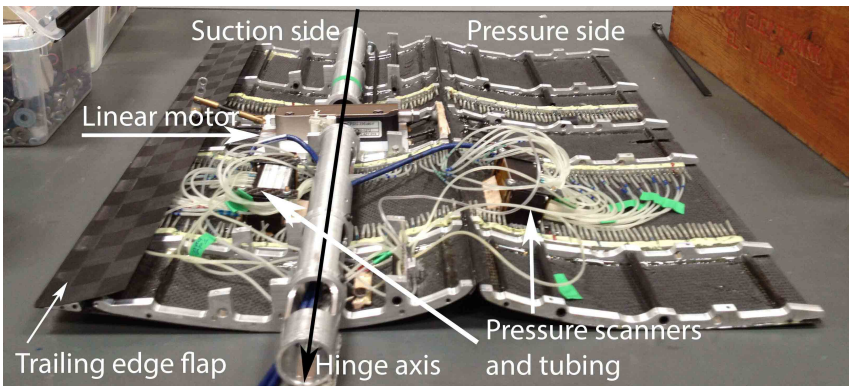

Figure 3.1: *Instrumentation inside of the wing: pressure scanners, flap linear motor, and tubing.*

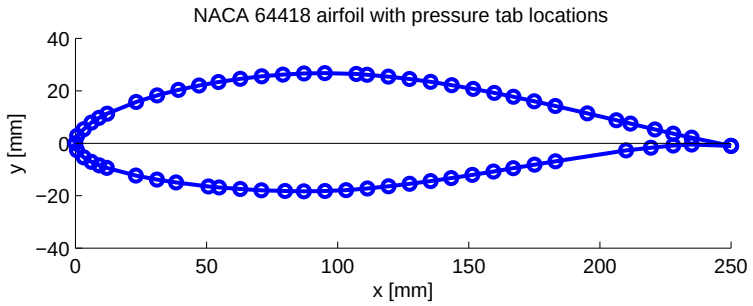

Figure 3.2: *NACA 64-418 airfoil showing the pressure tab distribution located at a span wise position of 45%.*

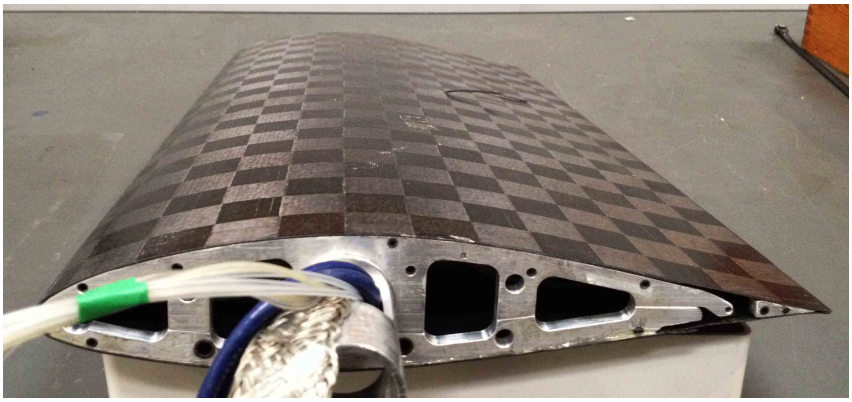

Figure 3.3: *Closed wing as used during measurements.*

3.1.2 Open-return wind tunnel

The open return wind tunnel of DTU is of the open-return type with test section dimensions: $l \times w \times h = 1.3\,\text{m} \times 0.5\,\text{m} \times 0.5\,\text{m}$. The boundary layer parameters and turbulence intensity of the wind tunnel were measured in previous experiments conducted by Bartholomay. For a more detailed description, the reader is referred to [6]. Figure 3.4 shows the layout and dimensions of the open return tunnel.

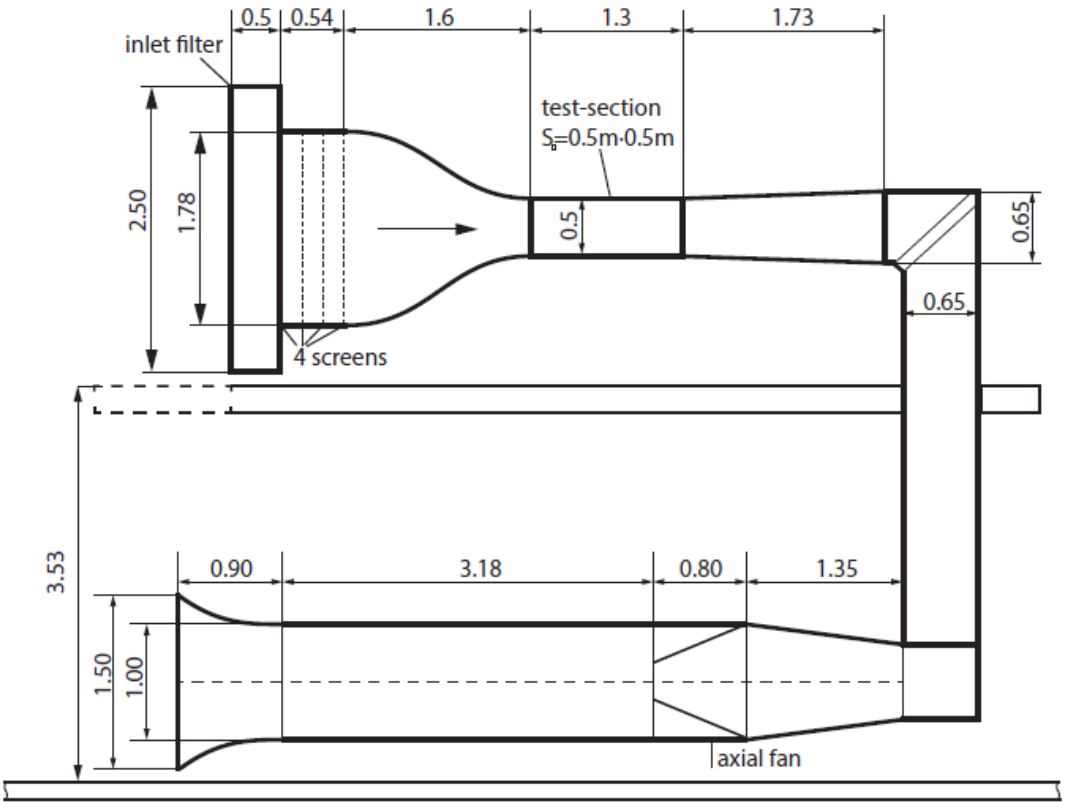

Figure 3.4: *Layout and dimensions of wind tunnel in meters [6].*

This type of tunnel has the disadvantage that the flow quality in the test section is relatively low compared to a closed return wind tunnel. In this tunnel, four screens at the inlet are used to reduce the turbulence intensity and hence improve the quality of the flow. A close-up photograph of the test section with the wing fitted inside the test section is shown in Figure 3.5. The hinge axis of the wing at the bottom, is connected to a servomotor which controls the harmonic motion through a voltage generator that relates voltage to the desired angle of attack amplitude. The wind tunnel velocity is measured using a Pitot tube placed at the beginning of the test section.

The previously measured turbulence intensity (TI Equation (3.1)) of the wind tunnel is obtained for a range of $15 < U_\infty < 55$, showing a decrease with increasing flow velocity and ranging from $0.221\% < TI < 0.164\%$ [6].

(a) Wing inside test section. (b) Wind tunnel test section.

Figure 3.5: *Experimental set-up DTU wind tunnel.*

In another publication, for a lower velocity range, TI increases with velocity as: $2.5\,\mathrm{m\,s^{-1}} < U_\infty < 20\,\mathrm{m\,s^{-1}}$ and $0.32\% < TI < 0.45\%$ [20].
Based on the ratio between the root mean square of the turbulent velocity fluctuations and the Reynolds averaged mean velocity and in (3.1) it can be calculated what value TI takes on.

$$TI = \frac{u_{rms}}{u_{mean}}, \tag{3.1}$$

where $_{rms}$ represents the root mean square.

3.1.3 Instrumentation

The instrumentation used in the experiments consists of the following devices.

- Pressure scanner.
  - The pressure scanner senses the pressure as result of fluctuations in flow velocity over the airfoil surface.
  - There are two pressure scanners with 32 ports each and a measuring accuracy of $\pm 0.03\%$ [21]. One is mounted on the pressure side of the wing and one on the suction side.
- Linear motor.
  - The linear motor is used to control the motion of the trailing edge flexible flap.
  - Technical issues prevented the use of the flap during measurements.

- Servomotor.
  - The servomotor is used for the harmonic motion of the main airfoil.
  - A prescribed motion is fed to the controller through a voltage generator resulting in a near sine motion, see Figure 3.6.
- Data acquisition system.
  - The pressure from the scanners is fed to the acquisition system.
  - This, in turn sends it to a computer where various graphs can be made visible on the monitor using LabVIEW.
- Voltage generator.
  - The voltage generator enables the user to set the frequency and amplitude of the desired motion.
  - In order to obtain the wanted motion, the generator is connected to the servomotor.
- Wind tunnel control system.
  - An on/off switch to start up or shut down the wind tunnel.
  - A control to set the tunnel velocity.
- Computer.
  - MacTalk to control the servomotor.
  - LabVIEW to obtain and process the pressure readings.
  - LinMot for the flap movement (not used).

3.1.4 Test cases

After preparing and fitting the wing in the wind tunnel, all tasks were completed to start the measurement campaign. Measurements are done for different mean angles of attack, amplitudes and reduced frequencies summarised in Table 3.2.

Before actually starting to measure all the test cases, the servomotor motion is benchmarked against a perfect sine motion. From Figure 3.6 it can be seen that the motion resembles a sine function closely, except for some minor deviations at the extremities.

It must be noted that with increasing angle of attack, the blockage effect of the tunnel increases. Since the tunnel velocity is not linked to the blockage, the tunnel velocity decreases for high angles of attack. The effect of this on the experimental data is discussed in Chapter 5. Since the test section is actually too small for the size of the wing, the walls exert an influence on the streamlines around the wing. This is compensated in Q^3UIC by modelling the wind tunnel walls as source panels with a constant distribution. The influence of the walls is reduced for smaller wings, in this case the wing could not be manufactured smaller because of the internal instrumentation.

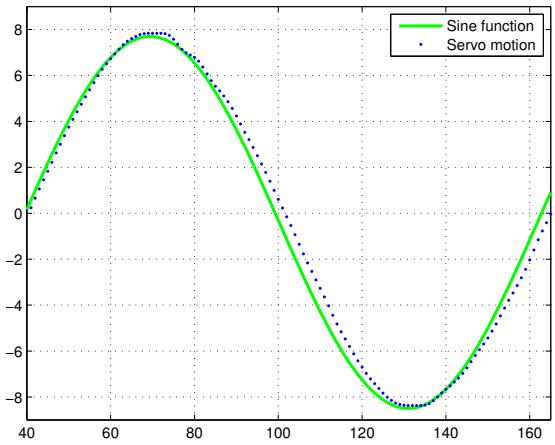

Figure 3.6: *Servomotor motion translated to $\alpha(t)$ benchmarked against a sine function.*

Prior to the measurements of the unsteady behaviour, a set of steady measurements are carried out for angles of attack: $-10° < \alpha < 25°$. Considering a free transition of the boundary layer and a boundary layer that is tripped to a turbulent state. The boundary layer is tripped using small metal strips close to the leading edge of the wing, as shown in Figure 3.7.

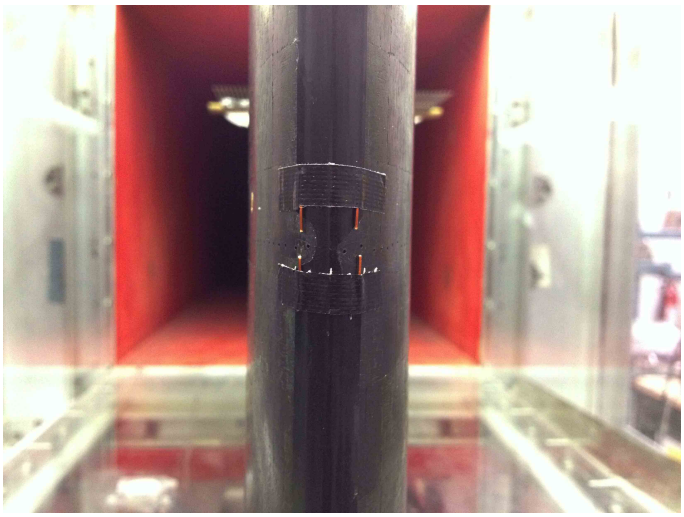

Figure 3.7: *Trip wires used to force an early boundary layer transition at $x/c \approx 5\%$.*

All the test cases that are analysed are summarised in Tables 3.1 and 3.2. The mean angles of attack and the amplitudes are chosen in such a way to cover the main part of the lift polar; in the unsteady loops ranging from $-8° < \alpha < 20°$. The reason for choosing the frequencies is because of the maximum attainable frequency of the servo motor of 2 Hz or $k = 0.0628$, which is just in the unsteady regime. For an easy and scalable comparison the other frequency is chosen to be half of the maximum value.

The results of the measurements are discussed in detail in Chapter 5.

Table 3.1: *Steady test cases NACA 64-418.*

Transition state	**Angle of attack range**
Free transition	$-10° < \alpha < 25°$
Tripped transition	$-10° < \alpha < 25°$

Table 3.2: *Unsteady test cases, NACA 64-418 pitch measurements.*

Frequency k and f	**Boundary layer transition**			
	Free transition		**Tripped transition**	
	Mean $\alpha_{\mathbf{m}}$[°]	$\Delta\alpha$[°]	**Mean $\alpha_{\mathbf{m}}$[°]**	$\Delta\alpha$[°]
k = 0.0314 **f = 1 Hz**	0	4	0	4
		8		8
	4	4	4	4
		8		8
	8	4	8	4
		8		8
	12	4	12	4
		8		8
k = 0.0628 **f = 2 Hz**	0	4	0	4
		8		8
	4	4	4	4
		8		8
	8	4	8	4
		8		8
	12	4	12	4
		8		8

Figure 3.8: *Trailing edge flap and servo motor on the DU 95-W-180 experimental model.*

3.2 TU Delft measurements on a morphing flap

This section gives an overview of the experimental study conducted in the LTT of TU Delft (Low speed, low Turbulence wind Tunnel) using a DU 95-W-180 airfoil with a morphing trailing edge flap region hinged at $x/c = 0.8$.

3.2.1 DU 95-W-180

For the experimental study a DU 95-W-180 airfoil is used with a morphing trailing edge flap. The wing is designed for $Re = 3 \cdot 10^6$ and is fabricated in fibre-glass composite with a polished polyester gel coat surface with a surface deviation that lies below 0.1 mm [22]. The term morphing should be clarified, because the skin is not actually morphing. The difference with a conventional flap is that there is no gap between the main airfoil and the trailing edge flap; as illustrated in Figure 3.8, the gap is sealed of as if the two parts were actually one.
The wing has a Delft University (DU) airfoil, from the year 1995 (95), used for wind energy applications (W) with a thickness to chord ratio t/c of 18% (180). The model has a chord of 0.6 m and a span of 1.25 m, designed to fit in the wind tunnel test section in vertical direction. The trailing edge is thin in order to avoid excessive boundary layer noise and the trip wire for forced transition measurements is located at approximately $0.05x/c$.
Pressures are measured through orifices distributed over the wing surface and by a wake rake system in the wake of the wing, see Figure 3.10a. The method of data acquisition is further discussed in Section 3.2.3.

3.2.2 Low-Speed Low-Turbulence Wind Tunnel (LTT)

The LTT is of an atmospheric closed single-return type with a total length of 72.7 m and a contraction ratio of 17.8:1. The test sections are removable and are octagonally shaped.

A 25 k W DC motor drives a fan with six blades giving a maximum velocity of $120\,\mathrm{m\,s^{-1}}$ and a maximum Reynolds number of $Re = 3.5 \times 10^6$. Exact dimensions of the test section and characteristics of the tunnel are summarised in Table 3.3 and a complete overview of the tunnel is illustrated in Figure 3.9.

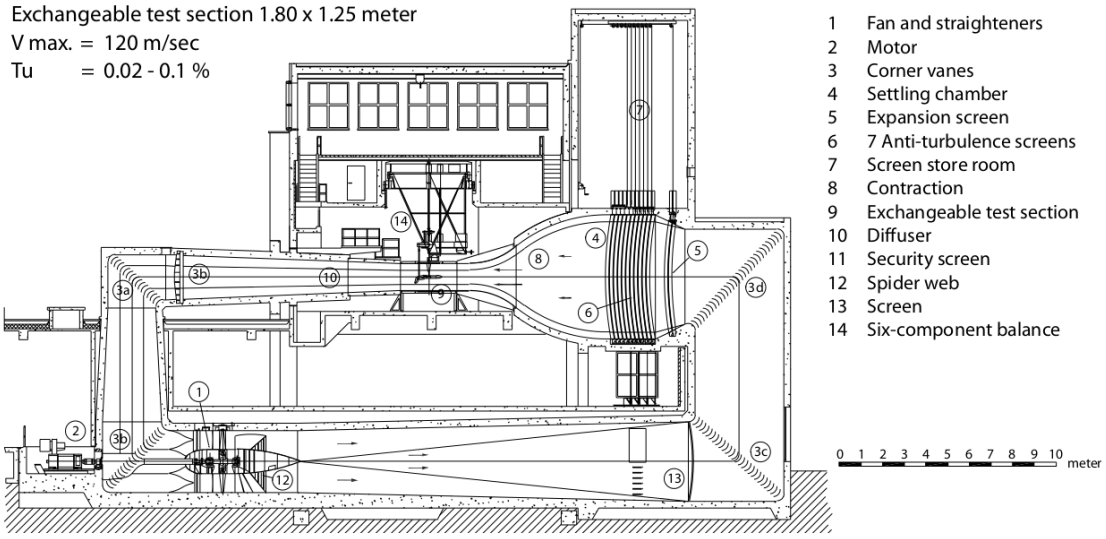

Figure 3.9: *LTT characteristics and components [7].*

Table 3.3: *LTT characteristics and dimensions.*

Maximum velocity	$120\,\mathrm{m\,s^{-1}}$
Turbulence Intensity	0.02 – 0.1%
Test section $l \times w \times h$	$2.60 \times 1.80 \times 1.25\,\mathrm{m}$
Contraction ratio	17.8 : 1

3.2.3 Instrumentation

The flap actuation is done using two servo motors JR DS8711HV, supplied by a voltage of 7.4 V and controlled by a varying pulse width signal of 50 Hz. One servo mounted on top and the other at the bottom of the flap. In order to get the real flap deflection, the voltage drop over the internal potentiometer is measured, after having calibrated the relation between flap deflection and voltage.

For the pressure measurements, the DTC Initium system is used with six ESP pressure scanners and LabVIEW. Four scanners are designated to the pressure tabs on the airfoil surface and two for the wake rake. A rectangular trigger signal of 300 Hz was used to trigger measurements of the six scanners. Sampling of the scanners is done simultaneously while the sampling per channel of a scanner in series.

The voltage of the servo and the trigger signal were logged with a sample rate of 10 kHz. Correlating the servo position, i.e. the flap deflection and the pressure is done by checking at which point the pressure sampling starts in relation to the trigger pulse.

(a) Wing and wake rake inside test section.

(b) Wind tunnel test section and inlet.

Figure 3.10: *Experimental set-up LTT.*

3.2.4 Test cases

The measurements were performed at a wind speed of $25\,\mathrm{m\,s^{-1}}$, which translates to

$$Re = \frac{\rho U_\infty c}{\mu} = \frac{1.2 \cdot 25 \cdot 0.6}{1.81 \cdot 10^{-5}} = 10^6 \tag{3.2}$$

During the measurements Re is steadily kept at one million by adjusting the wind tunnel velocity as it decreased slightly with increasing angles of attack. The steady polars are measured for angles of attack: $-15° < \alpha < 18°$. Above 18°, readings are not considered to be of much interest due to the large blockage effect.

Table 3.4 summarises all the unsteady test cases that are measured. The considered frequencies range from:

- $k = 0.01$: Nearly steady
- $k = 0.05$: Intermediate stage, quasi–steady
- $k = 0.1$: Unsteady

The selected angels of attack are chosen based on:

- $\alpha = 0°$: Should show little, if any deviations in unsteady behaviour; test case.
- $\alpha = 8°$: $\left(\frac{L}{D}\right)_{max}$
- $\alpha = 18°$: $C_{l,max}$

Table 3.4: *Unsteady test cases, DU 95-W-180 flap measuerements.*

Frequency k and f	**Boundary layer**			
	Free transition		**Forced transition**	
	$\alpha[^\circ]$	$\Delta\beta[^\circ]$	$\alpha[^\circ]$	$\Delta\beta[^\circ]$
k = 0.01 **f** = 0.1326 Hz	0	5	0	5
		10		10
	8	5	8	5
		10		8
	18	5	18	5
		10		10
k = 0.05 **f** = 0.6631 Hz	0	5	0	5
		10		10
	8	5	8	5
		10		10
	18	5	18	5
		10		10
k = 0.1 **f** = 1.3263 Hz	0	5	0	5
		10		10
	8	5	8	5
		10		10
	18	5	18	5
		10		10

Finally, the choice is made to measure for the maximum attainable flap deflection of the experimental model $\Delta\beta = 10°$ and half the maximum flap angle $\Delta\beta = 5°$.

The results for both steady and unsteady as well as for a free and forced boundary layer transition are discussed in detail in Chapter 5.

Chapter 4

Numerical methods

In this chapter an overview is given on Q^{3}UIC and the open source CFD tool OpenFOAM. The structure and theory behind the tools is described in order to get a clear understanding of the differences and similarities of both models.

4.1 Q^{3}UIC – Lagrangian approach

This section describes the basic theories and structure behind the viscous-inviscid interactive code that is used to analyse harmonically pitching airfoils in unsteady flow. The essence of this approach is based on a Lagrangian description of the flow field, where individual fluid particles are followed through space and time.

4.1.1 Theory

Q^{3}UIC is a computational tool capable of, amongst other, modelling the aerodynamic behaviour of an airfoil in unsteady flow. It does so through a strong interaction between the viscous boundary layer close to the airfoil surface and the inviscid outer flow far away from the surface. A strong coupling method has the advantage of a solid numerical stability and a good capability to solve the boundary layer equations after separation takes place. The viscous and inviscid flows are coupled by the transpiration velocity w_T (4.1). The normal velocity at the surface is forced to have a non-zero value as opposed to the conventional Neumann type boundary condition which assumes zero normal velocity at the surface, also referred to as the 'no-penetration condition'.

$$w_T = \frac{1}{\rho_i} \frac{\partial}{\partial s} \left(\rho_i u_i \delta_i^* \right) \tag{4.1}$$

If a fast solution and low computational costs are desired, a viscous-inviscid interaction method can be used as an alternative to CFD methods, where the full Navier-Stokes equations are solved. By continuously solving the NS equations, CFD methods can become

computationally very expensive. In contrast to this, a viscous-inviscid solver is faster because there is no need to make extensive time consuming meshes of the surroundings and it is not required to solve the full NS equations.

The inviscid part is modelled using a 2D potential panel method, whereas the viscous part is calculated with the integral form of the boundary layer equations discussed in Section 2.4. Because the outer inviscid flow is treated as a potential flow, the calculations are straightforward, facilitating the computations on that part.
More effort and time is needed to solve the viscous part, since the integral form of the boundary layer equations are derived from the full Navier-Stokes equations. The computational advantage comes from the parabolic nature of the partial differential equations; as the full Navier-Stokes equations are of an elliptical form and are therefore increasingly complicated and time demanding to solve.

4.1.2 Structure and solving procedure

As previously mentioned, Q^{3}UIC models aerodynamic properties through the interaction between viscous and inviscid flow. A 2D panel method is used for a proper modelling of the inviscid flow. In this code, 140 panels are used to discretise the airfoil surface, following a cosine distribution. This results in smaller panels in the vicinity of the leading and trailing edges, and larger panels in between. As such, it is possible to capture important flow fluctuations and pressure peaks, which take place near the edges, more accurately. Using a cosine distribution, a total of 140 panels means that both upper and lower surface consist of 70 panels. The number of chord-wise panels divides the semicircle as $\Delta\beta = \pi/70$. The chord-wise position of a point can be obtained using:

$$x = \frac{c}{2} \cdot (1 - \cos\beta) \tag{4.2}$$

In the center of each panel there is a control point, starting from the trailing edge of the lower surface (1) and moving clockwise towards the trailing edge of the upper surface (N), see Figure 4.1.

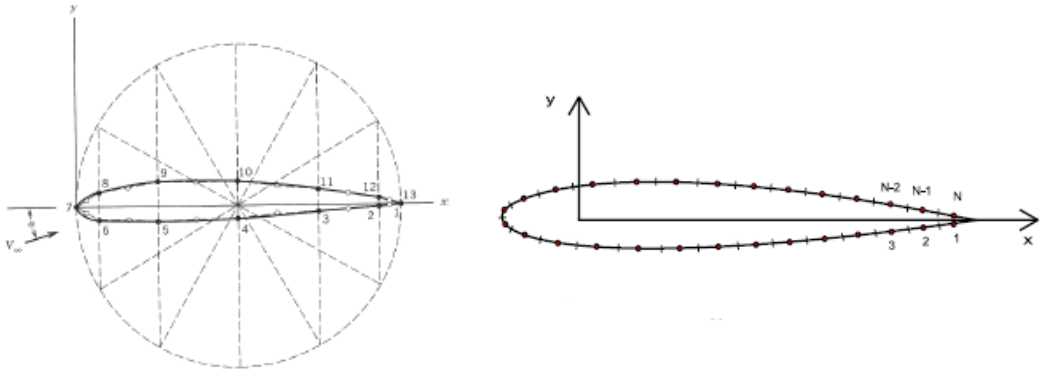

(a) Airfoil discretisation from [23].

(b) Airfoil discretisation from [4].

Figure 4.1: *Airfoil surface discretisation in panels using cosine distribution.*

In order to resolve the boundary layer, Q^{3}UIC uses the integral boundary layer equations, where the laminar attached BL equations are covered by Thwaites method which solves the Kármán momentum integral equation in terms of a parameter λ. This parameter is discussed and derived in [4] together with the whole process of how the equations are solved and discretised.

Q^{3}UIC makes use of the single wake model to simulate the flow around an airfoil. The final solution of the velocity distribution around the airfoil for one time step is obtained through a superposition of separate solutions as shown in (4.3).

$$U = U_\infty + \sigma U_{trans} + \Gamma U_{rot} + w_T + u_w + u_{walls} \tag{4.3}$$

The first term is the free stream flow and σ creates a constant panel sources distribution around the airfoil influencing the translating flow U_{trans}. U_{rot} (rotating) is dependent on the circulation Γ around the airfoil and the parabolic vorticity distribution. The transpiration velocity w_T represents the influence of the viscous flow on the inviscid part. The last two terms are the influence of the inviscid wake and wind tunnel walls. The latter is modelled using a constant strength distribution of source panels.

The viscous integral boundary layer equations are solved using the stream-wise momentum. The code is also capable of simulating quasi 3D effects in the radial direction, but these are not considered in this discussion. In order for the code to converge and to solve the entire set of equations several closure conditions and relations are implemented, including the unsteady version of the Kutta condition discussed in Section 2.5. Closure relations contain the displacement- δ^*, momentum- θ and boundary layer δ thicknesses, the shape factor H and skin friction coefficient C_f. All these parameters are discussed in Chapter 2. An additional model to calculate the transition point is also present and is based on the e^9 model.

The formulation and implementation of a proper unsteady Kutta condition as touched upon in Section 2.5 and studied by [17] [18], is of great importance for a proper solution and modelling of the flow at the trailing edge. Q^{3}UIC has three formulations implemented, of which the first is based on the bound vorticity [24], and the third on the wake vorticity.

$$\text{Basu \& Hancock v1} = U_1^2 - U_n^2 + 2 \cdot d\Gamma_b/dt \tag{4.4}$$

$$\text{Basu \& Hancock v2} = U_1^2 - U_n^2 - 2 \cdot d\Gamma_b/dt \tag{4.5}$$

$$\text{Katz, Fage \& Johansen} = U_1^2 - U_n^2 - 2 \cdot d\Gamma_w(N_{pan} + 1)/dt, \tag{4.6}$$

where subscript $(_b)$ represents the bound vorticity around the airfoil $(_w)$ the wake vorticity, $(_1)$ the first lower TE panel and $(_n)$ the last upper one as illustrated in Figure 4.1. A suitable Kutta condition basically accounts for viscosity effects in an essentially inviscid numerical model. In unsteady flow conditions, the notion of a zero pressure difference does not hold. A discussion on the effects of a finite pressure difference at the trailing edge on lift is given in [17].

To come to a solution, all equations of the in panels discretised airfoil are placed in one Jacobian matrix, and are calculated in one Newton iteration. Each panel has its own sub matrix which in turn consists of panel method equations, boundary layer equations, the relevant closure models and a model for calculating transition. Additionally the influence

of panels on each other, together with the transpiration velocity and the Kutta condition are also placed in this sparse matrix which is solved iteratively. For every time step, the whole set of equations is solved and updated every Newton iteration using:

$$x_n = x_{n-1} + \omega \Delta x \tag{4.7}$$

where x is a system variable and ω its relaxation factor. If the maximum number of iterations is exceeded, the solution at that particular time step does not converge and the solver moves on to the next time step.

4.1.3 Flap deflection

The deflection of the flap as it is done in Q^{3}UIC is illustrated in Figure 4.2 [6]. The trailing edge (TE) point is translated in x- and y-direction by:

$$dx_{TE} = u_{TE}dt = v_r \cdot \sin(\theta)dt = \Omega r \cdot \sin(\theta)dt \tag{4.8}$$

$$dy_{TE} = v_{TE}dt = -v_r \cdot \cos(\theta)dt = \Omega r \cdot \cos(\theta)dt, \tag{4.9}$$

where Ω is the angular frequency, v_r the trailing edge point velocity and θ the angle between the hinge- and trailing edge point. The deflection between these points is distributed linearly as:

$$x_{i,j} = x_{i-1,j} + dx_{TE} \cdot \left(\frac{x_{i-1,j} - x_{i-1,FP}}{x_{i-1,TE} - x_{i-1,FP}} \right) \tag{4.10}$$

$$y_{i,j} = y_{i-1,j} + dy_{TE} \cdot \left(\frac{x_{i-1,j} - x_{i-1,FP}}{x_{i-1,TE} - x_{i-1,FP}} \right), \tag{4.11}$$

where $_{FP}$ are the fixed points and relate panel numbers $_j$ to the hinge point of the flap, $_i$ the current time step. As shown in Figure 4.2, the pressure side deflects linearly and the suction side follows a polynomial. In steady conditions Q^{3}UIC uses a spline to rebuild this shape but for unsteady motions, a spline results in a length change of the panels, which would result in incorrect panel velocities. Therefore, the flap is deflected linearly in unsteady conditions. The difference between the two deflections is relatively small as shown in Figure 4.2. Deviations occur only on the suction side in the near vicinity of the hinge.

4.1.4 Inputs

In this study, primarily the subroutine `INPUTS.f90`, is used to match the Q^{3}UIC inputs to the experimental data. The main variables are reduced frequency k, mean angle of attack α_m and harmonic amplitude around the mean angle of attack α_A. The nature of the transition can be adjusted by specifying the panels on which there is a free boundary layer development. In case of a forced transition this is $\pm 5\%$ from the leading edge and for a free developing boundary layer this is increased to around 60% of the chord to make sure that the development of the boundary layer is not obstructed. In order to compare experimental wind tunnel data, Q^{3}UIC has the option to model the wind tunnel walls using panels with a source distribution. This is important considering the blockage effect for relatively high angles of attack.

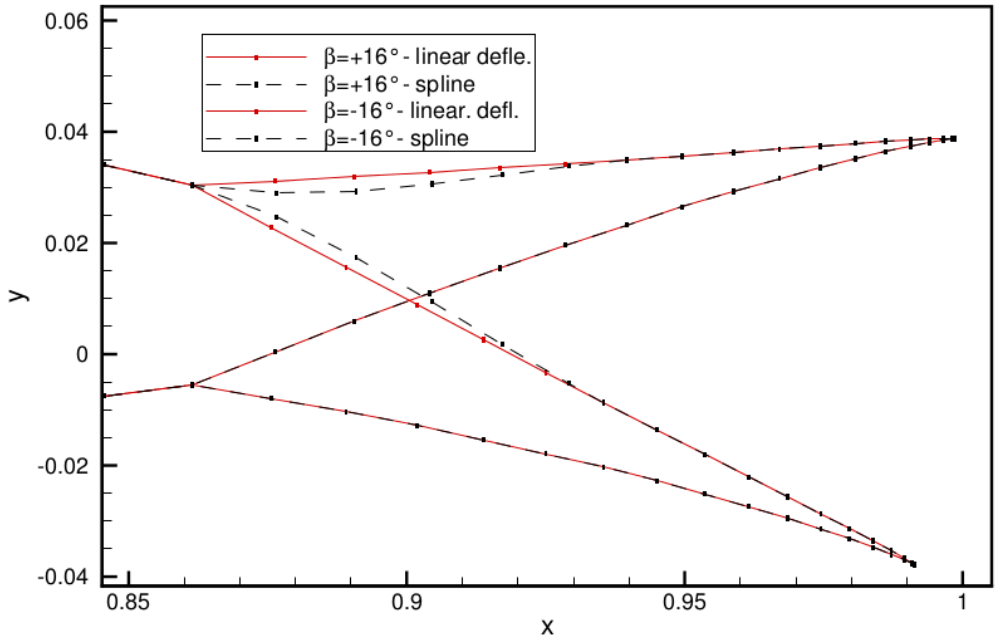

Figure 4.2: *Linear and polynomial flap deflections [6]. Q^{3}UIC uses linear deflection for unsteady flap motion.*

4.2 OpenFOAM – Eulerian approach

In contrast to the Lagrangian approach which follows fluid particles in space and time, the Eulerian description of the flow measures the fluid particle characteristics as it passes through a cell with a fixed location in space. However, when meshes are not fixed but cells deform or move with the motion of the airfoil, the Lagrangian and Eulerian methods are combined into the Arbitrary Lagrangian-Eulerian (ALE) method. The CFD software used for this is OpenFOAM (Open Field Operation and Manipulation), written in `C++` and utilising the finite volume method for solving partial differential equations on any grid. After a grid is made and boundary conditions are set, the equations are solved and finally the fields can be viewed and analysed.

Based on previous studies [14] [25], the CFD simulations in Chapters 5 and 6, are performed with the k-ω SST turbulence model, which has proven to be the most appropriate for problems as those discussed in this thesis.

4.2.1 Theory and turbulence models

The finite volume approximation of the dimensional NS-equations from Equation (2.37) that is used in OpenFOAM is described next, together with a short mentioning of discretisation schemes and the linear eddy viscosity turbulence models k-ω and k-ε.

Discretisation schemes

OpenFOAM operates using implicit and semi–implicit time stepping. Implicit in this case means that the discretised time derivative is evaluated at at a future time:

$$\frac{\varphi^{n+1} - \varphi^n}{\Delta t} = F\left(\varphi^{n+1}\right) \quad \Rightarrow \tag{4.12}$$

$$\Rightarrow \quad \varphi^{n+1} = \varphi^n + \Delta t \cdot F\left(\varphi^{n+1}\right), \tag{4.13}$$

where the derivative $\frac{\partial \varphi}{\partial t}(x,t) = F(\varphi)$ is discretised like $\frac{\varphi^{n+1} - \varphi^n}{\Delta t} = F(\varphi)$. Because of the implicit nature of the time stepping in OpenFOAM, the CFL condition of $Co \leq 1$ does not have to be satisfied.

OpenFOAM provides users with the choice of various numerical schemes – e.g. interpolation, time, gradient, divergence – to choose from in the `system/fvSchemes` directory. Interpolation between cells can be done using centred or upwind schemes, where upwind schemes are further subdivided. The time schemes' numerical behaviour of the derivative $\partial/\partial t$ can be specified first or second order. The choice of schemes and their behaviour can have a big influence on the results regarding stability, errors and convergence and should be chosen with care. For instance, a first order accurate upwinding scheme, increases the error but it will also tend to stabilize the resulting set of equations.

The solvers for the schemes can be specified in `fvSolution`, where there is a choice between linear solvers; divided in PBiCG (Preconditioned (Bi–) Conjugate Gradient) and GAMG (Generalised Geometric–Algebraic Multig–Grid). Dependent on the variable

of interest a choice is to be made which solver is the proper one to use. Differences are found in how the solution is initialised, mapped and treated during the calculation process.

Navier-Stokes finite volume approximation

Integrating the momentum equation over a control volume V_C gives rise to (4.14) with the classification of the terms depicted underneath.

$$\underbrace{\int_{V_C} \frac{\partial \mathbf{u}}{\partial t} dV}_{\text{Temporal}} + \underbrace{\int_{V_C} \nabla \cdot (\mathbf{uu}) dV}_{\text{Convective}} - \underbrace{\int_{V_C} \nabla \cdot (\nu \nabla \mathbf{u}) dV}_{\text{Diffusive}} = \underbrace{\int_{V_C} \frac{\nabla p}{\rho} dV}_{\text{Pressure}} \tag{4.14}$$

Each of the terms shown in (4.14) is solved using the PISO (Pressure Implicit with Splitting of Operators) method in OpenFOAM. Reformulating Equation (4.14) using Gauss' theorem and grouping the results of the discrete finite volume terms of the momentum equation together with the discretised continuity equation, results in the pressure equation of the PISO method. A more extensive explanation can be found in [26]. The PISO algorithm uses the pressure of the current time to determine the velocity at the new time and after the pressure based on the new velocities is calculated, the velocity can be updated. Finally, using the updated velocity, the cell face flux is calculated. The transient solver PIMPLE is a combination of the PISO algorithm and the steady state solver SIMPLE (Semi–Implicit Method for Pressure–Linked Equations). Due to this semi–implicit nature, some values are dependent on previous time steps and extra iterations are required to correct the initial solution.

Moving meshes

In case of moving meshes, Equation (4.14) requires an additional term that specifies the velocity of the mesh movement $\mathbf{u_m}$. The new equations are referred to as the Arbitrary Lagrangian-Eulerian (ALE) Navier-Stokes equations and the ALE momentum equation is found in (4.15), where the convective and temporal term have changed compared to (4.14).

$$\frac{\partial}{\partial t} \int_{V_C} \mathbf{u} dV + \oint_{V_C} \mathbf{n} \cdot (\mathbf{u} - \mathbf{u_m}) \mathbf{u} dS - \int_{V_C} \nabla \cdot (\nu \nabla \mathbf{u}) dV = \int_{V_C} \frac{\nabla p}{\rho} dV \tag{4.15}$$

This modification adds a new requirement called the Discrete Geometric Conservation Law (DGCL) stating that the change in volume of a cell must equal the volume swept by the faces of the cell.

Turbulence models

This section is dedicated to set out the main difference between the k-ε and k-ω turbulence models. k-ε is the more widely used model for relatively simple flow problems that need no accurate modelling of the boundary layer and complex viscous effects. It

performs poorly for separated flow conditions with adverse pressure gradients [27].
The k-ω model however, does allow for a more accurate near wall boundary layer treatment and performs better under adverse pressure gradients in separated flow conditions. A downside is that k-ω requires more computational power in comparison to the k-ε model. A combination of both the k-ω and the k-ε model, namely k-ω SST (Shear Stress Transport) is used in this study. Near the wall k-ω is used and further away a blending function ensures the transition to k-ε. Due to the inclusion of the transport of turbulent shear stress, the near wall treatment is enhanced allowing the onset and amount of flow separation under adverse pressure gradients to be modelled more accurately. Additionally there are turbulence models that sustain the turbulent inflow parameters more strongly and also models which are more suited for lower Reynolds number problems. These are not further addressed but can be found in [28] and [29].

4.2.2 Model specific inputs

In order to conduct a successful research it is imperative to know how to translate theory into practice. The coordinate axes are fixed to the airfoil which moves about its quarter chord point as result of a specified amplitude and frequency. The mean angle of attack however, is not controlled by the pitch motion of the airfoil but by a change of inflow angle of the air flow. For the comparison with experiments and Q^{3}UIC, the x and y components of the force coefficients are recalculated to actual lift and drag values using the relations in (4.16). The forces are calculated by integrating the pressure and shear stress over the airfoil surface.

$$\begin{aligned} C_l &= C_y \cos(\alpha) - C_x \sin(\alpha) \\ C_d &= C_y \sin(\alpha) + C_x \cos(\alpha) \end{aligned} \tag{4.16}$$

4.2.3 Mesh topology and deformation due to flap deflection

The computational domain in both the NACA and the DU airfoil case was made using the same approach. First an initial cell size is determined based on the $y^+ = 1$ condition. With a suitable growth rate, the adjoining cells are extruded for the boundary layer region. Special care is taken of the trailing edge region to avoid cells with high aspect ratios or large skewness. The rest of the O-mesh is extruded into the far field radius of approximately 90 chord lengths. The exact numbers and characteristics corresponding to the two test cases are provided in the results chapters 5 and 6.

The mesh deformation due to deflection of the flap for the Du 95-W-180 case is illustrated in Figure 4.3. The flap is hinged at $x/c = 0.8$ and mainly deforms the cells in the vicinity of the hinge. Where one column of cells is elongated in the direction parallel to the surface while the two adjacent columns are slightly compressed. This effect weakens as the distance from the hinge increases.

4.2.4 Mesh independence

To ensure that the results are independent of a change in mesh density, it is needed to perform a mesh independence study. In general, as the number of cells grows, i.e. if

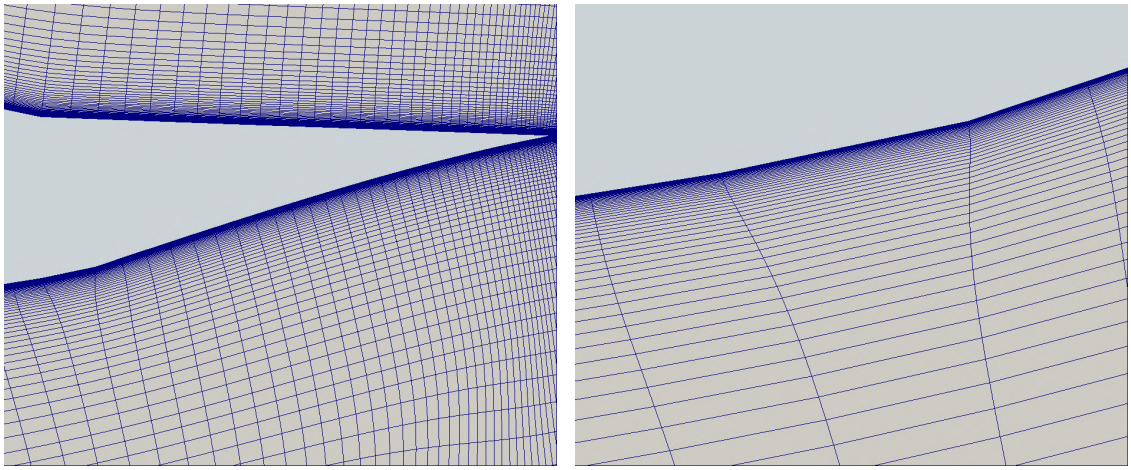

(a) Maximum negative flap deflection $\beta = -10°$.

(b) Detailed view of cell deformation near hinge at $\beta = 10°$.

Figure 4.3: *Mesh deformation at maximum flap deflection.*

the mesh becomes finer, the solution should increase in accuracy. Once the solution does not change to within a predefined value, the solution can be considered converged with respect to the mesh. This can be done by means of the Richardson extrapolation.

Richardson extrapolation

The general idea of the Richardson extrapolation is to generate high accuracy results by using simple formulae. Based on the step size h, it is possible to predict outcomes without actually knowing them. After having taken an initial step size, the next iteration is done with half the initial step size. With each iteration the accuracy is improved and the error decreases.
In this study this extrapolation method is used for the mesh study, of which a more detailed description is given in [30]. Eventually the method uses the equations listed in Table 4.1 to obtain a mesh with an infinite number of cells and its corresponding value.
A numerical example is used to illustrate this procedure. Figure 5.7a shows the steady state vertical force coefficient values for the three meshes, and by applying the steps from Table 4.1, the final value is extrapolated from the three already known values. As the mesh density increases the value should converge towards the final extrapolated value. Now to make a choice on which mesh is most suitable a trade-off has to made between accuracy of the outcome and computational time. It is common to allow a maximum deviation of 1% from the extrapolated 'infinite' value. From Table 4.2 it follows that the middle and the finest mesh both comply to this criterion.
However, as this example is based on a steady state solution, the middle mesh may be too coarse with respect to unsteady simulations. So regardless of the 1% criterion it may still be unsuitable for further use. The basic idea of a mesh study can be done in this way, but when considering unsteady simulations additional mesh studies can yield more accurate results. In principle, a case in the separated region with an angle of attack around 12 degrees requires a considerably finer mesh (and time step) than a simple, low angle of

attack case. That is why in some cases, this method needs additional criteria to define a mesh that is sufficiently dense.

Table 4.1: *Richardson extrapolation to find C_y value for a mesh with an infinite number of cells.*

Simulated C_y	$N_1\,(h/2) + \dfrac{N_1\,(h/2) - N_1(h)}{3}$	$N_2\,(h/2) + \dfrac{N_2\,(h/2) - N_2(h)}{15}$
$N_1(h) = 0.8695$		
$N_1(h/2) = 0.8119$	$N_2(h) = 0.7927$	
$N_1(h/4) = 0.8058$	$N_2(h/2) = 0.8037$	$C_{y,\infty} = 0.8045$

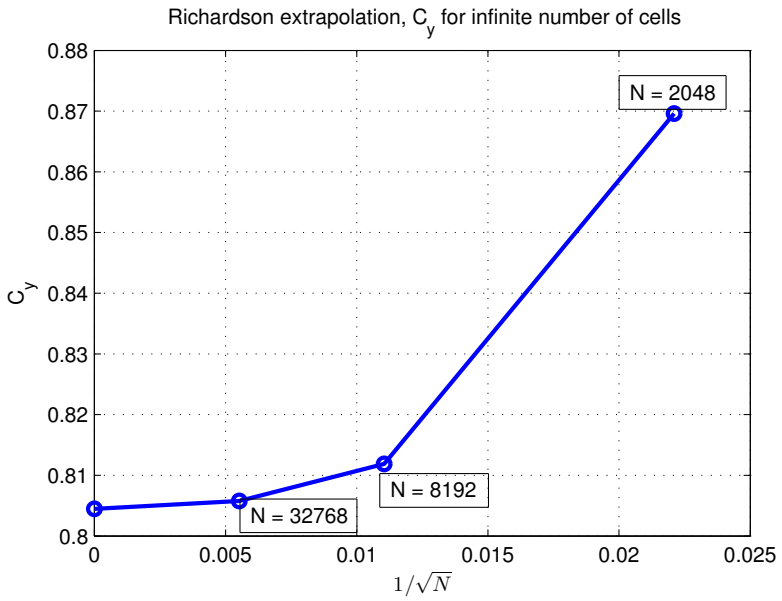

Figure 4.4: *Determination of suitable mesh using Richardson extrapolation.*

Table 4.2: *Mesh size and percentage difference between the different meshes and final extrapolated C_y value.*

N	C_y	**% difference**	**Cost [s]**
2048	0.8695	8.1%	90
8192	0.8119	0.9%	373
32768	0.8058	0.16%	1163

4.2.5 Turbulent inflow parameters

In order to get the turbulence properties of the surrounding flow, the proper parameters need to be defined and set as initial conditions. In this study, the k-ω SST turbulence model is used where SST stands for turbulent shear stress transport. Following the description given in [29], Equation (4.17) shows how the wall and far field values for k and ω are approximated.

$$\frac{U_\infty}{c} < \omega_{farfield} < 10\frac{U_\infty}{c} \tag{4.17}$$

$$10^{-5}\frac{U_\infty^2}{Re_L} < k_{farfield} < 0.1\frac{U_\infty^2}{Re_L} \tag{4.18}$$

$$\omega_{wall} = 10\frac{6\nu}{\beta_1(\Delta d_1)^2} \tag{4.19}$$

$$k_{wall} = 0 \tag{4.20}$$

where the constant ν is obtained from `constant/transportProperties` as $\nu = \frac{U_\infty L}{Re}$, $\beta_1 = 0.075$ and d_1 is the initial cell size based on the calculation of $y^+ = \frac{u_* y}{\nu} = 1$ using flat plate boundary layer theory as described by White [3], where U_f is the friction velocity at the nearest wall, y is the distance to the nearest wall and ν the kinematic viscosity. Following White, using the skin friction coefficient, Re and the chord it is possible to approximate the initial cell size with Equation (4.21).

$$d_1 = \frac{y^+ \cdot \mu}{U_f \cdot \rho}, \tag{4.21}$$

$$\text{with :} \qquad U_f = \frac{\tau_{wall}}{\rho}; \qquad \tau_{wall} = \frac{C_f \rho U_\infty^2}{2}; \qquad C_f = \frac{0.026}{Re^{1/7}}, \tag{4.22}$$

where U_f is the friction velocity, τ_{wall} the wall shear stress and C_f the skin friction coefficient.

4.2.6 Time step

Once the steady state is considered it is time to take a look at the unsteady part, where the time step in which things are being solved is of importance. The idea is to examine convergence, i.e. if the time step (or Courant number) is decreased, the periodic solutions of e.g. $C_l(\alpha)$ should show less deviations from each other. This can be obtained easily by performing a check on the outcomes of the different time steps. By plotting the periods of for instance $C_l(\alpha)$ on top of each other for the simulated time steps, the deviations can be observed and analysed quantitatively. The choice for the proper time step should be based on the difference between the solutions being relatively small while at the same time sufficiently efficient with regards to computational time. A trade-off has to be made between high accuracy (smaller time step) and low computational time (larger time step). In other words, the time step should be chosen as large as possible, while maintaining sufficiently accurate solutions. This can be done either by qualitatively examining the features or by looking at percentage difference in CPU time and final solutions.

The choice of a proper time step Δt in CFD is related to the Courant–Friedrichs–Lewy (CFL) condition. Which in an explicit sense means that a moving particle is not allowed to travel a larger distance than the size of the mesh element that momentarily contains it.

Mathematically this is expressed in (4.23) by the dimensionless Courant number which is not allowed to exceed the value of 1.

$$Co = \frac{u\Delta t}{\Delta x} \leq 1, \tag{4.23}$$

where Δt is the time step, Δx the length interval (mesh element dimension) and u the magnitude of the travelling particle's velocity.
However, for implicit time stepping used in OpenFOAM there is no need to satisfy this condition because the discretised time derivative is evaluated at a future time as described in Section 4.2.1. This is in contrast to explicit time stepping where the current time is used to evaluate the time derivative.

Chapter 5

Results – Pitching airfoil

This chapter first shows the experimental results of wind tunnel measurements conducted at DTU. A harmonically pitching NACA 64-418 airfoil in an open return wind tunnel is analysed for various pitching frequencies and amplitudes. Afterwards these results are compared to Q^3UIC and OpenFOAM simulations. Some conclusive remarks and main findings are addressed at the end of the chapter.

5.1 Experimental results of the NACA 64-418 airfoil

In this section the measurements are shown which were carried out as described in Chapter 3. It must be noted that due to the blockage effect, the wind tunnel velocity, hence the Reynolds number, and also the reduced frequency, decrease with increasing angle of attack. This has an effect on the experimental data in a sense that most aerodynamic characteristics such as lift curve are lower than they should be. To account for this effect in the Q^3UIC simulations, a constant strength source distribution is placed on the wind tunnel walls using 60 panels. It is imperative to keep this in mind while comparing measurements to simulations for high angels of attack. Unfortunately no wall corrections were applied in OpenFOAM.

5.1.1 Steady measurements

Figure 5.1a shows the steady lift polars for free and tripped boundary layer transitions. The two curves are almost identical up until the stall angle of attack of the tripped measurements which is close to 8 degrees. From here on, the lift curve stalls and evens out. The maximum lift coefficient and maximum angle of attack are higher for the free measurements, implying that a laminar boundary layer shows higher lift values. Theory states that a laminar boundary layer in general has lower drag values, which is not confirmed by the measurements in Figure 5.1b. It may be said that the acquisition method is not accurate judging by the drag values in the attached flow region up to 8 degrees. The

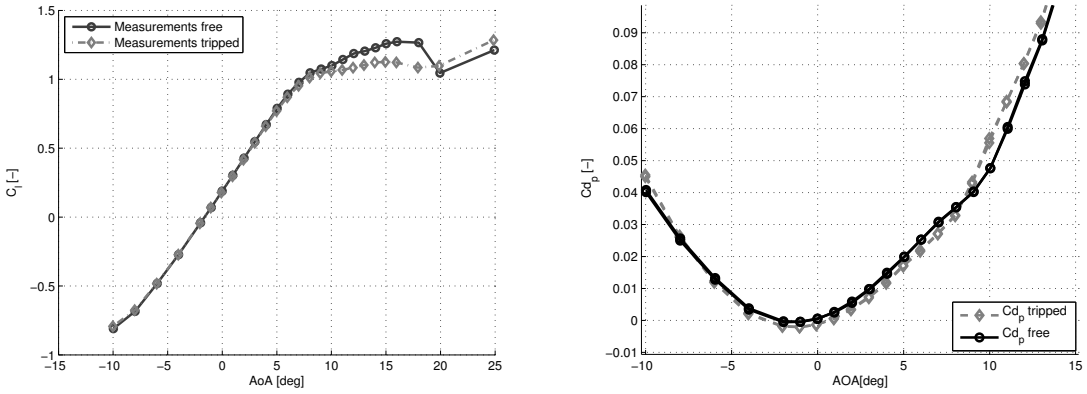

(a) Tripped and free lift polars.

(b) Tripped and free drag polars.

Figure 5.1: *NACA 64-418, measured steady lift polars for free and tripped transition.*

tripped, hence turbulent, drag values remain lower up until the stall angle for tripped transition. Lower drag values are supposed to be mainly related to a lower skin friction coefficient. Equation (5.1) gives an idea of the difference between laminar and turbulent skin friction coefficients [31].

$$\begin{aligned} C_{f,laminar} &\approx \frac{0.664}{Re^{0.5}} \\ C_{f,turbulent} &\approx \frac{0.0583}{Re^{0.2}} \end{aligned} \tag{5.1}$$

The theoretical expression of the skin friction coefficient is obtained by the ratio of wall shear stress, density and velocity: $C_f = \dfrac{2\tau_w}{\rho U^2}$.

Pressure coefficient

During both the steady and the unsteady measurements the stagnation pressure was found to have a physically incorrect value of $C_p = 1.2$. Following Bernoulli's equation for incompressible flow where $\rho = \rho_\infty$, this raises questions.

$$C_p = \frac{p - p_\infty}{\frac{1}{2}\rho U_\infty^2} = \frac{\frac{1}{2}\rho(U_\infty^2 - U^2)}{\frac{1}{2}\rho U_\infty^2} = 1 - \left(\frac{U}{U_\infty}\right)^2 \tag{5.2}$$

As equation (5.2) shows, C_p at the stagnation point, where the velocity U is zero, must be equal to one. To trace down this error, the experimental set-up was checked after the measurements. It was found that a misalignment of the Pitot tube with the incoming airflow was the cause of this offset in pressure distribution. To compensate for this, the entire distribution is shifted upwards by $+0.2$ in order to get the stagnation pressure equal to unity and have a fair comparison with the simulations. The effect of this shift on the integral loads is found to be negligible.

An additional error discovered after the measurements was that five pressure tabs on the suction side near the trailing edge had been switched during the preparation of the wing.

The five tabs are highlighted with a black circle in Figure 5.9a and 6.7a. For the upper surface trailing edge measurements to make more sense, the order of the tabs from left to right has to be switched.

5.1.2 Unsteady measurements

The experimental unsteady $C_l(\alpha)$ loops are visualised in Figures 5.2 to 5.5. The left hand side figures represent a tripped boundary layer and the figures on the right a free transition.

Angle of attack: $\alpha = 0°$

In Figure 5.2, the difference between free and forced transition is rather small, as it is in the steady lift polars in Figure 5.1a. The forced transition measurements have slightly wider loops, indicating that the unsteady effects are larger.

Angle of attack: $\alpha = 4°$

Again, Figure 5.3, shows no remarkable difference between free and forced transition apart from the afore mentioned effect. What can be clearly seen, however, is that the free flow reattaches about one degree earlier in the down stroke. Additionally the earlier reattachment point corresponds to a higher C_l value of approximately 0.1. An increase in frequency shifts the reattachment point backwards by approximately half a degree.

Angle of attack: $\alpha = 8°$

For the mean angle of attack plots corresponding to the stall angle in Figure 5.4, the same can be said as before. An additional effect is that the loops stop being linear and start to curve, this can clearly be seen for the lower plots with an amplitude of 8 degrees.

Angle of attack: $\alpha = 12°$

The highest mean angle of attack of 12 degrees shows fully separated flow loops in Figure 5.5. A noticeable difference is the slope of the loops for the free and forced cases, following the steady polars in Figure 5.1a, where the free polar shows a steeper slope. Again the loops are wider for forced transition and lift values are lower. However, in the case of 8 degrees amplitude, going up to a maximum angle of attack of 20 degrees, this difference reduces and the loops are much alike, especially for the higher reduced frequency $k = 0.0628$.

5.2 Simulations

This section is divided into steady results and unsteady results, a free boundary layer transition and a forced transition. The CFD results are only simulated for a forced boundary

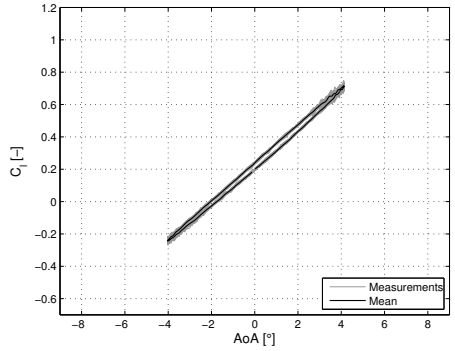

(a) Forced $\alpha = 0°$, $\Delta\alpha = 4°, k = 0.0314$.

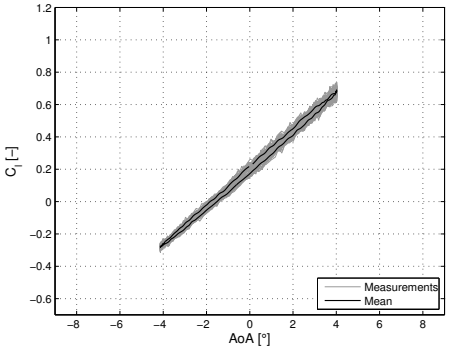

(b) Free $\alpha = 0°$, $\Delta\alpha = 4°, k = 0.0314$.

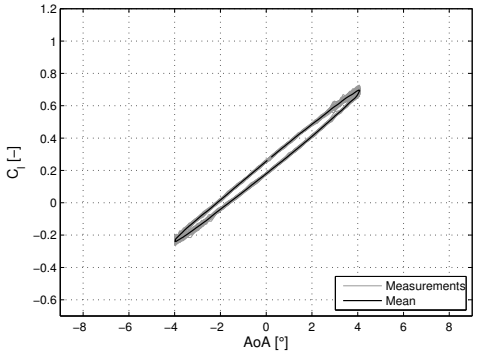

(c) Forced $\alpha = 0°$, $\Delta\alpha = 4°, k = 0.0628$.

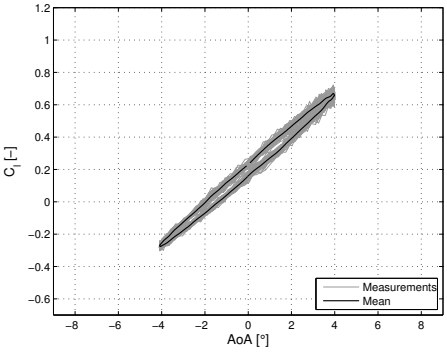

(d) Free $\alpha = 0°$, $\Delta\alpha = 4°, k = 0.0628$.

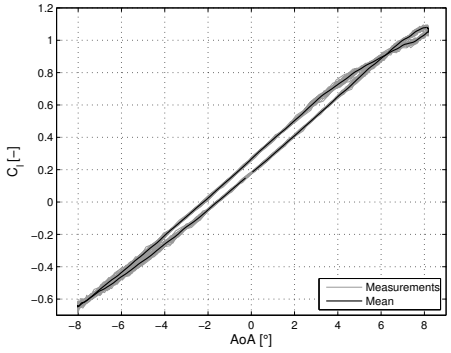

(e) Forced $\alpha = 0°$, $\Delta\alpha = 8°, k = 0.0314$.

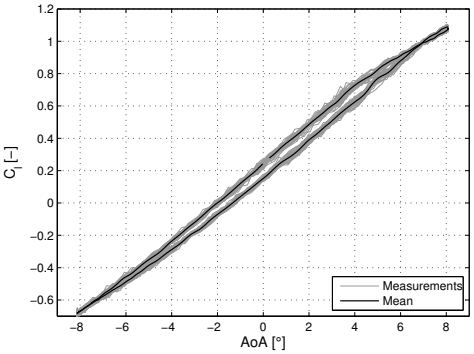

(f) Free $\alpha = 0°$, $\Delta\alpha = 8°, k = 0.0314$.

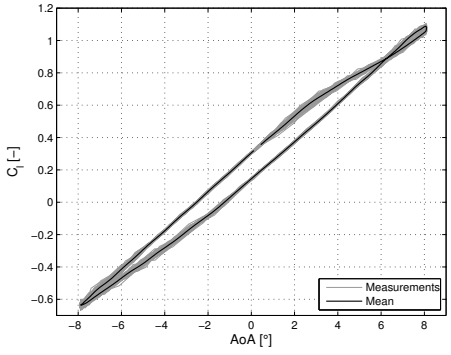

(g) Forced, $\alpha = 0°$, $\Delta\alpha = 8°, k = 0.0628$.

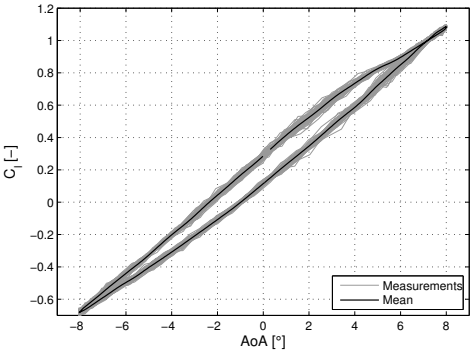

(h) Free, $\alpha = 0°$, $\Delta\alpha = 8°, k = 0.0628$.

Figure 5.2: *Experimental $C_l(\alpha)$ for $\alpha = 0°$, $\Delta\alpha = 4°, 8°$, $k = 0.0314, 0.0628$. Forced transition left and free transition right.*

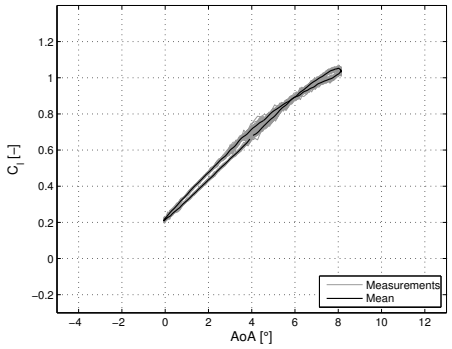

(a) Forced $\alpha = 4°$, $\Delta\alpha = 4°, k = 0.0314$.

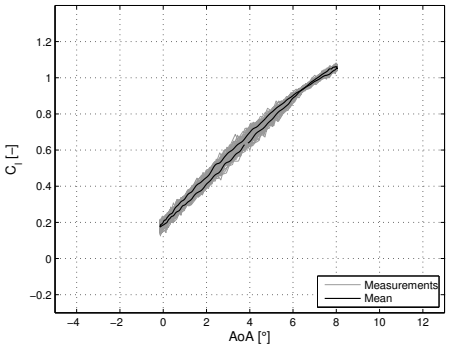

(b) Free $\alpha = 4°$, $\Delta\alpha = 4°, k = 0.0314$.

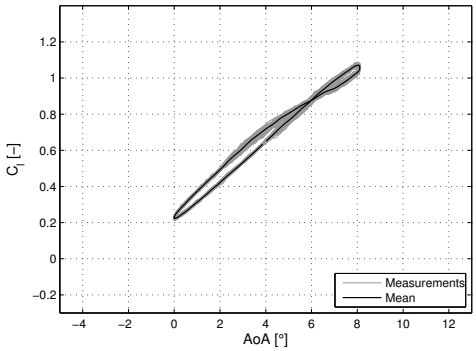

(c) Forced $\alpha = 4°$, $\Delta\alpha = 4°, k = 0.0628$.

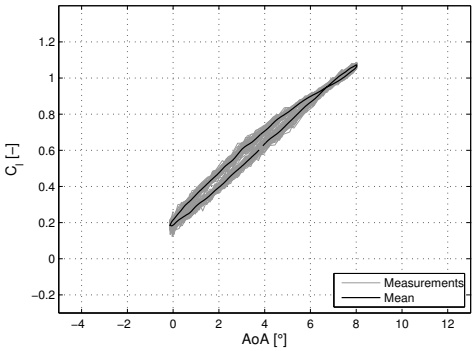

(d) Free $\alpha = 4°$, $\Delta\alpha = 4°, k = 0.0628$.

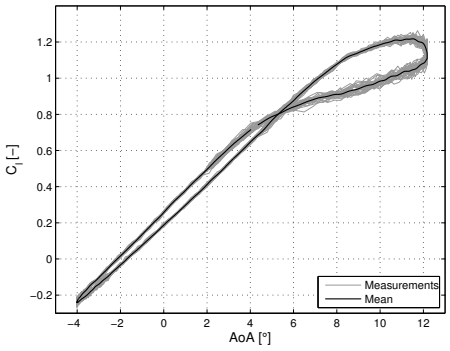

(e) Forced $\alpha = 4°$, $\Delta\alpha = 8°, k = 0.0314$.

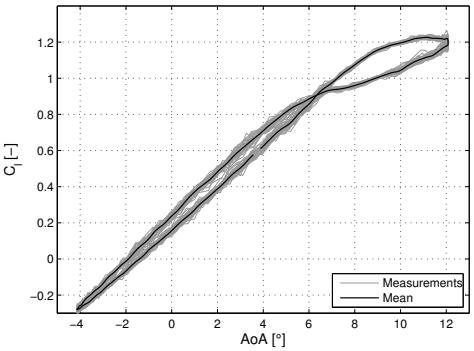

(f) Free $\alpha = 4°$, $\Delta\alpha = 8°, k = 0.0314$.

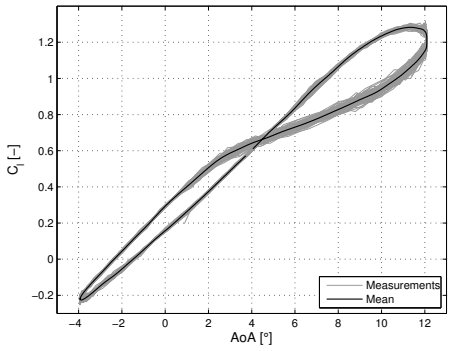

(g) Forced $\alpha = 4°$, $\Delta\alpha = 8°, k = 0.0628$.

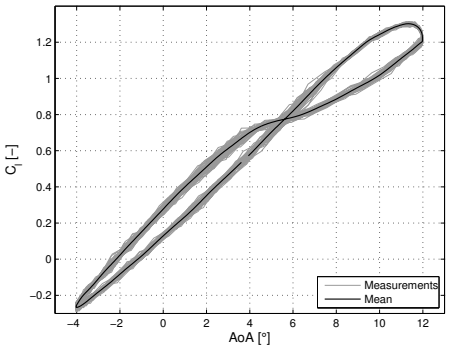

(h) Free $\alpha = 4°$, $\Delta\alpha = 8°, k = 0.0628$.

Figure 5.3: *Experimental $C_l(\alpha)$ for $\alpha = 4°$, $\Delta\alpha = 4°, 8°$, $k = 0.0314, 0.0628$. Forced transition left and free transition right.*

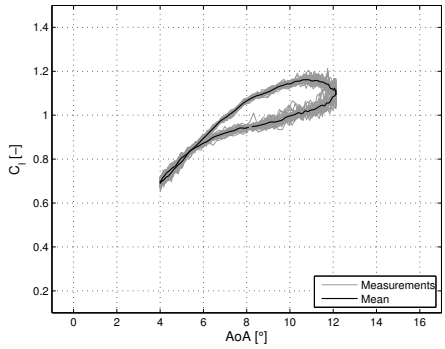

(a) Forced $\alpha = 8°$, $\Delta\alpha = 4°, k = 0.0314$.

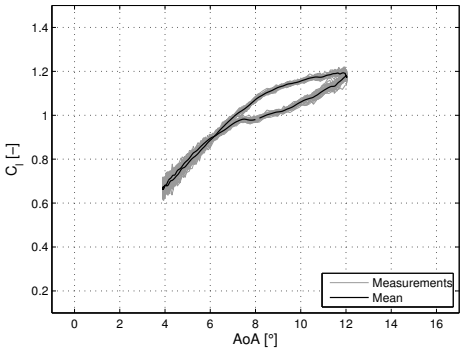

(b) Free $\alpha = 8°$, $\Delta\alpha = 4°, k = 0.0314$.

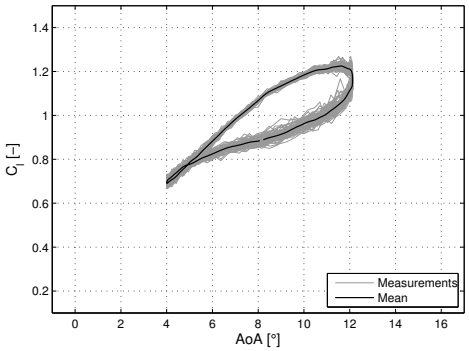

(c) Forced $\alpha = 8°$, $\Delta\alpha = 4°, k = 0.0628$.

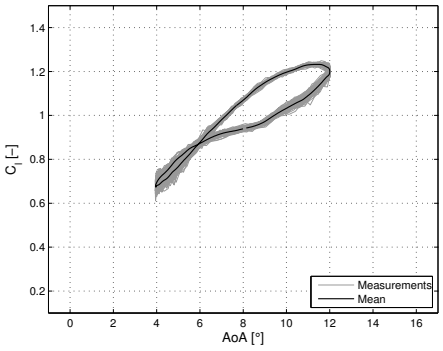

(d) Free $\alpha = 8°$, $\Delta\alpha = 4°, k = 0.0628$.

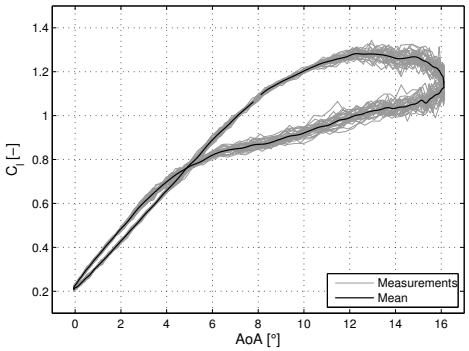

(e) Forced $\alpha = 8°$, $\Delta\alpha = 8°, k = 0.0314$.

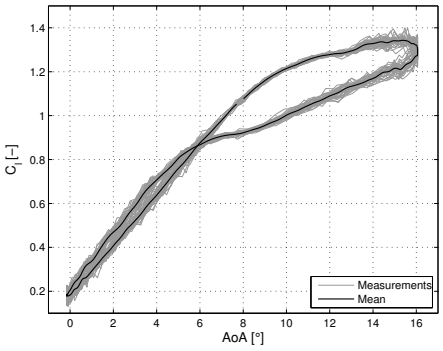

(f) Free $\alpha = 8°$, $\Delta\alpha = 8°, k = 0.0314$.

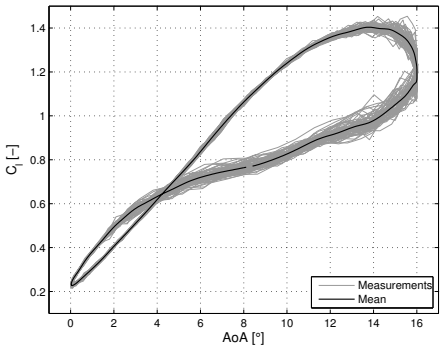

(g) Forced $\alpha = 8°$, $\Delta\alpha = 8°, k = 0.0628$.

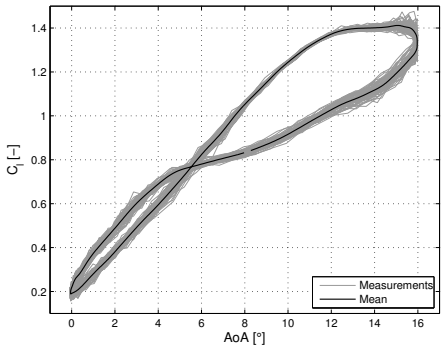

(h) Free $\alpha = 8°$, $\Delta\alpha = 8°, k = 0.0628$.

Figure 5.4: *Experimental $C_l(\alpha)$ for $\alpha = 8°$, $\Delta\alpha = 4°, 8°$, $k = 0.0314, 0.0628$. Forced transition left and free transition right.*

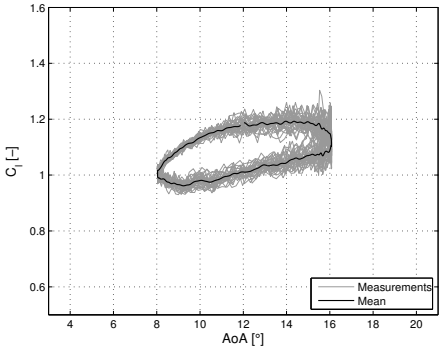

(a) Forced $\alpha = 12°$, $\Delta\alpha = 4°, k = 0.0314$.

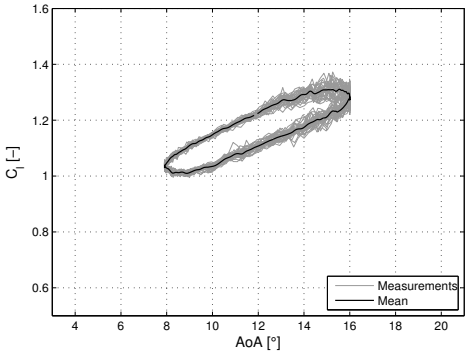

(b) Free $\alpha = 12°$, $\Delta\alpha = 4°, k = 0.0314$.

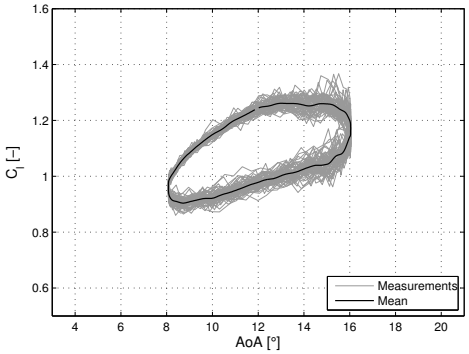

(c) Forced $\alpha = 12°$, $\Delta\alpha = 4°, k = 0.0628$.

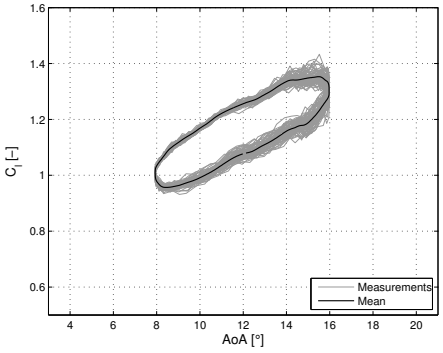

(d) Free $\alpha = 12°$, $\Delta\alpha = 4°, k = 0.0628$.

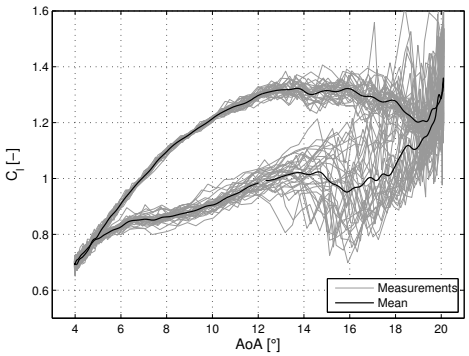

(e) Forced $\alpha = 12°$, $\Delta\alpha = 8°, k = 0.0314$.

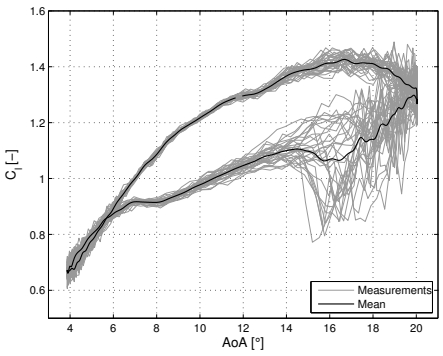

(f) Free $\alpha = 12°$, $\Delta\alpha = 8°, k = 0.0314$.

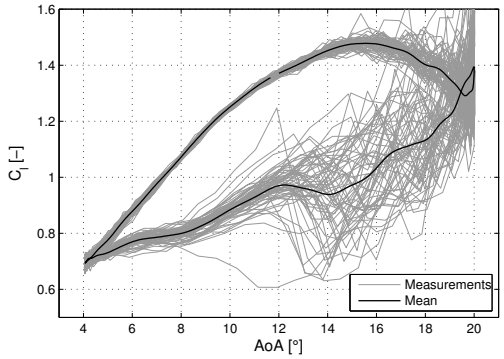

(g) Forced $\alpha = 12°$, $\Delta\alpha = 8°, k = 0.0628$.

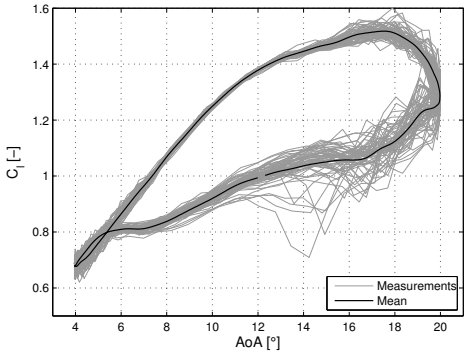

(h) Free $\alpha = 12°$, $\Delta\alpha = 8°, k = 0.0628$.

Figure 5.5: *Experimental $C_l(\alpha)$ for $\alpha = 12°$, $\Delta\alpha = 4°, 8°$, $k = 0.0314, 0.0628$. Forced transition left and free transition right.*

layer transition because a working transition model has not yet been implemented into the used OpenFOAM version. First it is required to validate the simpler forced transition model, which partly, is the aim of this study.

All Q^{3}UIC and OpenFOAM simulations are performed with a flap angle of $\beta = -3^\circ$ because during the post processing of the data and after checking the set-up it was found that the flap had not been set to a zero deflection angle. Remarkable is that, for Q^{3}UIC, the free transition measurements compare well with the applied flap correction whereas for the tripped transition measurements the flap correction seems to make Q^{3}UIC under predict all lift values. The reason for this remains unclear. An overview of the Q^{3}UIC input parameters that are used for the simulations is given in Table 5.1.

Table 5.1: *Q^{3}UIC main inputs parameters.*

Input	**Free transition**	**Tripped transition**
Re	$4.18 \cdot 10^5$	
Lower transition	37	59
Upper transition	110	82
Turbulence intensity	0.0022	
dtU	0.4	
Kutta condition	(1): $U_1^2 - U_n^2 + 2d\Gamma/dt$	
Boundary layer trip	OFF	ON
Reduced frequency	[0.0314, 0.0628]	
Mean AoA	[0, 4, 8, 12]	
AoA amplitude	[4, 8]	
Flap angle	-3	
Tunnel walls	ON	
IBL flag	ON	

In the Q^{3}UIC version that is used for the simulations in this chapter, there was a bug in the way the pressure drag is calculated, it was using the same approach as for a wind direction change instead of using changes in the airfoil motion. Therefore, any form of analysis and fair comparison based on drag could not be done.

5.2.1 Convergence study

For the OpenFOAM simulations, convergence studies are performed in order to get a appropriate mesh and time step.

Mesh

From C_x and C_y in Figure 5.7, it is clearly visible that the mesh study shows convergence for the two latter meshes of 40 and 80 thousand cells. The right most point is the mesh with 20 thousand cells and it can be deduced from the large difference of the steady state

value that the mesh is too coarse to resolve the flow. Finally the mesh with $N = 80000$ cells is chosen to do the simulations, primarily based on high mesh density requirements to successfully capture the flow behaviour for high angles of attack. For a visualisation of the meshes, see Figure 5.6.

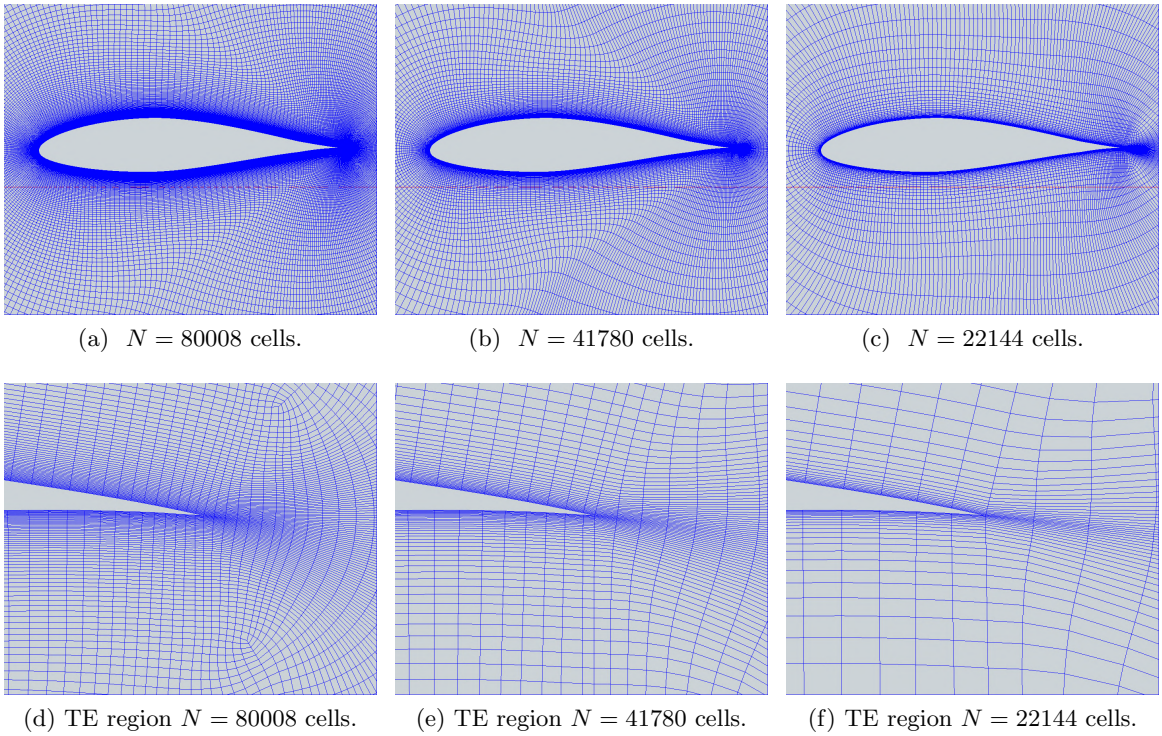

(a) $N = 80008$ cells. (b) $N = 41780$ cells. (c) $N = 22144$ cells.

(d) TE region $N = 80008$ cells. (e) TE region $N = 41780$ cells. (f) TE region $N = 22144$ cells.

Figure 5.6: *Sparsity of meshes used for mesh convergence study on NACA 64-418.*

Table 5.2 summarises the variables that were changed in order to perform a systematic mesh convergence study. The main varying parameters are the number of surface points on the airfoil and the growth rate of the cells. The initial cell size for the grid generation tool Pointwise is calculated using a standard chord of 1 m. This cell size is larger than the one used for the simulations in OpenFOAM. Since the chord of the experimental model was 0.25 m, the cell size – keeping Re the same – changes. The outcome is obtained using the y^+ calculator [32] and the equations have been discussed in Section 4.2.5.

Special care is taken to match the form and size of the cells at the transitions between the different domains. As shown in Table 5.2 the mesh is split into three domains to reduce the amount of high aspect ratio cells with high skewness.

- **Boundary layer domain**: from the first cell to the edge of the farfield domain. Fine cells are needed to resolve the boundary layer.
- **Trailing edge domain**: This region is generated to get a good mesh quality and to serve as a bridge between the boundary layer and farfield domain.
- **Farfield domain**: From the edge of the boundary layer and trailing edge domain to the outer edge of the circular domain with a radius of approximately 80 chords.

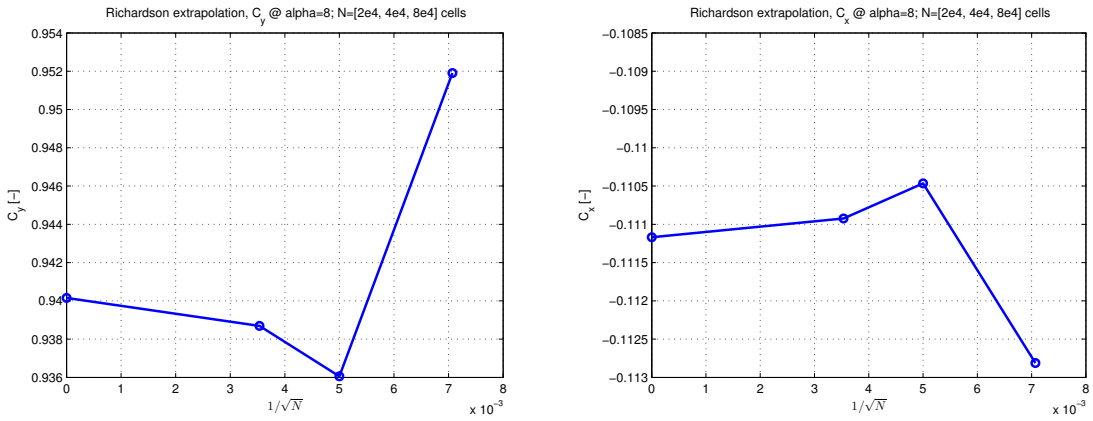

(a) C_y component.

(b) C_x force component.

Figure 5.7: *Values of steady C_y and C_x components for meshes with $N \approx$ [2e4; 4e4; 8e4; ∞] cells.*

Table 5.2: *Mesh variables NACA 64-618 used for convergence study in Pointwise.*

	Number of cells N	**N=80008**	**N=41780**	**N=22144**
General	Surface points	2×128	2×64	2×32
	TE & LE spacing	0.00075	0.0015	0.003
	Initial cell size	5×10^{-5} m	5×10^{-5} m	5×10^{-5} m
	Growth rate	1.05	1.1	1.2
	Farfield radius	79c	86c	85c
BL domain	Steps	50	40	30
	Growth rate	1.05	1.1	1.2
TE domain	Steps	7	6	3
	Growth rate	1.05	1.1	1.2
Farfield domain	Initial cell size	0.006	0.0018	0.009
	Steps	181	90	43
	Growth rate	1.05	1.1	1.2

Time step

In order to obtain the most suitable time step for running the simulations, first variable time steps were studied by specifying a maximum Courant number and letting the solver decide which time step is needed within the specified range. An initial time step is specified together with a maximum Courant number which is not be exceeded. This method is more efficient because larger time steps can be used where the flow behaviour is less complex, reducing computational time. However, for post-processing and stability reasons it is chosen to work with a fixed time step. Despite the fact that it is less efficient in terms of computational time, the benefits of this method outweigh the drawbacks.

Based on previous runs, an approximate suitable time step was known and the simulations were done for 4×10^{-5} s, which – in a particular case – proved not to be accurate enough in terms of capturing flow oscillations in the separated region. The 2.5×10^{-5} s time step showed better results and was chosen to run the simulations with.

5.2.2 Steady results

During the experimental stage, the steady lift curves are obtained for an angle of attack range of $-10° < \alpha < 25°$. It was found that Q^{3}UIC had convergence problems and crashed slightly above $\alpha = 20°$, so that is where the simulations were stopped.

Free boundary layer transition, Q^{3}UIC

From Figure 5.8a it follows that the lift curves show good agreement in the linear region up to $\alpha = 9°$, where $C_{l,max}$ is reached and slightly over predicts the lift value at that angle. The simulated curve stalls earlier and shows large deviations from the experimental data until $\alpha = 20°$. After stall, the lift curve stays almost constant from 12° to 20°. This under prediction is probably caused by an improper calculation of the exact locations where transition and separation occur, see Figure 5.8b. The relation between the stall of the lift curve and the upstream movement of the separation location after approximately $\alpha = 9°$ becomes apparent by studying Figure 5.8.
For increasing α, the transition location on the suction side moves upstream from a initial chord–wise location of approximately 60%, the rate at which this happens may be off by an inaccurate prediction of the boundary layer thickness. An alternative explanation may be related to the applied wall correction.

Comparing the pressure distributions in Figure 5.9 it is visible that the deviations are relatively large. This is believed to be caused by a misalignment of the Pitot tube with the incoming flow. Despite the fact that the entire experimental curve is shifted upwards by 0.2, the distributions still do not match as they should. For each of the shown angles of attack, Q^{3}UIC seems to under predict continuously. For the comparison, the same angles of attack are chosen as the ones used to investigate the hysteresis loops in the unsteady flow measurements: $\alpha = [0°, 4°, 8°, 12°]$.
For the highest α in Figure 5.9d, an almost constant pressure is observed in the measurements starting roughly at $x/c = 0.6$. Simulations show something close to a constant

pressure from $x/c = 0.7$ onwards. The pressure difference between upper and lower surface is slightly smaller. As the difference between upper and lower surface pressure is a measure for the lift, an under prediction is obtained in this aft region. In Figure 5.9c the pressure peak is over predicted whereas Figure 5.9d shows an under prediction. Although the absolute values do not match, the overall shape and tendency of the curves seems to be in agreement.

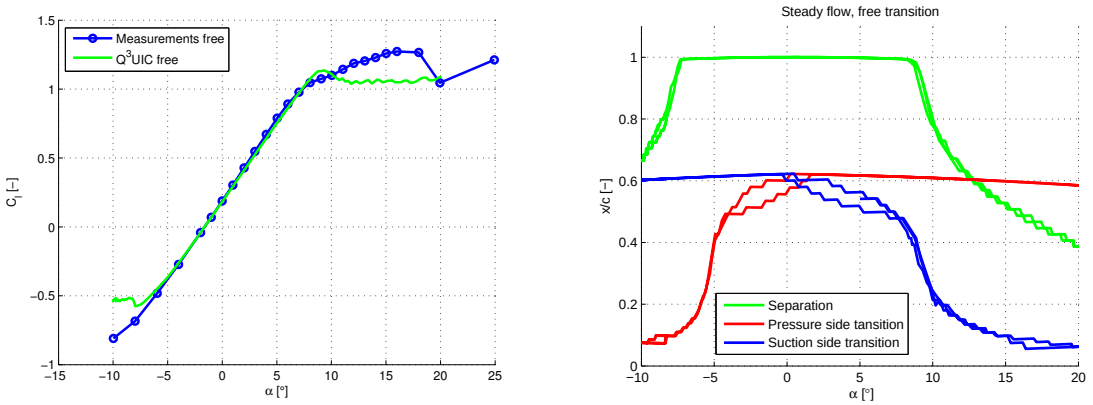

(a) Experimental and simulated steady lift curves for free boundary layer transition.

(b) Simulated separation and transition locations for a free boundary layer.

Figure 5.8: *Steady free boundary layer comparisons between lift, separation and transition.*

Forced boundary layer transition

Contrary to the free transition, the comparison in this section also includes the OpenFOAM simulations.

For Q^{3}UIC, the tripped boundary layer measurements show similar results to the free boundary layer transition with regards to under-prediction of the steady lift curve as shown in Figure 5.10a. The maximum relative difference between measurements and simulations is smaller but the lift curve shows a continuous under-prediction except for negative α around –3° where the curves intersect.
In the simulations, the slope of the separation location curve in Figure 5.10b is more gradual than for the free transition case in Figure 5.8b. This is to be expected since the boundary layer is turbulent, hence less prone to sudden separation due to more mixing with the outer inviscid flow. For C_l, this translates into a curve that gradually grows without a sudden drop in lift as can be observed in Figure 5.8a. However, the absolute lift value is lower due to an early transition and less efficient lift caused by an over prediction of the boundary layer thickness.

OpenFOAM's steady lift curve shows an almost identical behaviour to Q^{3}UIC up to the point that Q^{3}UIC starts to stall at approximately 8 degrees. Beyond this angle, the Q^{3}UIC slope levels out while OpenFOAM does not meet its stall angle before 10 degrees.

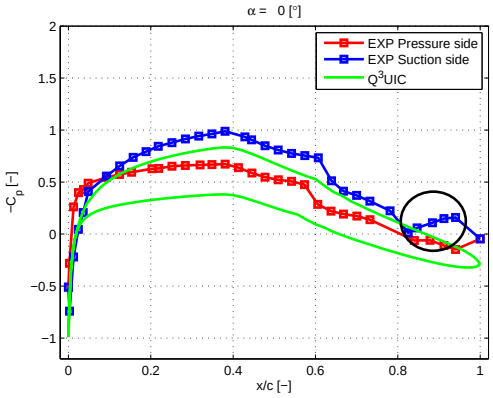

(a) Pressure distribution at $\alpha = 0°$

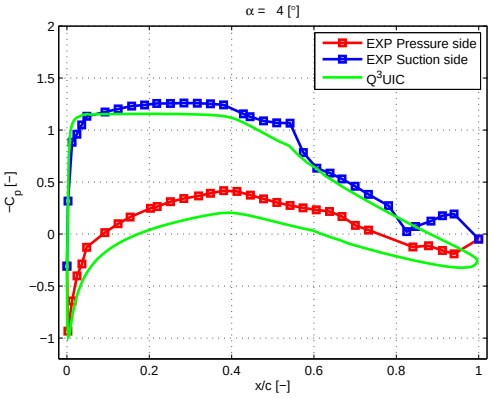

(b) Pressure distribution at $\alpha = 4°$

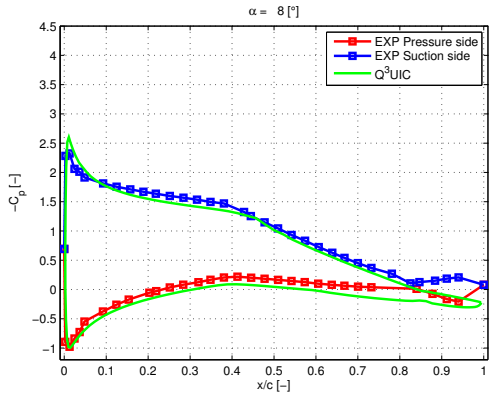

(c) Pressure distribution at $\alpha = 8°$

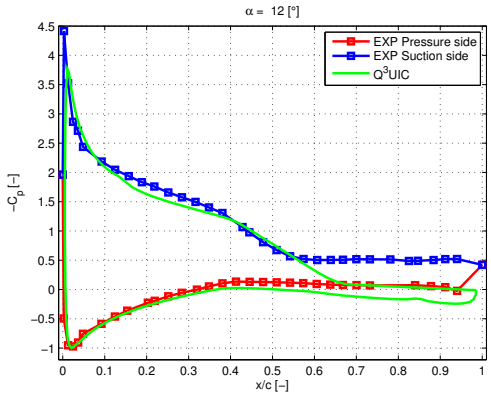

(d) Pressure distribution at $\alpha = 12°$

Figure 5.9: *Pressure coefficient over airfoil for* $\alpha = [0°, 4°, 8°, 12°]$ *and a free boundary layer transition.*

Based on the slopes and deviation beyond 8 degrees of the numerical polars, it can be said that the way in which the experimental boundary layer is tripped can have a large influence on the resulting polar. Most probably, a more sophisticated trip wire, would have yielded a more gradual slope, resembling the numerical solutions more accurately.

Figure 5.11, shows an under-prediction for nearly all angles of attack shown. However, for $\alpha = 12°$ in Figure 5.11d, Q^{3}UIC shows an overshoot in a small region just after the leading edge and a slightly larger region between $0.3c$ and $0.5c$.
OpenFOAM also under predicts consistently, even more so than Q^{3}UIC. This all is in line with the steady polars, of which the experimental curve, stays on top up to 9 degrees, where OpenFOAM crosses. At 12 degrees, apart from the suction peak at the leading edge, the suction side pressures of the simulations are almost identical up to $x/c = 0.55$. The OpenFOAM pressure side experiences higher pressures up to approximately the same chord-wise location.

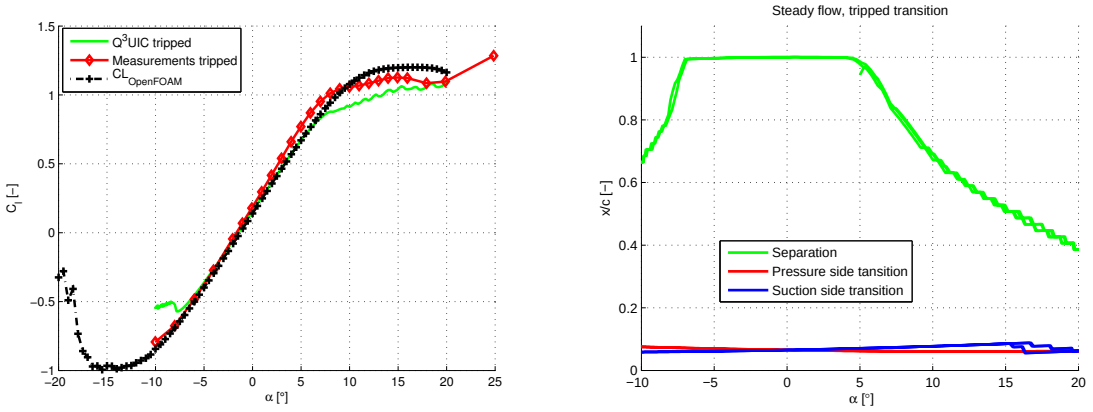

(a) Experimental and simulated steady lift curves for tripped boundary layer transition.

(b) Simulated separation and transition locations for tripped boundary layer.

Figure 5.10: *Steady tripped boundary layer comparisons between lift, separation and transition.*

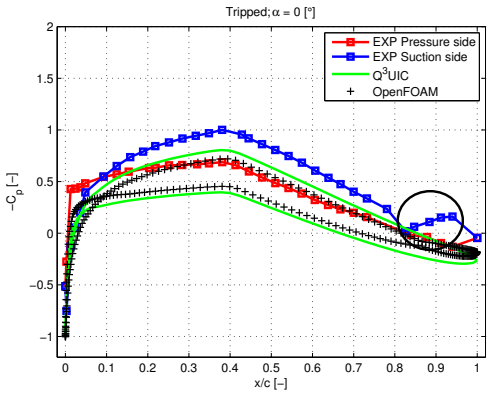

(a) Pressure distribution at $\alpha = 0°$

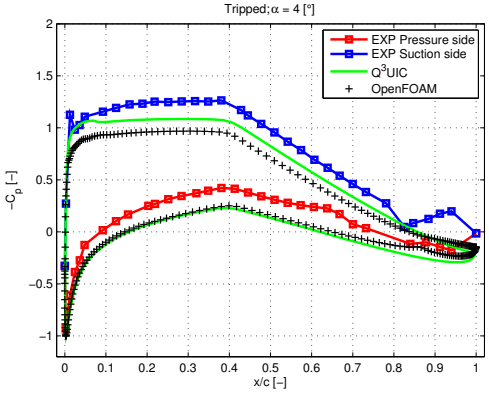

(b) Pressure distribution at $\alpha = 4°$

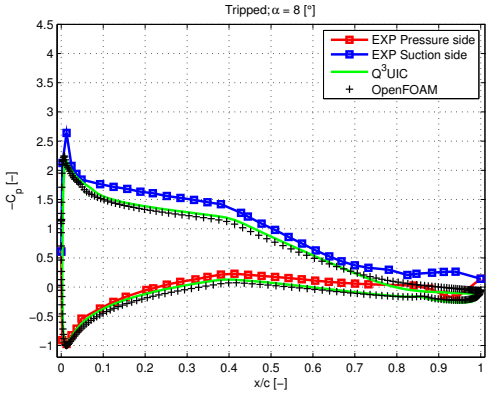

(c) Pressure distribution at $\alpha = 8°$

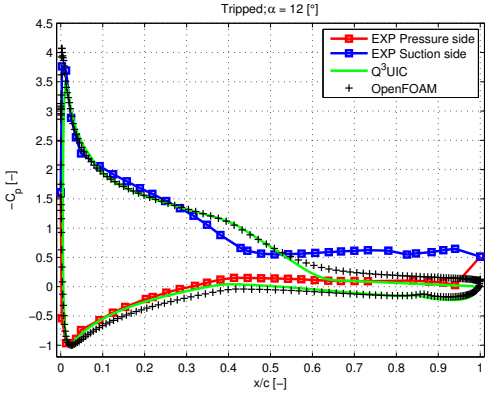

(d) Pressure distribution at $\alpha = 12°$

Figure 5.11: *Pressure coefficient over airfoil for* $\alpha = [0°, 4°, 8°, 12°]$ *and a tripped boundary layer transition.*

5.2.3 Unsteady results

Angle of attack: $\alpha = 0°$

Looking globally at the zero angle of attack case in Figure 5.12, the first noticeable thing is the offset in slope between measurements and simulations for the tripped transition. Numerically there seems to be little difference apart from the offset. Looking more closely though, the experimental loop, transitions to separated flow just above 6 degrees, resulting in a small clock-wise $C_l(\alpha)$ loop, which reattaches again in the down-stroke at the same 6 degree angle of attack. Q^{3}UIC captures this behaviour accurately by calculating when the skin friction coefficient C_f drops below zero, and as such predicting separation location. OpenFOAM does not capture this and displays a fully attached flow loop for both amplitudes. In Figure 5.12e, there is one large attached flow region around the mean angle of attack and two small separated regions at the extremities. Apart from the difference in slope, Q^{3}UIC manages to capture this effect to a high accuracy.

The free measurements on the right of Figure 5.12 also show a, somewhat smaller, separated region for Figures 5.2f and 5.2h. This time, Q^{3}UIC does not succeed to capture the separated region, because the boundary layer thickness is probably underestimated causing a delay in transition. As such, not entering flow separation. The free transition results from Q^{3}UIC do not show the offset in slope and have a better overlap with the measurements than in the forced transition cases.

Angle of attack: $\alpha = 4°$

In Figure 5.13 OpenFOAM shows a small region of separated flow for Figure 5.13a. As the frequency increases this diminishes, and by increasing the amplitude, deviations grow further. It seems like $\alpha = 8°$ is the limiting angle of attack for OpenFOAM as it is not capable of resolving the physics properly. Again, for the lower frequency of $k = 0.0314$ in Figure 5.13e there is a small separated flow region at $\alpha = 12°$ which disappears as the frequency is increased to $k = 0.0628$ in Figure 5.13g.

Q^{3}UIC shows, in relation to the measurements, early separation points in the tripped cases and retarded separation points in the free cases. This can again be explained by an estimation of the boundary layer thickness which is not accurate enough and by inaccurate closure equations of the transition model

Angle of attack: $\alpha = 8°$

Figure 5.14 shows the unsteady loops around the 8 degree mean angle of attack, where flow conditions are complex and proved to be extremely challenging to model accurately in OpenFOAM. The unsteady effects seem to be nearly absent regarding lift differences for the up- and down-stroke.

A more detailed analysis with respect to pressure distributions is performed on Figure 5.14g in Section 5.3. This angle of 8 degrees is on the border of varying attached and separated flow conditions, and is close to $C_{l,max}$. Where Q^{3}UIC shows acceptable and nearly identical shapes to the experimental loops, OpenFOAM fails in all aspects except

for the reattachment location in the down stroke close to the minimum angle of attack. Q^{3}UIC predicts a more severe drop in lift during the down-stroke, forcing the flow to reattach at lower angles of attack.

Again Q^{3}UIC shows a consistent behaviour in delaying the reattachment point for forced transition and a retarded separation point for free transition. Only Figure 5.14h does not comply with this statement as the separation in this case is advanced.

Q^{3}UIC predicts a more severe drop of lift in the down stroke, forcing the flow to reattach at lower angles of attack then found in the measurements for Figures 5.14c and 5.14g.

Angle of attack: $\alpha = 12°$

As the highest mean angle of attack in Figure 5.15 is reached, OpenFOAM seems to have less difficulties in resolving the flow compared to $\alpha_m = 4°$. Despite the fact that the OpenFOAM results are still not accurate, the notion that this case performs better than for the previous case ($\alpha = 8°$), brings relief and narrows down the search to find a probable cause for the errors and inaccuracies. The slope and offset of the OpenFOAM loops can be traced back to the steady lift curve, which also exceeds both Q^{3}UIC and measurements. An over-estimation of the stall angle and $C_{l,max}$ is found in all the cases.

Q^{3}UIC under-predicts all lift values, in both free and forced transition, which is also in line with the steady lift polar in Figure 5.16a. The growing influence of separated flow regions at this angle of attack cause Q^{3}UIC to experience more difficulties of properly modelling the viscous effects.

5.3 Conclusive remarks

For convenience, all the steady lift polars are shown in Figure 5.16a, together with the influence of the wall correction on the lift values in Q^{3}UIC.

Looking at the pressure distributions in Figure 5.17a, there is no remarkable difference between the unsteady OpenFOAM up- and down-stroke pressure distributions as there is neither a big difference in the lift values at $\alpha = 14°$ in Figure 5.14g.
There is a higher suction peak present at the leading edge during the down-stroke, as can be seen by comparing Figures 5.18a and 5.18c. Also some dissimilarities are observed in the trailing edge region as the point of separation seems to move from $x/c \approx 0.9$ in the upstroke to $x/c \approx 0.75$ in the down-stroke. This effect also seems to take place in Figure 5.18, particularly for the turbulent kinetic energy fields Figures 5.18g and 5.18i. Here, a 'bubble' with a low turbulent kinetic energy seems to move upstream towards the leading edge, as the angle of attack increases.

To facilitate the analysis and comparison between steady pressure distributions and their unsteady counterparts during up- and down-stroke; the steady pressure distributions for approximately the same angle of attack are shown in Figure 5.17b. The distributions of Q^{3}UIC, OpenFOAM and measurements are plotted together. Q^{3}UIC and OpenFOAM seem to have more resemblance with each other than either of them to the experimental pressure distribution. This, however, does not seem to comply with the steady solution,

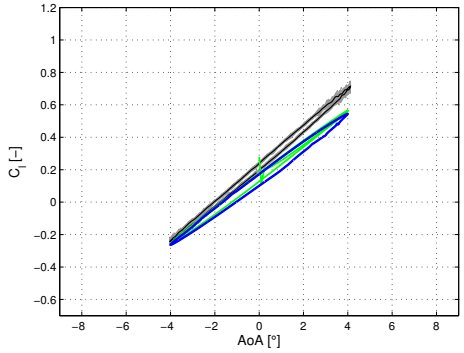

(a) Forced $\alpha = 0°$, $\Delta\alpha = 4°, k = 0.0314$.

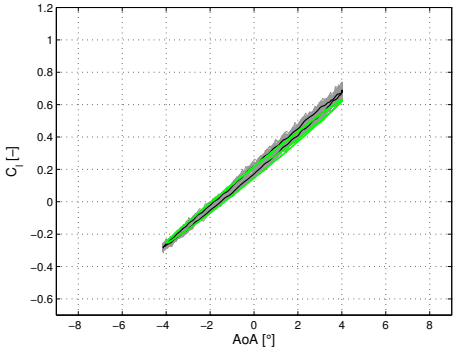

(b) Free $\alpha = 0°$, $\Delta\alpha = 4°, k = 0.0314$.

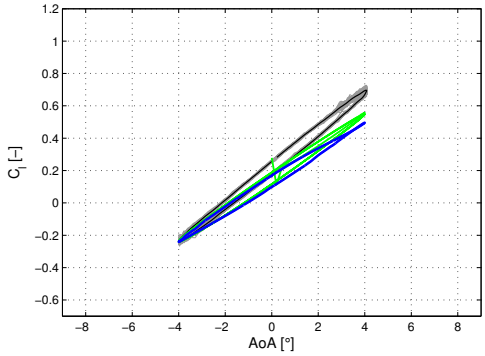

(c) Forced $\alpha = 0°$, $\Delta\alpha = 4°, k = 0.0628$.

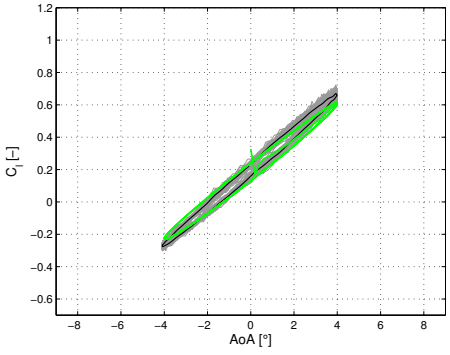

(d) Free $\alpha = 0°$, $\Delta\alpha = 4°, k = 0.0628$.

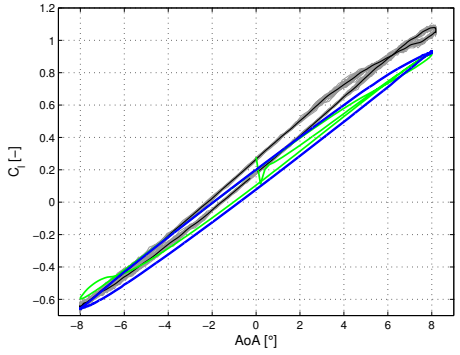

(e) Forced $\alpha = 0°$, $\Delta\alpha = 8°, k = 0.0314$.

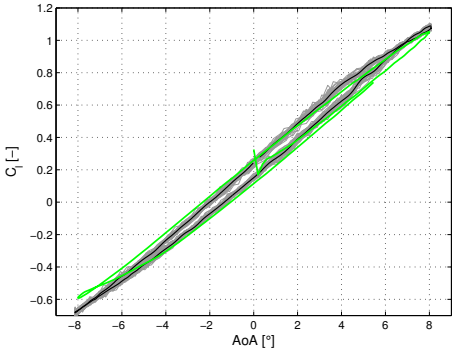

(f) Free $\alpha = 0°$, $\Delta\alpha = 8°, k = 0.0314$.

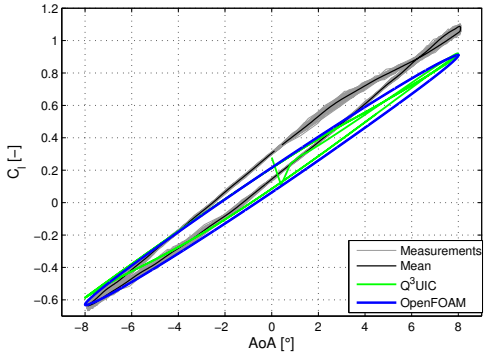

(g) Forced $\alpha = 0°$, $\Delta\alpha = 8°, k = 0.0628$.

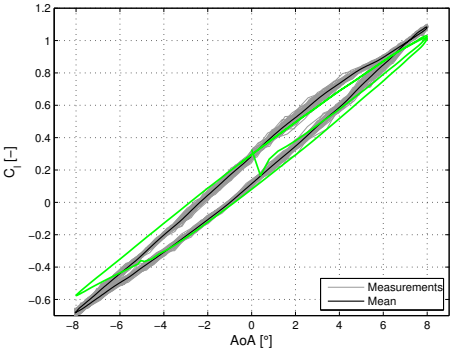

(h) Free $\alpha = 0°$, $\Delta\alpha = 8°, k = 0.0628$.

Figure 5.12: *Experimental and numerical $C_l(\alpha)$ for $\alpha = 0°$, $\Delta\alpha = 4°, 8°$, $k = 0.0314, 0.0628$. Forced transition left and free transition right.*

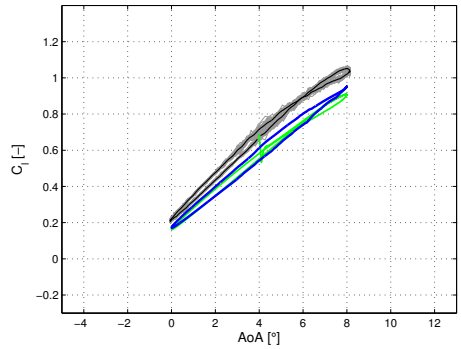

(a) Forced $\alpha = 4°$, $\Delta\alpha = 4°, k = 0.0314$.

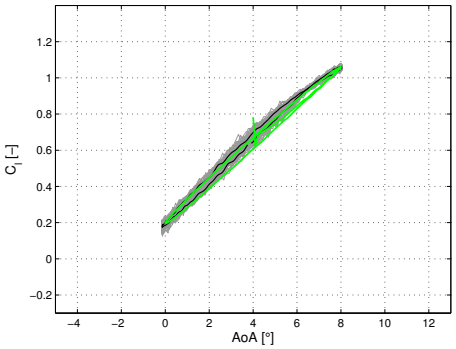

(b) Free $\alpha = 4°$, $\Delta\alpha = 4°, k = 0.0314$.

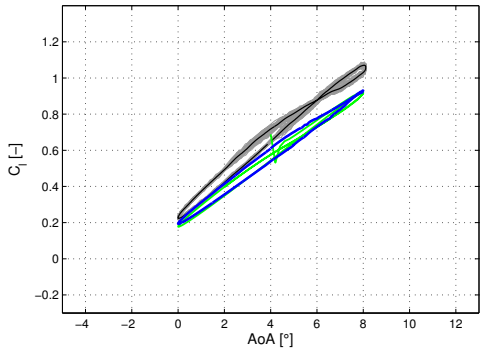

(c) Forced $\alpha = 4°$, $\Delta\alpha = 4°, k = 0.0628$.

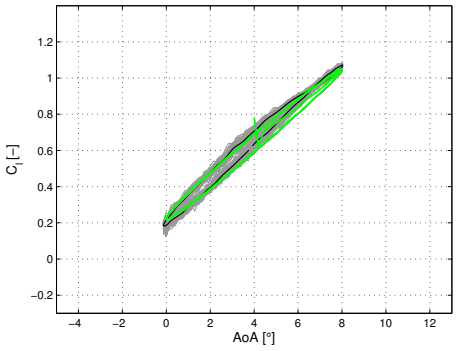

(d) Free $\alpha = 4°$, $\Delta\alpha = 4°, k = 0.0628$.

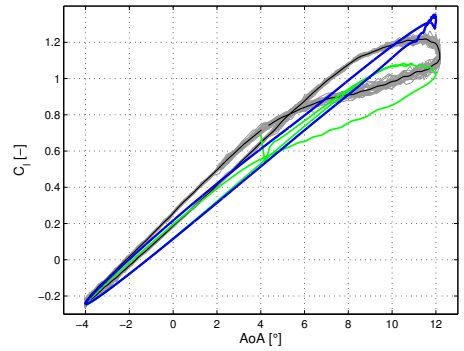

(e) Forced $\alpha = 4°$, $\Delta\alpha = 8°, k = 0.0314$.

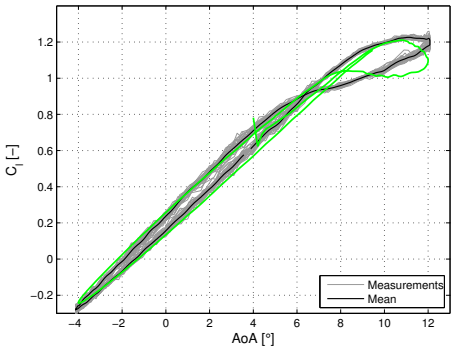

(f) Free $\alpha = 4°$, $\Delta\alpha = 8°, k = 0.0314$.

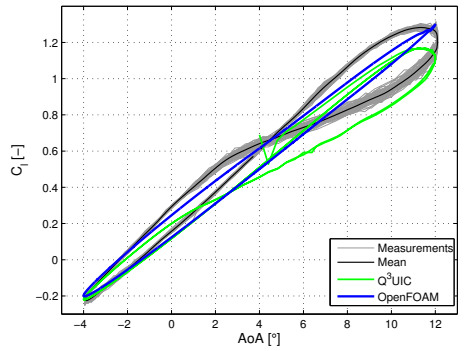

(g) Forced $\alpha = 4°$, $\Delta\alpha = 8°, k = 0.0628$.

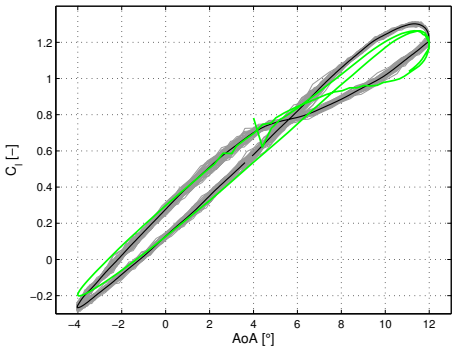

(h) Free $\alpha = 4°$, $\Delta\alpha = 8°, k = 0.0628$.

Figure 5.13: *Experimental and numerical $C_l(\alpha)$ for $\alpha = 4°$, $\Delta\alpha = 4°, 8°$, $k = 0.0314, 0.0628$. Forced transition left and free transition right.*

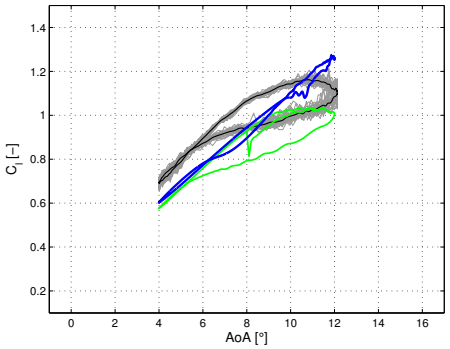

(a) Forced $\alpha = 8°$, $\Delta\alpha = 4°, k = 0.0314$.

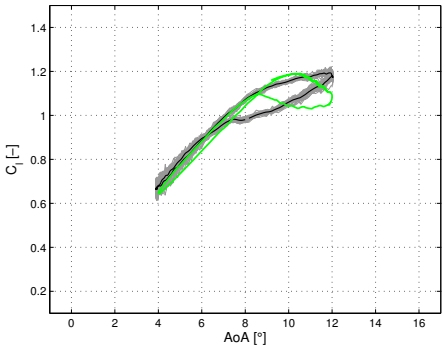

(b) Free $\alpha = 8°$, $\Delta\alpha = 4°, k = 0.0314$.

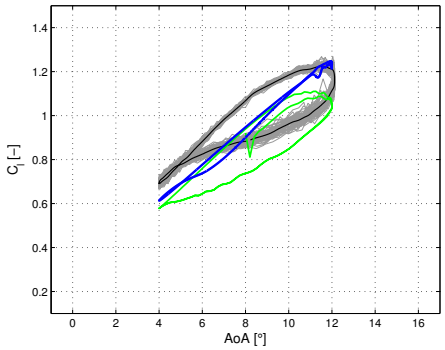

(c) Forced $\alpha = 8°$, $\Delta\alpha = 4°, k = 0.0628$.

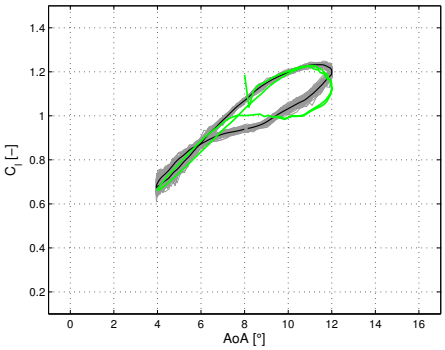

(d) Free $\alpha = 8°$, $\Delta\alpha = 4°, k = 0.0628$.

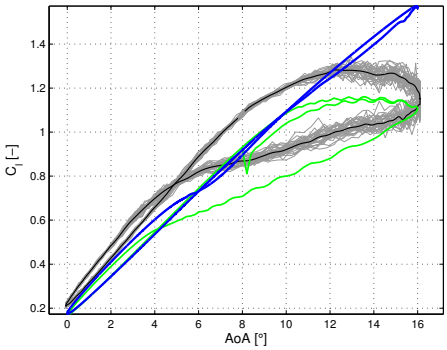

(e) Forced $\alpha = 8°$, $\Delta\alpha = 8°, k = 0.0314$.

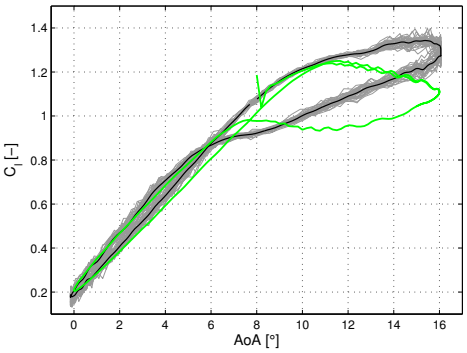

(f) Free $\alpha = 8°$, $\Delta\alpha = 8°, k = 0.0314$.

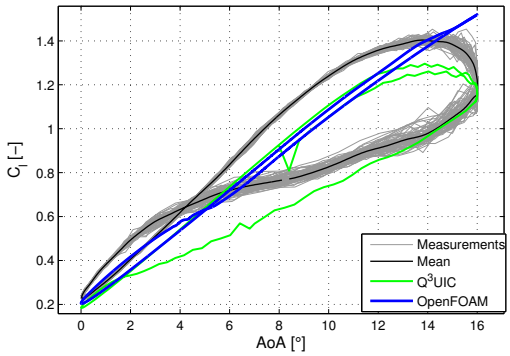

(g) Forced $\alpha = 8°$, $\Delta\alpha = 8°, k = 0.0628$.

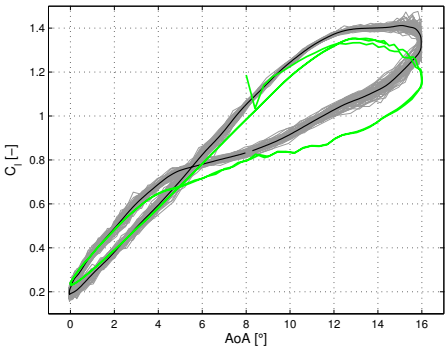

(h) Free $\alpha = 8°$, $\Delta\alpha = 8°, k = 0.0628$.

Figure 5.14: *Experimental and numerical $C_l(\alpha)$ for $\alpha = 8°$, $\Delta\alpha = 4°, 8°$, $k = 0.0314, 0.0628$. Forced transition left and free transition right.*

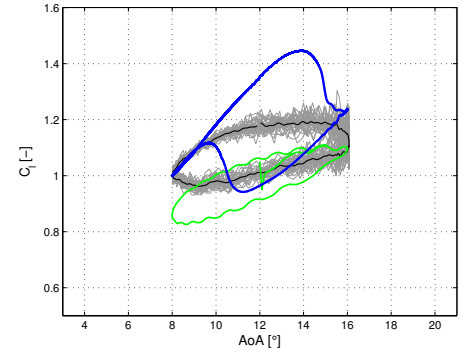

(a) Forced $\alpha = 12°$, $\Delta\alpha = 4°, k = 0.0314$.

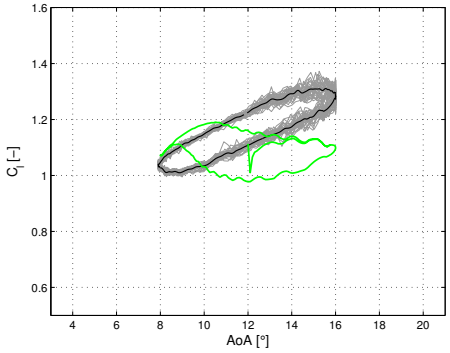

(b) Free $\alpha = 12°$, $\Delta\alpha = 4°, k = 0.0314$.

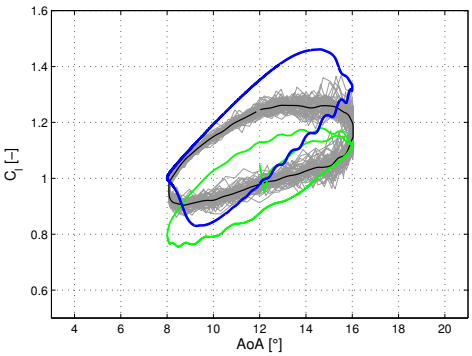

(c) Forced $\alpha = 12°$, $\Delta\alpha = 4°, k = 0.0628$.

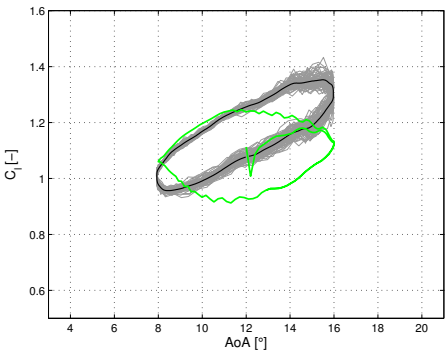

(d) Free $\alpha = 12°$, $\Delta\alpha = 4°, k = 0.0628$.

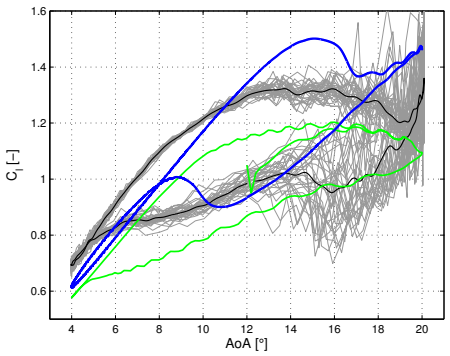

(e) Forced $\alpha = 12°$, $\Delta\alpha = 8°, k = 0.0314$.

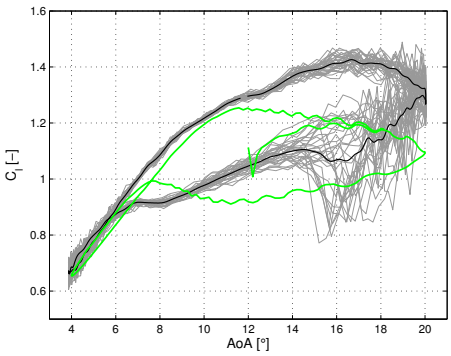

(f) Free $\alpha = 12°$, $\Delta\alpha = 8°, k = 0.0314$.

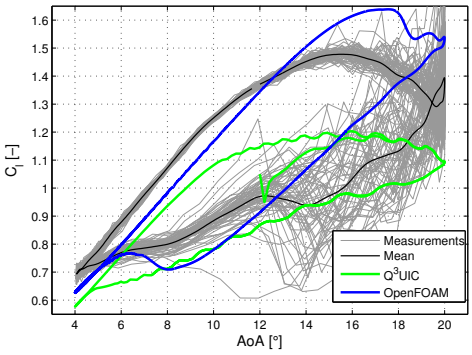

(g) Forced $\alpha = 12°$, $\Delta\alpha = 8°, k = 0.0628$.

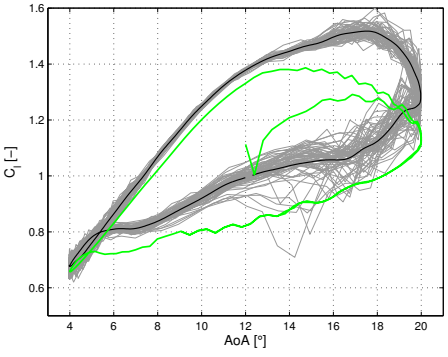

(h) Free $\alpha = 12°$, $\Delta\alpha = 8°, k = 0.0628$.

Figure 5.15: *Experimental and numerical $C_l(\alpha)$ for $\alpha = 12°$, $\Delta\alpha = 4°, 8°$, $k = 0.0314, 0.0628$. Forced transition left and free transition right.*

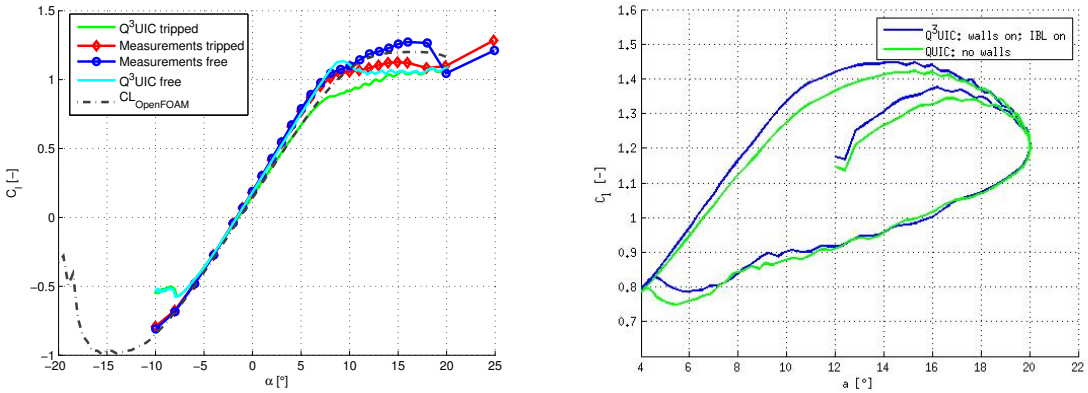

(a) NACA 64418, measured and simulated lift polars.

(b) Influence of wind tunnel walls effect in Q^{3}UIC results.

Figure 5.16: *All NACA 64-418 steady polars and effect of the wall correction in Q^{3}UIC.*

because at an angle of attack of 15 degrees, the experimental lift curve is situated between Q^{3}UIC and OpenFOAM curves.

In agreement with the steady polars in Figure 5.16a, the experimental pressure distributions in Figure 5.17b seem to indicate the largest difference between pressure and suction side, implying a larger lift force for the measurements. The difference between the measured up- and down-stroke in Figure 5.17a is considerably larger than the unsteady pressure distributions from OpenFOAM, adding to the explanation of the difference in lift values during up- and down-stroke in Figure 5.14g. Contrary to what is seen in the OpenFOAM pressure distributions – more suction during the up-stroke at $0.25 < x/c < 0.6$ – measurements show a much larger suction area during the down-stroke, almost over the entire upper surface of the wing.

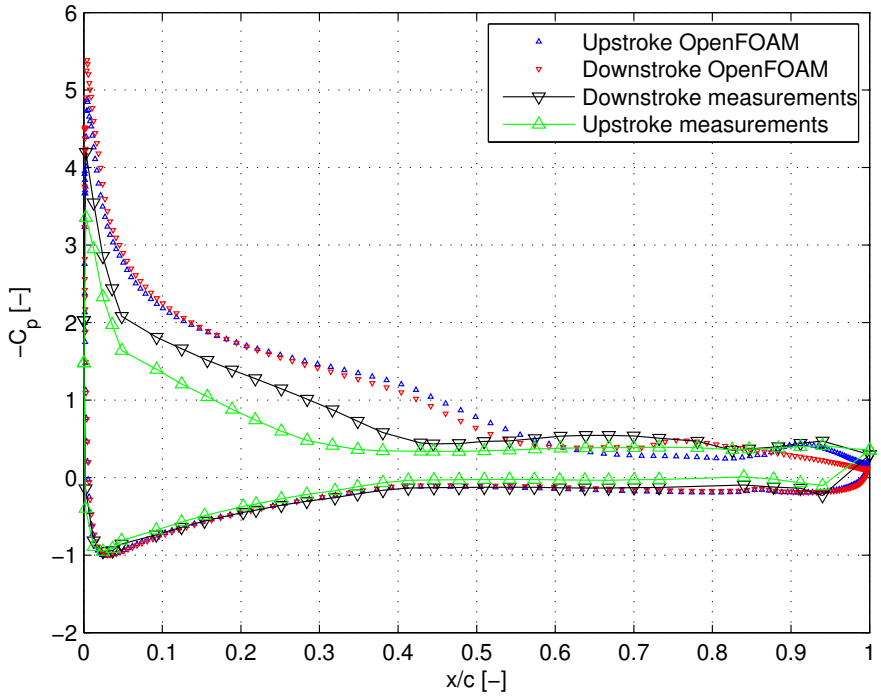

(a) Unsteady pressure distributions OpenFOAM and measurements. Up– and down-stroke at $\alpha \approx 14°$ from Figure 5.14g.

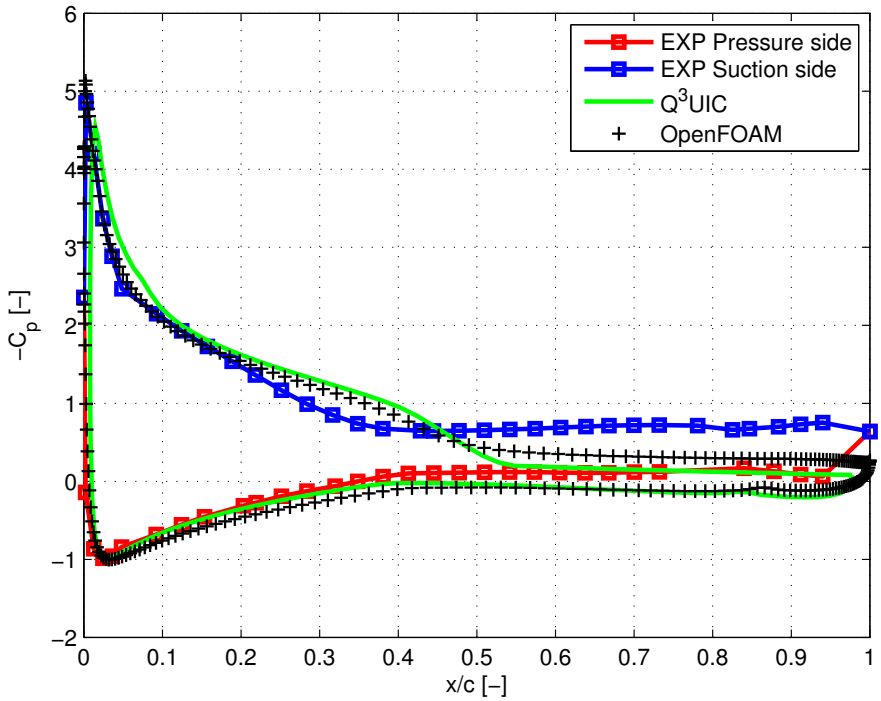

(b) Steady pressure distributions OpenFoam, Q^{3}UIC and measurements at $\alpha \approx 15°$.

Figure 5.17: *Steady and unsteady pressure distributions around 14-15 degrees.*

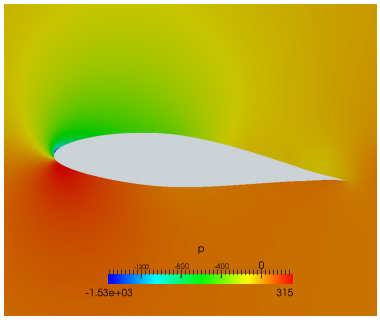

(a) Pressure field in the upstroke at $\alpha = 14°$.

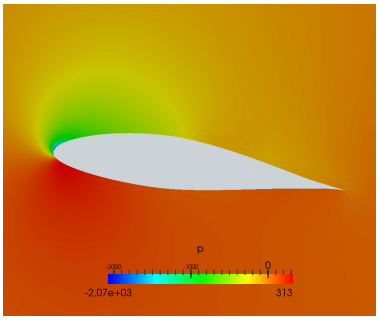

(b) Pressure field at maximum $\alpha = 16°$.

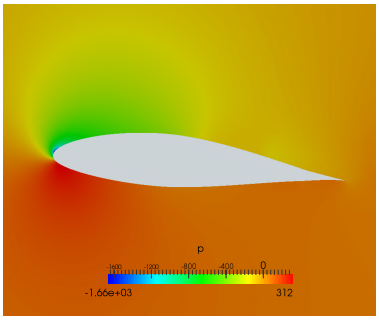

(c) Pressure field in the downstroke at $\alpha = 14°$.

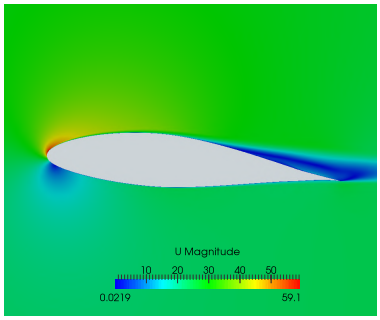

(d) Velocity field in the upstroke at $\alpha = 14°$.

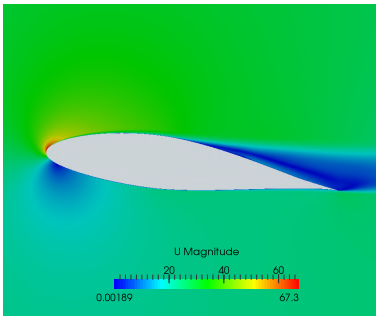

(e) Velocity field at maximum $\alpha = 16°$.

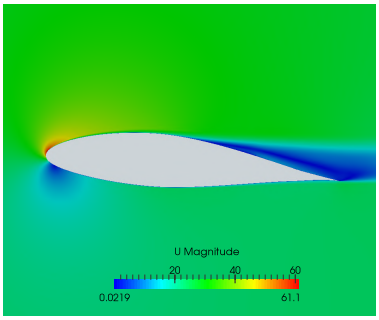

(f) Velocity field in the downstroke at $\alpha = 14°$.

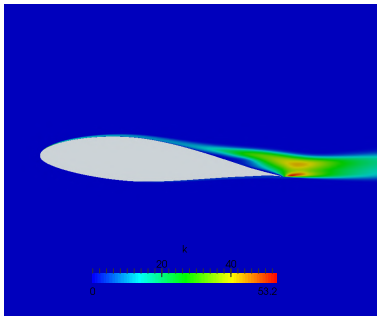

(g) Turbulent kinetic energy field in the upstroke at $\alpha = 14°$.

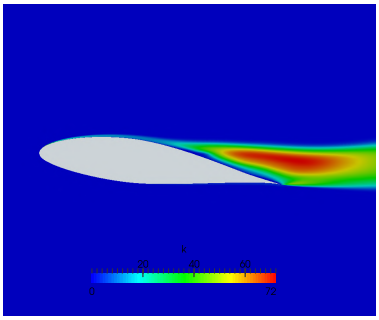

(h) Turbulent kinetic energy field at maximum $\alpha = 16°$.

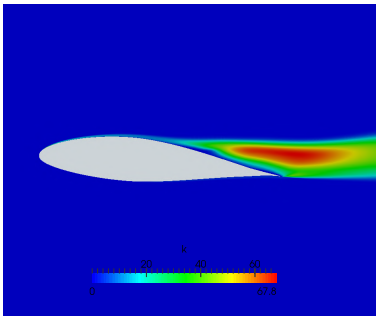

(i) Turbulent kinetic energy field in the downstroke at $\alpha = 14°$.

Figure 5.18: *Pressure, velocity and turbulent kinetic energy fields for NACA 64-418 case at* $\alpha_m = 8°$, $\alpha_A = 8°$ *and* $k = 0.0628$.

Chapter 6

Results – Morphing flap

The present chapter shows the results from the wind tunnel measurements of a harmonically oscillating trailing edge flap, conducted in the LTT in Section 6.1. Simulations of Q^{3}UIC and OpenFoam are discussed in Section 6.2. Finally, the main findings are summarised in Section 6.3. Additional unsteady measurements are performed for the free transition stall angle $\alpha = 10°$, and can be found in Appendix A.

6.1 Experimental results of the DU 95-W-180 airfoil

This section reports the steady and unsteady results of the oscillating flap measurements for a free and forced boundary layer transition.

6.1.1 Steady measurements

Figure 6.1 shows the lift and drag coefficients for the measured angle of attack range $-15° < \alpha < 18°$. The difference in lift coefficient between free and forced transition is clearly present, especially in the higher angle of attack region where there is predominantly separated flow. As expected, both $C_{l,max}$ and α_{max} are higher in the case of free transition. At first glance, the difference in lift coefficients between free and forced transition seems high, and it was believed there had been an error in the post-processing of the wind tunnel data.
However, the designer of the airfoil, Timmer, argued that this large difference may be possible provided that the runs are measured at Re = 1e6, which is on the edge of stability side, because the airfoil was designed for Re = 3e6 and is likely to show unstable behaviour for lower Re.
Additionally, the way in which the transition is forced, also has an effect that can not be neglected. The turbulator (zig-zag tape) that is used in the experiments is large and is likely to have created a thick boundary layer and severe transition, explaining the large difference that is found. Presumably a smaller turbulator would have shown more

resemblance with the free transition curve, since the increase in boundary layer thickness would have been smaller [31]. The drag coefficient in the tripped case is higher, confirming theoretical assumptions. The largest difference is found around $\alpha = 10°$, where also the lift curves show the largest deviation.

6.1.2 Unsteady measurements

The unsteady $C_l(\beta)$ loops of the measurements are shown in Figures 6.2 to 6.7. In all the left hand side figures transition is forced, whereas in the figures on the right hand side it is free. In all cases, the lift coefficient for the free transition is higher and steeper than in the forced case. This can be explained by comparing the steady polars in Figure 6.1a. With increase of the airfoil's angle of attack, the difference between the forced and free loops increases. Moreover, it is clearly visible that with increasing frequency k, the thickness of the loops grows, indicating that the unsteady effects are more pronounced.
Another observable difference is that the thickness of the loops is larger for free transition, especially for the two higher angles of attack of 8 and 18 degrees in Figures 6.4 to 6.7.

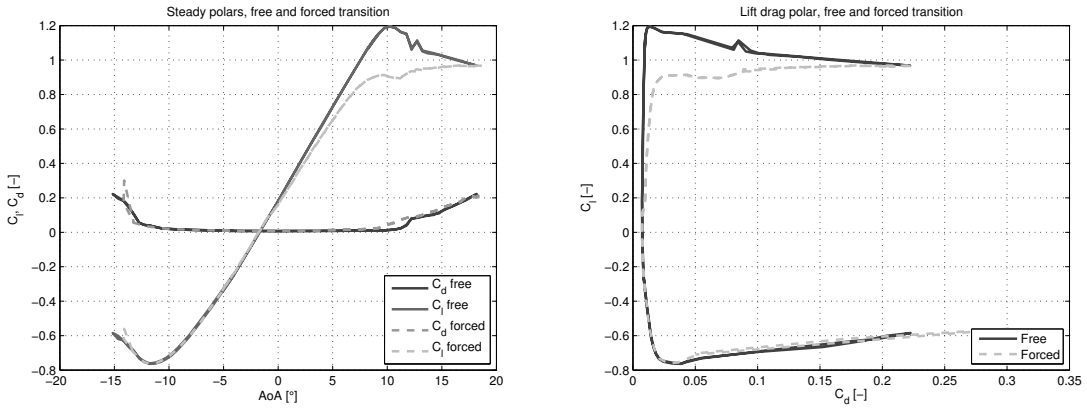

(a) $C_l(\alpha)$ and $C_d(\alpha)$.

(b) C_l-C_d polar.

Figure 6.1: *Lift and drag steady polars, forced and free transition.* $Re = 10^6$.

Angle of attack: $\alpha = 0°$

Figure 6.2 shows no remarkable difference between free and forced transition. What can be observed is that free transition has slightly wider loops and the lift values at positive flap angles of 5 degrees exceed tripped transition by 0.1 C_l. Increasing the reduced frequency from a nearly steady value of $k = 0.01$ to unsteady $k = 0.1$ shows a clear growth of the loops.
The same angle of attack and a higher flap amplitude of $\Delta\beta = 10°$ shows similar behaviour and the flow is still attached along the entire flap range of flap angles (Figure 6.3).

Angle of attack: $\alpha = 8°$

As the angle of attack is increased to 8 degrees, the slope and overall offset between the loops clearly changes resembling the behaviour of the steady curves from Figure 6.1. Also the unsteady effects are more pronounced for free transition as can be seen by the wider loops. Figure 6.4a does seem to show crossings of the lines, which would imply that the flow is alternating between an attached and separated condition. This is not the case for free transition, neither is it the case for increasing frequencies. It can also be the case that the upper left case lines do not cross but are almost on top of each other, implying the transition character does not change. Judging by the visual interpretation of the figure it is hard to say.
Increasing the flap amplitude leads to an overall shift upwards of the free loops compared to the forced loops, both the values for maximum negative deflection as maximum positive flap deflection are considerably higher. Where the positive flap angle C_l -difference is close to 0.2. Again it is not clearly visible if the flow changes from attached to separated for the lowest tripped reduced frequency in Figure 6.5a. However, the free case does seem to separate at $\beta = 6.5°$, in Figure 6.5b. For the free case an increase in frequency decreases the separated flow region as the reattachment point is advanced to $\beta = 9°$ in Figure 6.5d. The highest reduced frequency does not seem to have separated flow at all, for neither transition states. Apparently, for the $k = 0.01$ and $k = 0.05$ cases, the trailing edge separation is given enough time travel upstream the chord whereas the highest flap frequency of $k = 0.1$ does not seem to allow this as the flow stays attached in Figures 6.5e and 6.5f.

Angle of attack: $\alpha = 18°$

The highest measured angle of attack of 18 degrees clearly shows the chaotic behaviour of separated flow, Figure 6.6. The difference between free and forced transition is nearly absent, indicating the negligible effect of the turbulator at this high angle of attack.
The overall lift values in Figure 6.7 are slightly larger in the free transition case, but this difference is also almost negligible as in Figure 6.6.

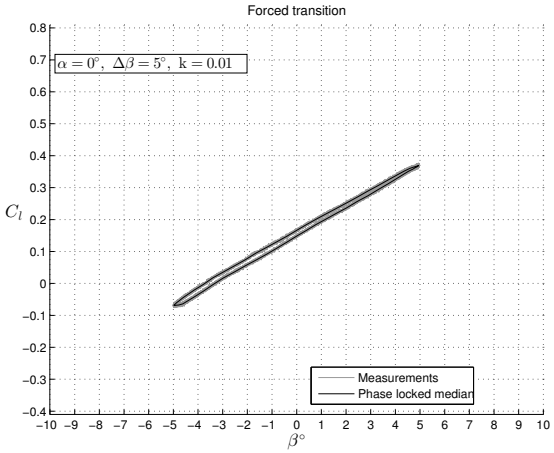

(a) Forced transition, $\alpha = 0°, \Delta\beta = 5°, k = 0.01$.

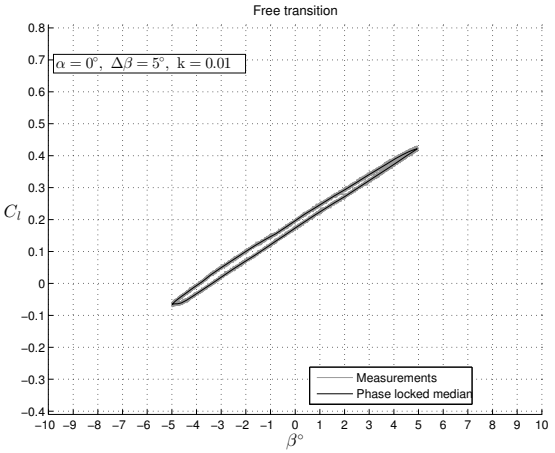

(b) Free transition, $\alpha = 0°, \Delta\beta = 5°, k = 0.01$.

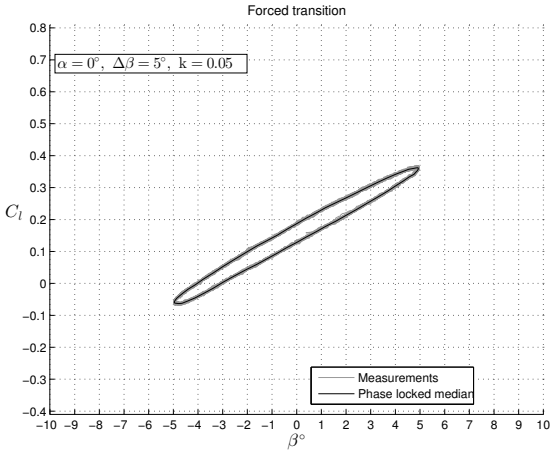

(c) Forced transition, $\alpha = 0°, \Delta\beta = 5°, k = 0.05$.

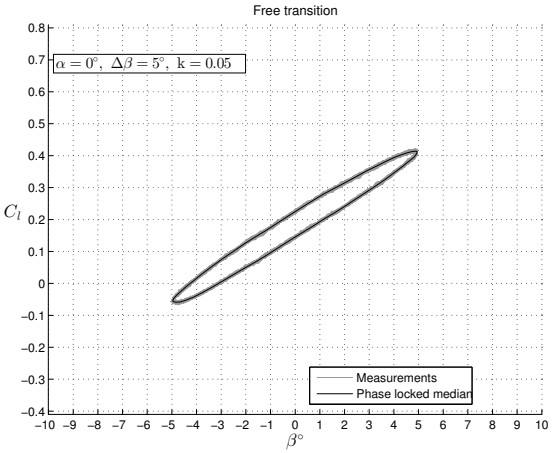

(d) Free transition, $\alpha = 0°, \Delta\beta = 5°, k = 0.05$.

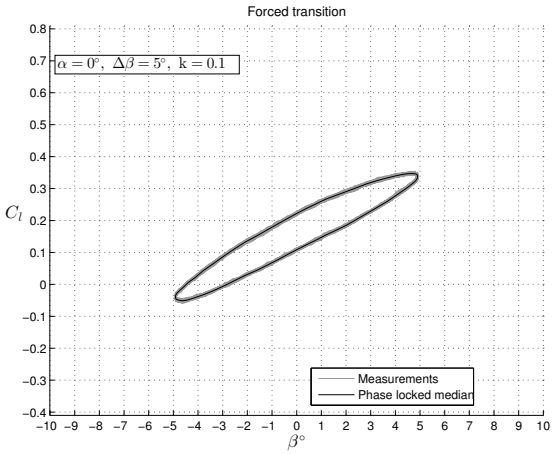

(e) Forced transition, $\alpha = 0°, \Delta\beta = 5°, k = 0.10$.

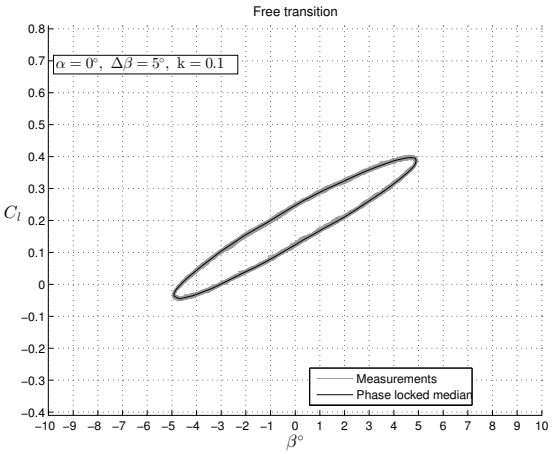

(f) Free transition, $\alpha = 0°, \Delta\beta = 5°, k = 0.10$.

Figure 6.2: *Experimental* $C_l(\beta)$ *for* $\alpha = 0°, \Delta\beta = 5°,\ k = 0.01, 0.05$ *and* 0.10.

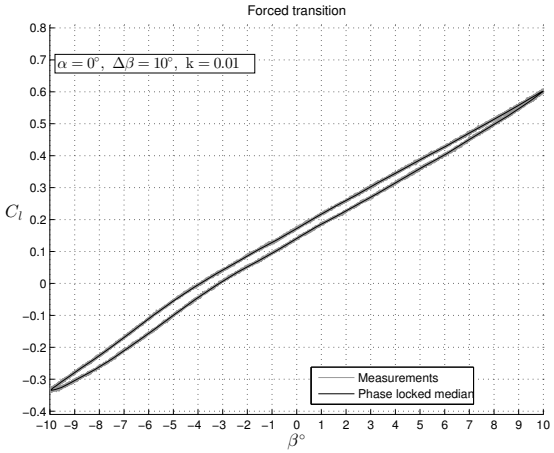

(a) Forced transition, $\alpha = 0°, \Delta\beta = 10°, k = 0.01$.

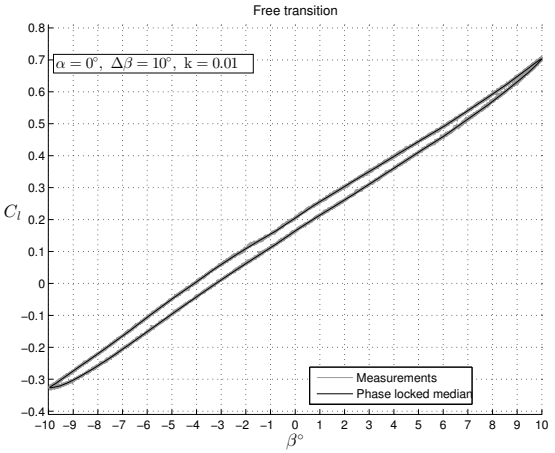

(b) Free transition, $\alpha = 0°, \Delta\beta = 10°, k = 0.01$.

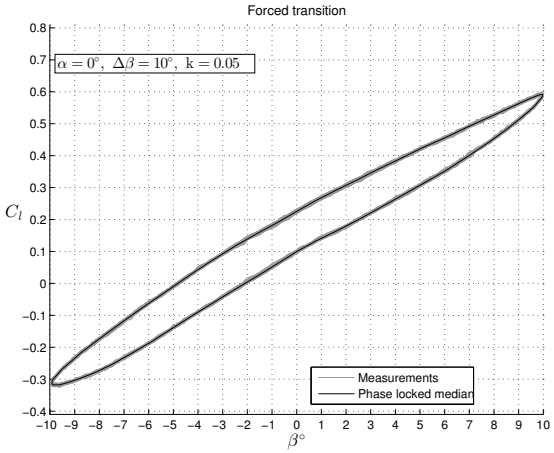

(c) Forced transition, $\alpha = 0°, \Delta\beta = 10°, k = 0.05$.

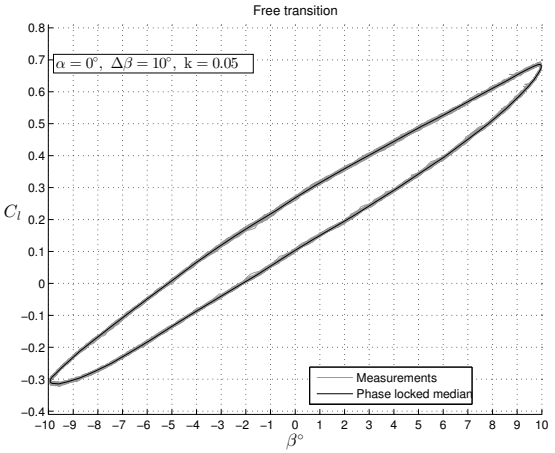

(d) Free transition, $\alpha = 0°, \Delta\beta = 10°, k = 0.05$.

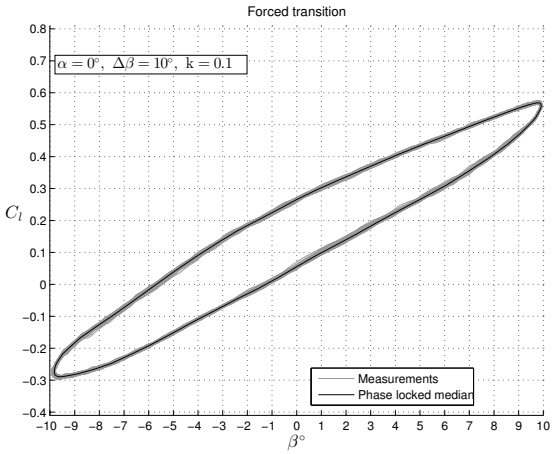

(e) Forced transition, $\alpha = 0°, \Delta\beta = 10°, k = 0.10$.

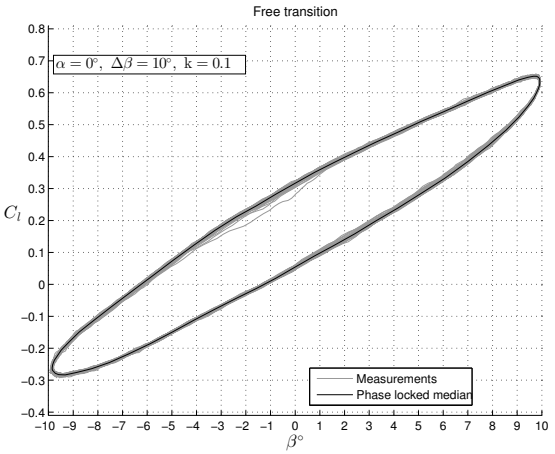

(f) Free transition, $\alpha = 0°, \Delta\beta = 10°, k = 0.10$.

Figure 6.3: *Experimental* $C_l(\beta)$ *for* $\alpha = 0°, \Delta\beta = 10°$, $k = 0.01, 0.05$ *and* 0.10.

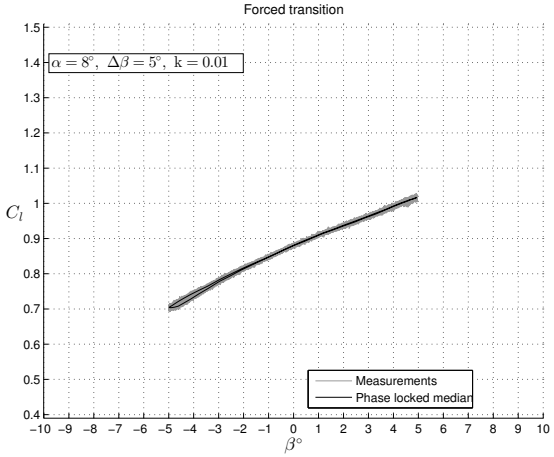

(a) Forced transition, $\alpha = 8°, \Delta\beta = 5°, k = 0.01$.

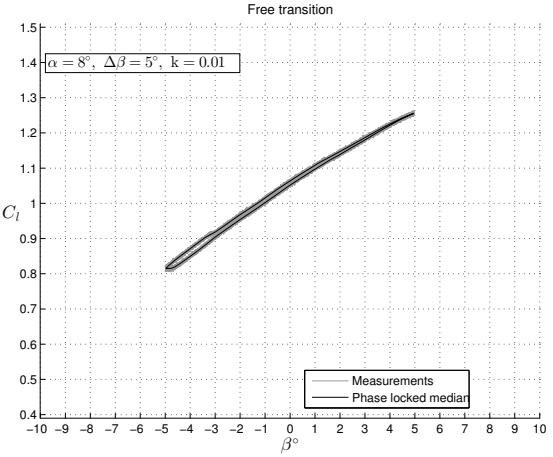

(b) Free transition, $\alpha = 8°, \Delta\beta = 5°, k = 0.01$.

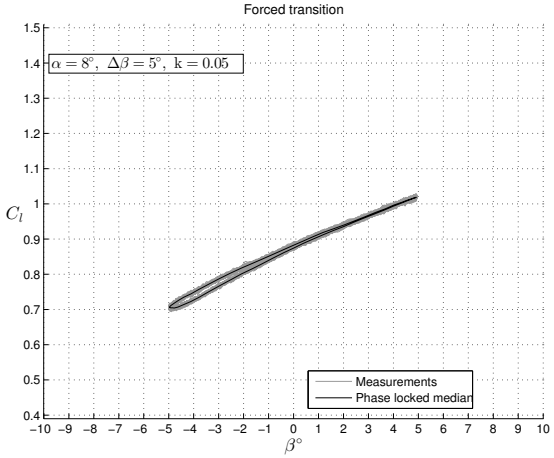

(c) Forced transition, $\alpha = 8°, \Delta\beta = 5°, k = 0.05$.

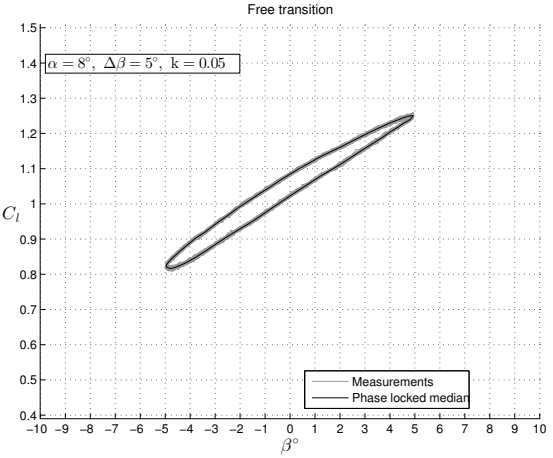

(d) Free transition, $\alpha = 8°, \Delta\beta = 5°, k = 0.05$.

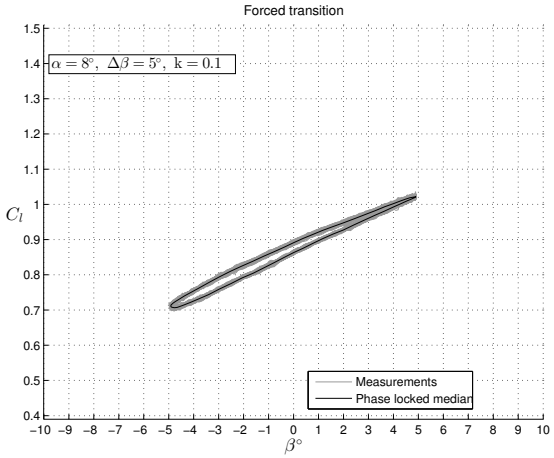

(e) Forced transition, $\alpha = 8°, \Delta\beta = 5°, k = 0.10$.

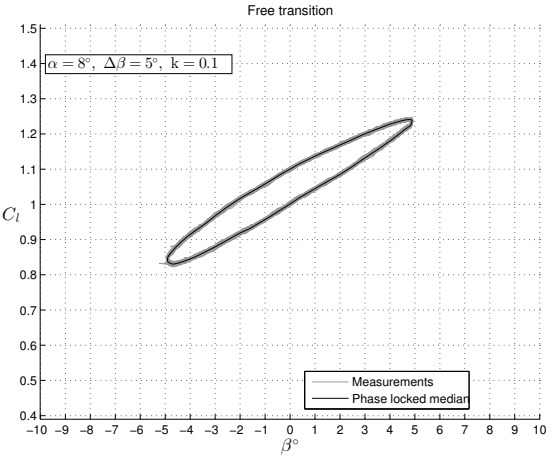

(f) Free transition, $\alpha = 8°, \Delta\beta = 5°, k = 0.10$.

Figure 6.4: *Experimental* $C_l(\beta)$ *for* $\alpha = 8°, \Delta\beta = 5°,\ k = 0.01, 0.05$ *and* 0.10.

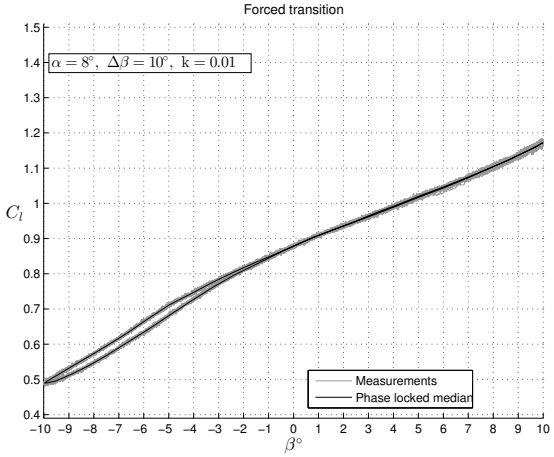

(a) Forced transition, $\alpha = 8°, \Delta\beta = 10°, k = 0.01$.

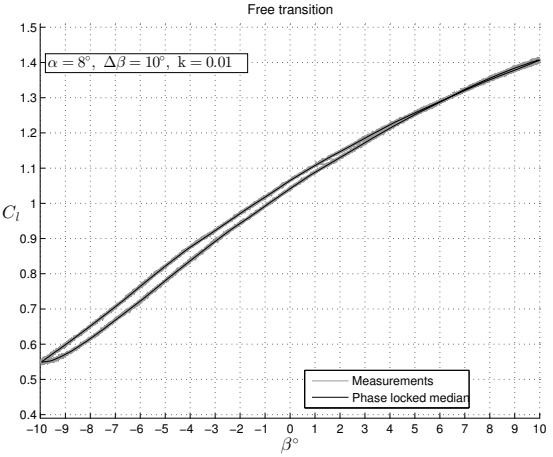

(b) Free transition, $\alpha = 8°, \Delta\beta = 10°, k = 0.01$.

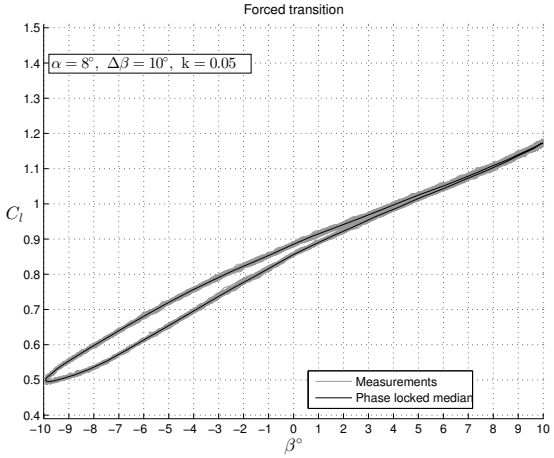

(c) Forced transition, $\alpha = 8°, \Delta\beta = 10°, k = 0.05$.

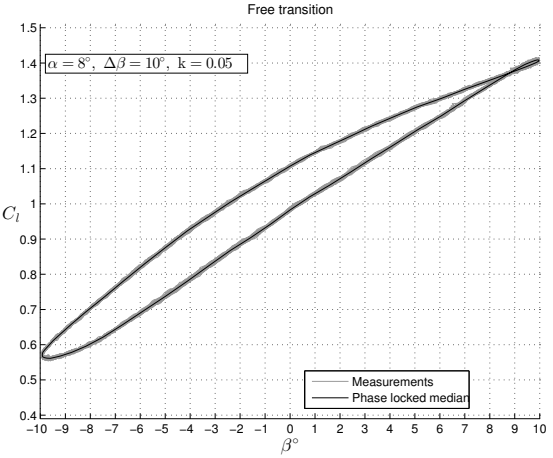

(d) Free transition, $\alpha = 8°, \Delta\beta = 10°, k = 0.05$.

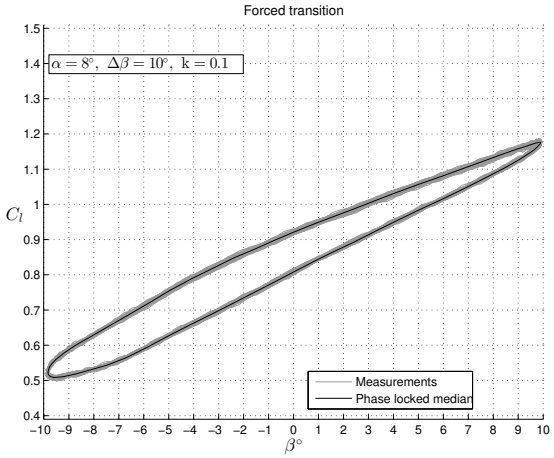

(e) Forced transition, $\alpha = 8°, \Delta\beta = 10°, k = 0.10$.

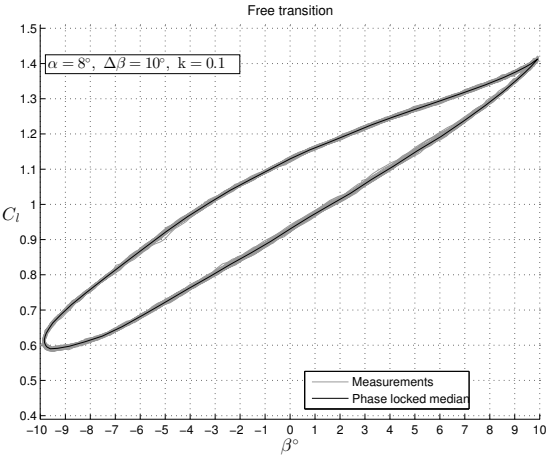

(f) Free transition, $\alpha = 8°, \Delta\beta = 10°, k = 0.10$.

Figure 6.5: *Experimental* $C_l(\beta)$ *for* $\alpha = 8°, \Delta\beta = 10°,\ k = 0.01, 0.05$ *and* 0.10.

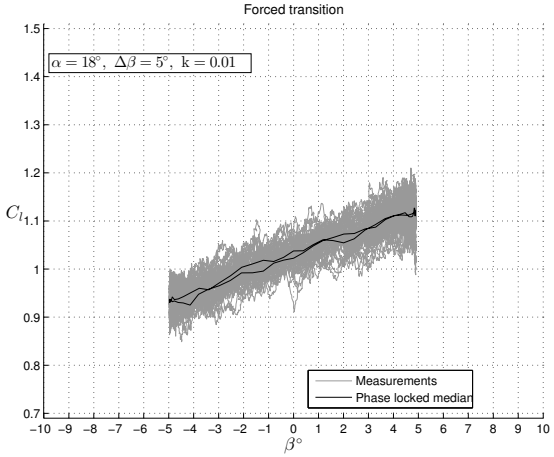

(a) Forced transition, $\alpha = 18°, \Delta\beta = 5°, k = 0.01$.

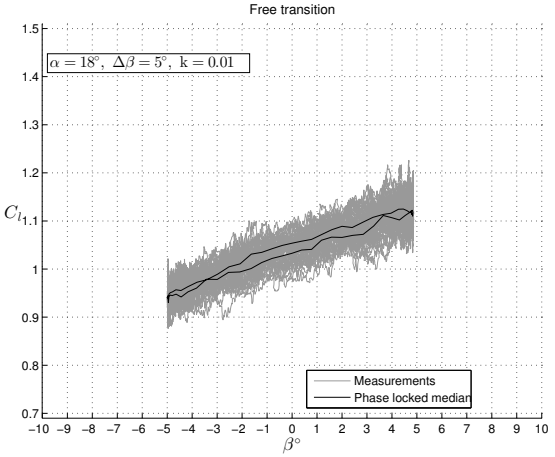

(b) Free transition, $\alpha = 18°, \Delta\beta = 5°, k = 0.01$.

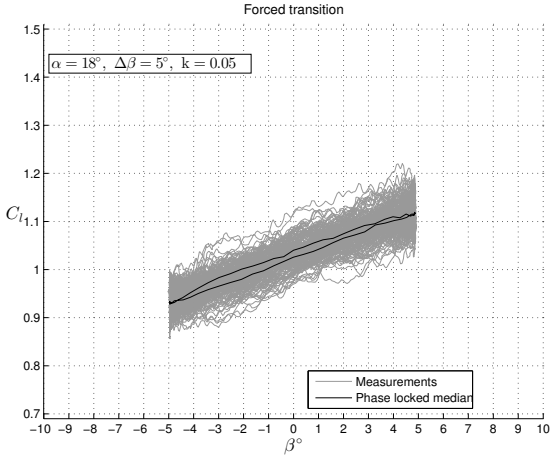

(c) Forced transition, $\alpha = 18°, \Delta\beta = 5°, k = 0.05$.

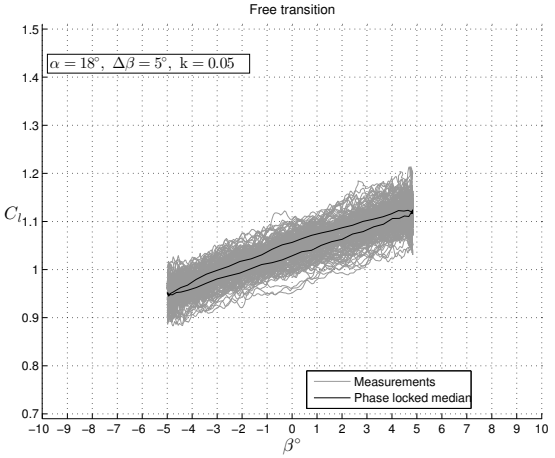

(d) Free transition, $\alpha = 18°, \Delta\beta = 5°, k = 0.05$.

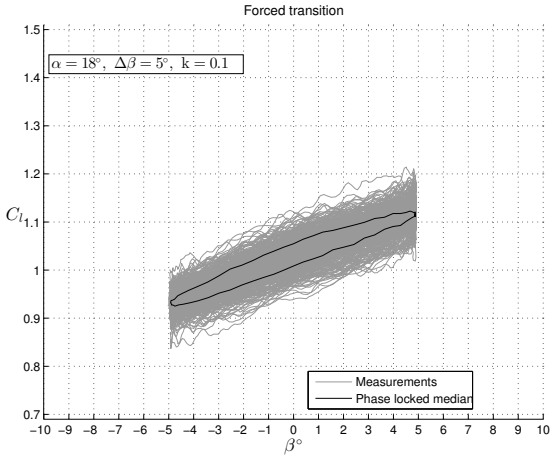

(e) Forced transition, $\alpha = 18°, \Delta\beta = 5°, k = 0.10$.

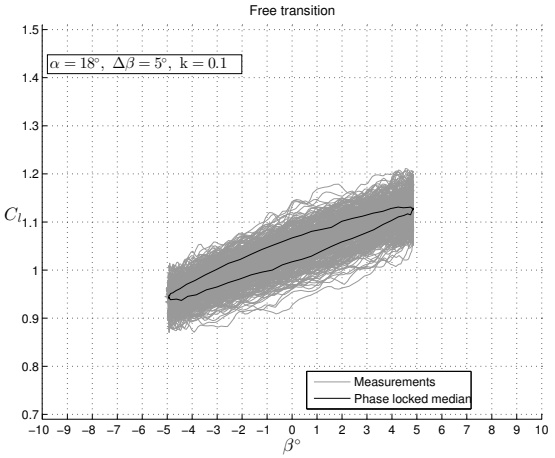

(f) Free transition, $\alpha = 18°, \Delta\beta = 5°, k = 0.10$.

Figure 6.6: *Experimental* $C_l(\beta)$ *for* $\alpha = 18°, \Delta\beta = 5°,\ k = 0.01, 0.05$ *and* 0.10.

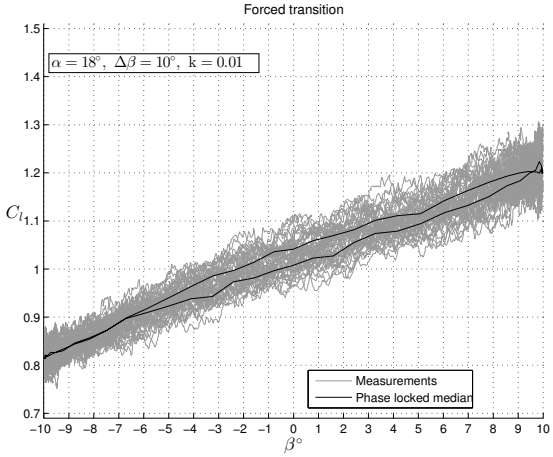

(a) Forced transition, $\alpha = 18°, \Delta\beta = 10°, k = 0.01$.

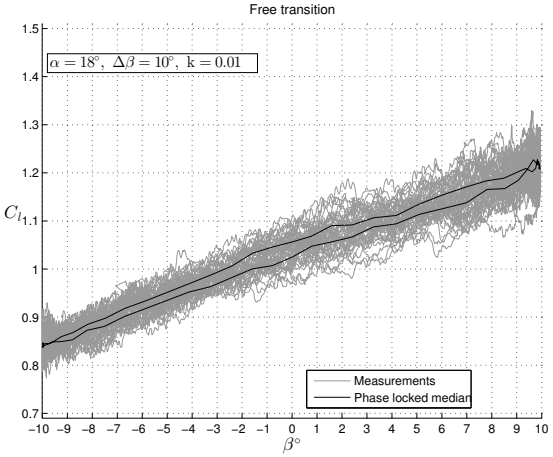

(b) Free transition, $\alpha = 18°, \Delta\beta = 10°, k = 0.01$.

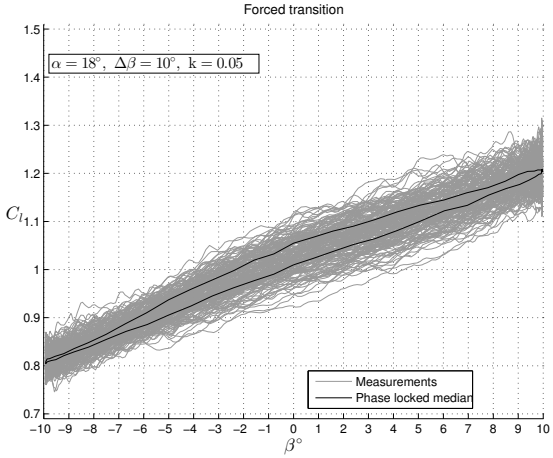

(c) Forced transition, $\alpha = 18°, \Delta\beta = 10°, k = 0.05$.

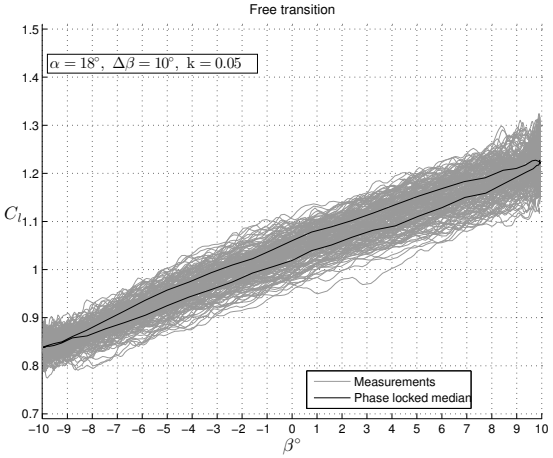

(d) Free transition, $\alpha = 18°, \Delta\beta = 10°, k = 0.05$.

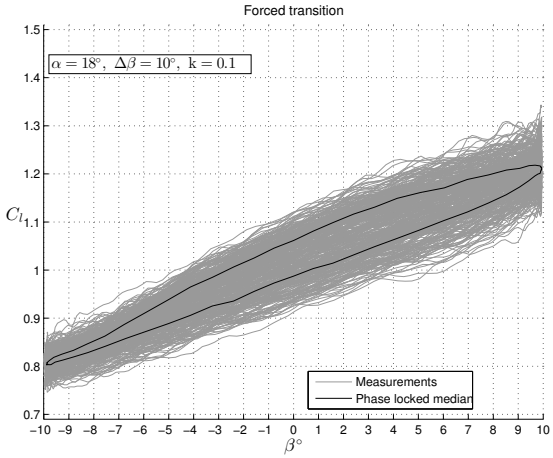

(e) Forced transition, $\alpha = 18°, \Delta\beta = 10°, k = 0.10$.

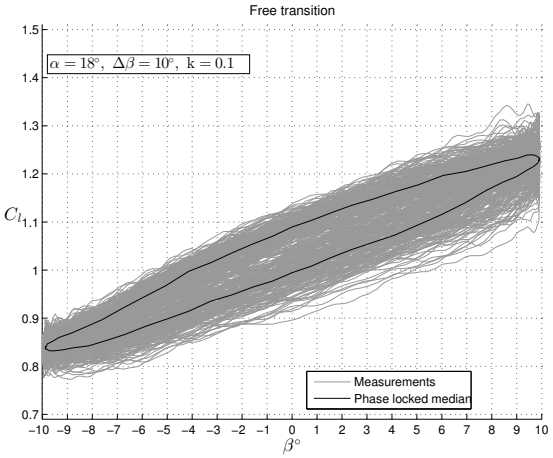

(f) Free transition, $\alpha = 18°, \Delta\beta = 10°, k = 0.10$.

Figure 6.7: *Experimental* $C_l(\beta)$ *for* $\alpha = 18°, \Delta\beta = 10°,\ k = 0.01, 0.05$ *and* 0.10.

6.2 Simulations

This section shows the convergence study, after which the steady and unsteady results are given and discussed.

6.2.1 Convergence study

A convergence study performed for different meshes and time steps is described next.

Mesh

The mesh characteristics are summarised in Table 6.1. For the mesh generation in Pointwise, a chord of 1 m is used instead of the 0.6 m of the experimental and OpenFOAM model. This means that – keeping Re constant – the initial cell size is larger than in OpenFOAM, because the x and y dimensions of the airfoil are scaled by 0.6 to comply with the measurements. Eventually the initial cell size used for the simulations is $1.4 \cdot 10^{-5}$ m or 0.014 mm, instead of the $2.3 \cdot 10^{-5}$ value in Pointwise found in Table 6.1.

Table 6.1: *Mesh variables DU 95-W-180 used for convergence study in Pointwise.*

	Number of cells N	**N=48522**	**N=13446**	**N=5248**
General	Surface points	2×128	2×64	2×32
	TE & LE spacing	0.001	0.002	0.004
	Initial cell size	2.3×10^{-5} m	2.3×10^{-5} m	2.3×10^{-5} m
	Growth rate	1.1	1.2	1.3
	Farfield radius	92c	92c	89c
BL domain	Cells	15240	3780	1240
	Steps	60	30	20
	Growth rate	1.1	1.2	1.3
TE domain	Cells	1800	360	120
	Steps	15	6	3
	Growth rate	1.13	1.2	1.3
Farfield domain	Cells	31512	9306	3888
	Initial cell size	0.006	0.0045	0.003
	Steps	78	47	36

Time step

For the lower angles of attack of 8 and 10 degrees, a fixed time step of 1×10^{-4} s was enough. The deviations between the largest time step 1×10^{-4} s and the smallest 2.5×10^{-5} s was negligible. So in order to reduce computational time, the largest time step is chosen for the 0 and 8 degree angles of attack. To try capturing the chaotic effects at 18 degrees, a smaller, intermediate time step of 5×10^{-5} s is used. An overview of the time steps for the angles is shown in Table 6.2.

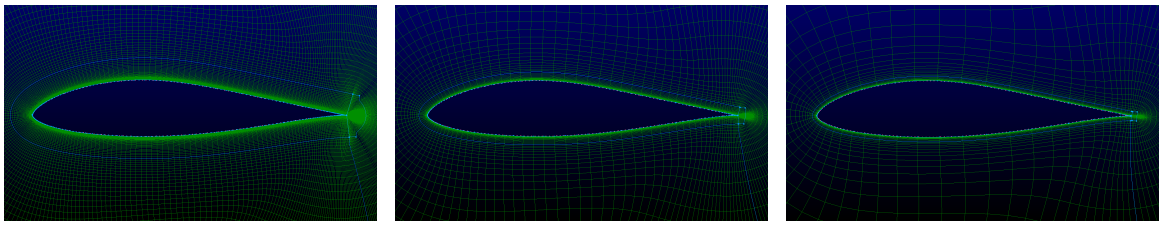

(a) Mesh with $N = 48522$ cells. (b) Mesh with $N = 13446$ cells. (c) Mesh with $N = 5248$ cells.

Figure 6.8: *Sparsity of meshes used for the convergence study.*

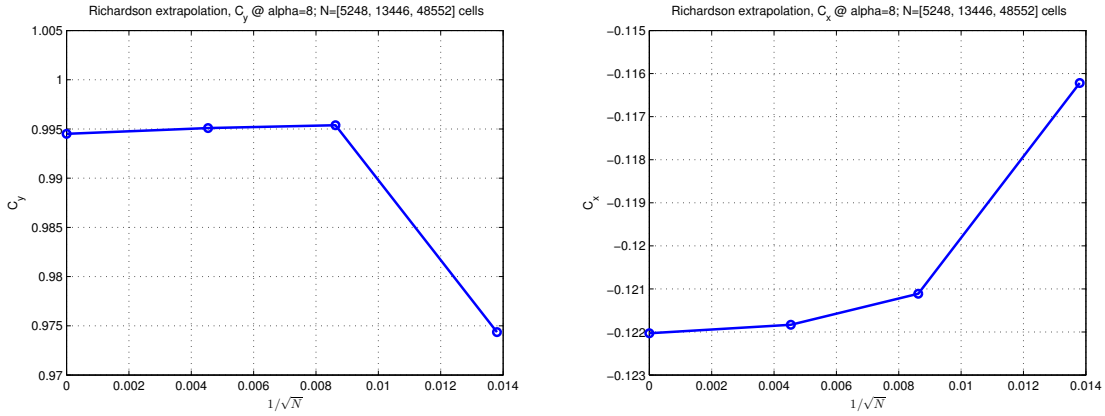

(a) C_y component. (b) C_x component.

Figure 6.9: *Values of steady C_y and C_x components for meshes with $N = [5248;\ 13446;\ 48522;\ \infty] \sim 1/\sqrt{N} = [0.0138,\ 0.0086,\ 0.0045,\ 0]$.*

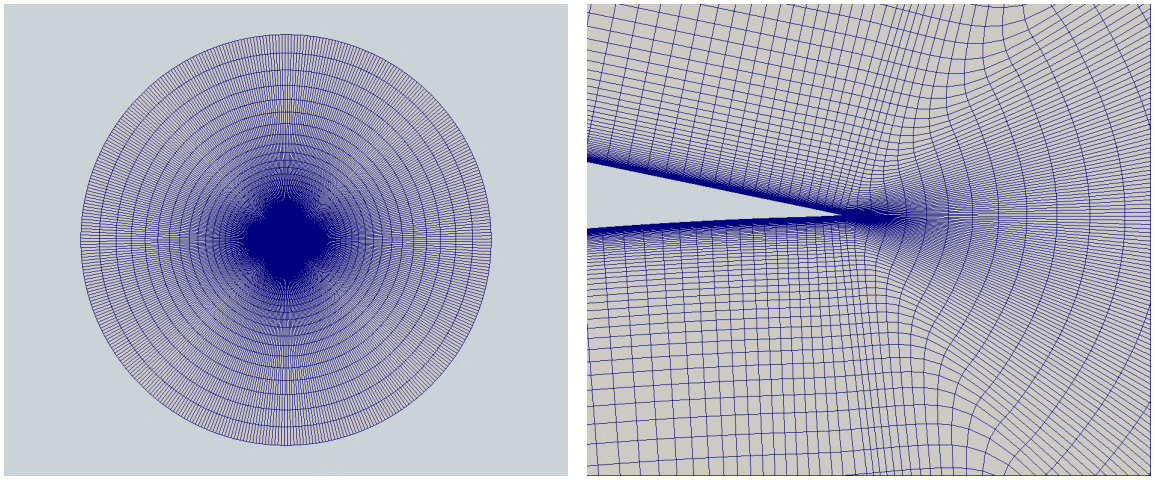

(a) Enitre mesh of approximately 90 chords radius. (b) Detail of trailing edge region.

Figure 6.10: *Entire mesh of 48522 cells and a more detailed view of trailing edge region.*

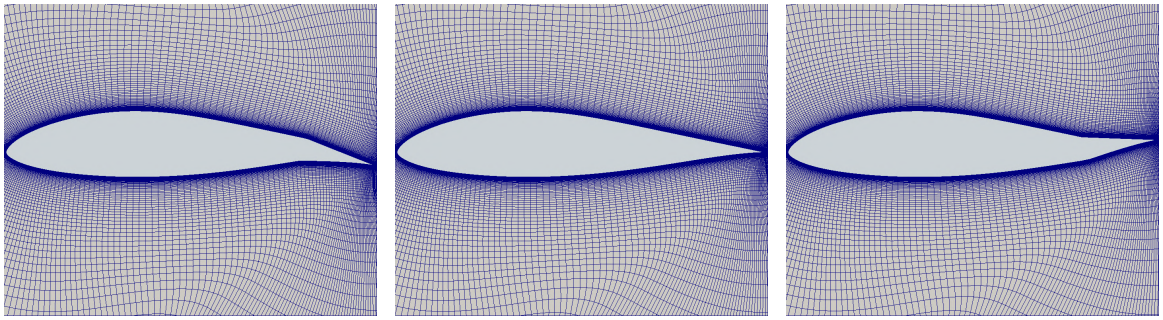

(a) Positive flap angle $\beta = 10°$. (b) Zero flap angle $\beta = 0°$. (c) Negative flap angle $\beta = -10°$.

Figure 6.11: *Flap angles and corresponding mesh deformation in OpenFOAM.*

Table 6.2: *Time steps used for DU 95-W-180 simulations.*

$\alpha[°]$	`deltaT` [s]
0	1e–4
8	1e–4
18	5e–5

6.2.2 Steady results

The steady lift polars of the experiments and the two numerical models are shown in Figure 6.12. Q^{3}UIC captures the forced transition to an acceptable accuracy. There is a small over prediction for $-5 < \alpha < 7$, after which the curves intersect and Q^{3}UIC starts oscillating and under predicting C_l. Both α_{max} and $C_{l,max}$ are lower in Q^{3}UIC. The spurious oscillations of the lift curve at high angles are related to small variations in the separation location that affect the suction side pressure level, abruptly changing the aerodynamic loading on the airfoil. This can be reduced with a finer airfoil discretisation. However, the current version of Q^{3}UIC does not allow this.

OpenFOAM shows a considerably larger deviation from the experimental curve. It does not seem to accurately capture the stall angle, nor $C_{l,max}$. This is can be caused by improper handling of the turbulent inflow parameters discussed in Section 4.2.5. Analysis has shown that the reference far-field values that are set at approximately 80 chords in front of the airfoil leading edge, diminish by the time they reach the airfoil. A k-ω SST-Sust model, is better in sustaining the far-field values and is likely to show other results. This model has not been used in this study, but can be recommended for future studies.

For the free transition case Q^{3}UIC shows a constant over prediction, also for the higher angles of attack. After stall, around 12 degrees, the curves coincide. Q^{3}UIC seems to capture α_{max} well at 10 degrees, but $C_{l,max}$ is slightly over predicted: 1.28 vs 1.2.

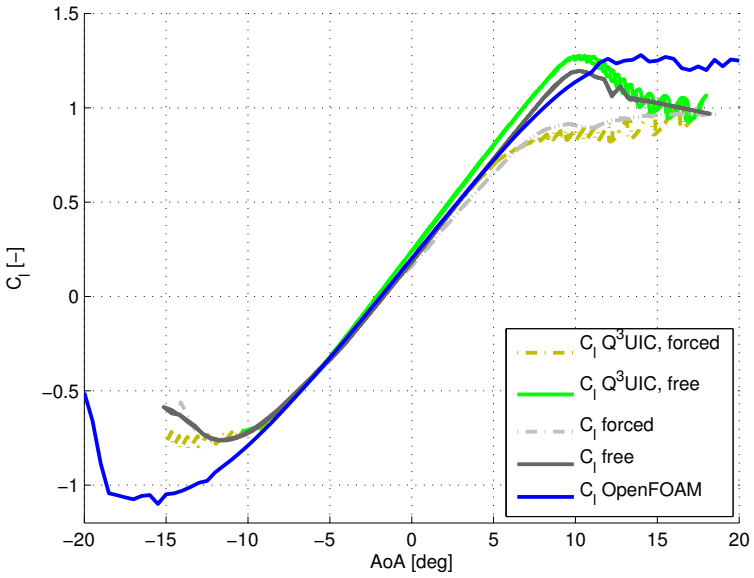

Figure 6.12: *Steady lift polars free and forced transition combined. Numerical and experimental.*

6.2.3 Unsteady results

The lift loops at the three angles of attack are described next. As the unsteady Kutta condition is supposed to have an influence on the results due to the flap movement, the different versions provided in Q^{3}UIC have been compared to each other without showing remarkable deviations. All simulations are done with the third Kutta condition in (4.6), because it is believed to be the most accurate, incorporating the wake vorticity.

Angle of attack: $\alpha = 0°$

Figure 6.13 shows great resemblance between the two numerical methods, this is to be expected as the steady polars coincide at $\alpha = 0°$ in Figure 6.12. Both show a vertical offset compared to measurements which also follows from the steady polars. Apart from this shift, the loop size is captured very well by both Q^{3}UIC and OpenFOAM. Free transition also shows a vertical offset and a small difference in slope.

The similarities between experiments and simulations for a higher flap amplitude of 10 degrees, in Figure 6.14 are still large. Towards the maximum positive flap deflections, discrepancies start to become more apparent.

Angle of attack: $\alpha = 8°$

For the angle of attack of 8 degrees in Figure 6.15, Q^{3}UIC starts to run into problems for the forced transition cases. For a free transition this spurious behaviour is not observed. OpenFOAM over predicts the size of the loops for all frequencies. Free transition is

captured much more accurately because perhaps the location of the transition in Q^{3}UIC in the forced case does not coincide with the measurements and around this critical angle of attack this has a large influence on the outcome.

The flow in Q^{3}UIC seems to show trailing edge separation around an angle of attack of 8 degrees, that can be seen in the steady polar curve as well as in the unsteady Figure 6.16. The steady experiments undergo trailing edge separation slightly later compared to Q^{3}UIC. The dynamic effects appear to delay separation for the experiments but not for Q^{3}UIC where separation is clearly observed. In Figure 6.16a, OpenFOAM also predicts a small separated flow region from $\beta \approx 4°$. The two higher frequency loops are similar, apart from the vertical offset.

The free cases show larger attached regions, but still the prediction of a small separated flow region is present at the higher flap angles. Figure 6.16

Angle of attack: $\alpha = 18°$

The Q^{3}UIC loops coincide acceptably with the measurements in Figure 6.17, both for free and forced transition. Again the difference at this high angle of attack is nearly unobservable. Negative flap angles seem to help reattach the boundary layer as the lift values are similar or even higher than for positive flap angles. OpenFOAM clearly shows faulty results. First of all, the steady state values at such a high angle of attack were not steady. This meant an unsteady solver without body motion was used to obtain the initial conditions to initialise the unsteady solver which does include the flap motion. Clearly an error has occurred somewhere in the initialisation process, probably while reconstructing data after having decomposed for doing computations on the TU Delft cluster. So the validity of the OpenFOAM loops can be regarded as questionable.

The effect for Q^{3}UIC described above is accentuated for a higher flap angle in Figure 6.18. Remarkable is that the higher flap angles show relatively accurate results, while Q^{3}UIC shows a large increase in lift for negative flap angles. This means that the negative, upward movement of the flap seems to have a favourable effect on the boundary layer and helps reattaching it.

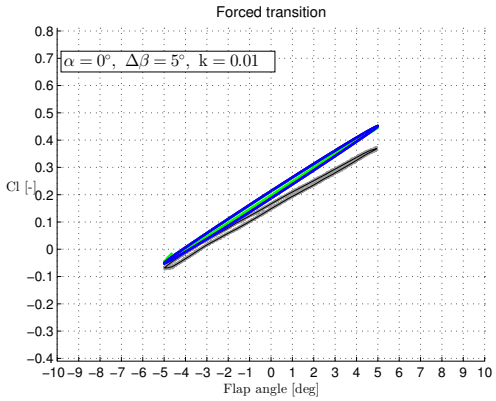

(a) Forced transition, $\alpha = 0°, \Delta\beta = 5°, k = 0.01$.

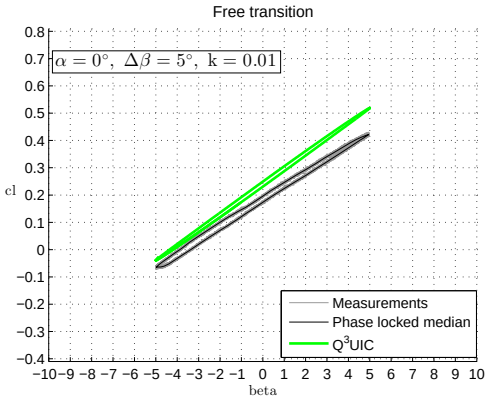

(b) Free transition, $\alpha = 0°, \Delta\beta = 5°, k = 0.01$.

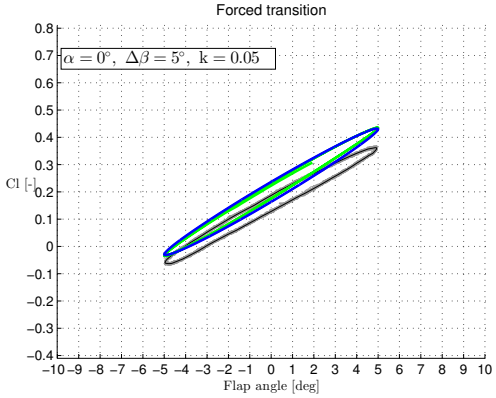

(c) Forced transition, $\alpha = 0°, \Delta\beta = 5°, k = 0.05$.

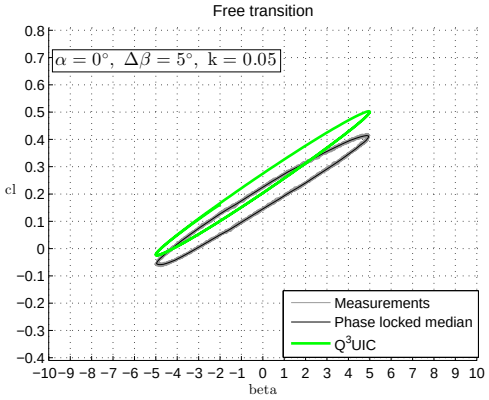

(d) Free transition, $\alpha = 0°, \Delta\beta = 5°, k = 0.05$.

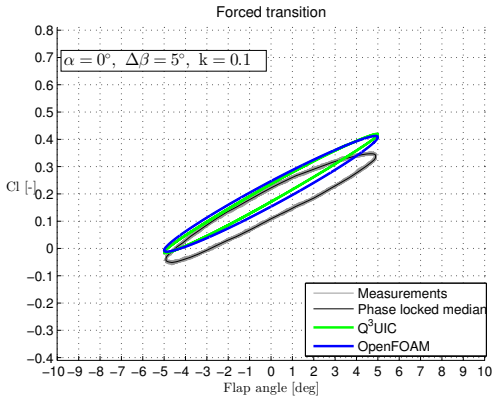

(e) Forced transition, $\alpha = 0°, \Delta\beta = 5°, k = 0.10$.

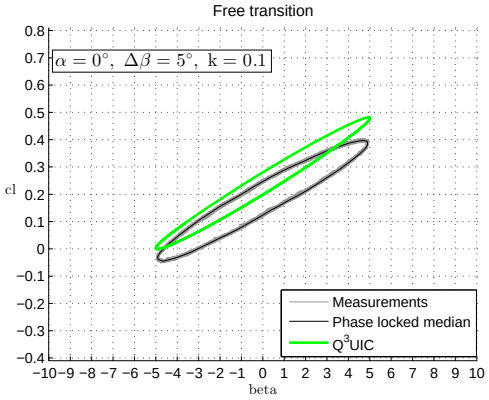

(f) Free transition, $\alpha = 0°, \Delta\beta = 5°, k = 0.10$.

Figure 6.13: *Experimental and numerical* $C_l(\beta)$ *for* $\alpha = 0°, \Delta\beta = 5°$, $k = 0.01, 0.05$ *and* 0.10.

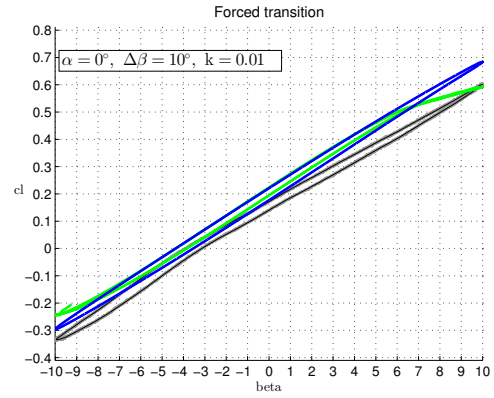

(a) Forced transition, $\alpha = 0°, \Delta\beta = 10°, k = 0.01$.

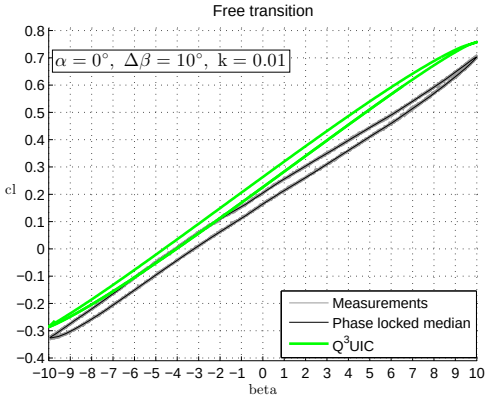

(b) Free transition, $\alpha = 0°, \Delta\beta = 10°, k = 0.01$.

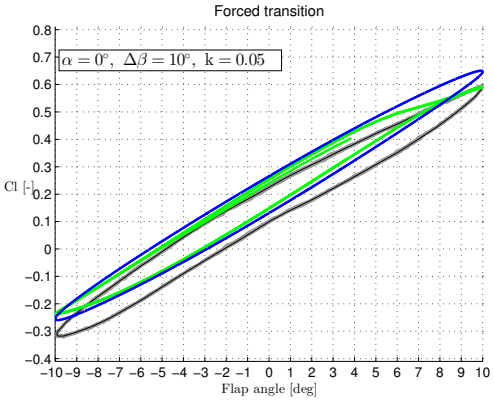

(c) Forced transition, $\alpha = 0°, \Delta\beta = 10°, k = 0.05$.

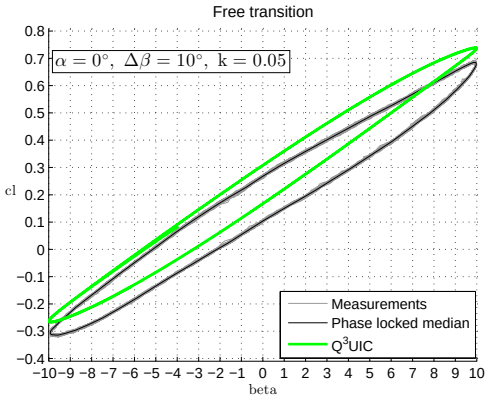

(d) Free transition, $\alpha = 0°, \Delta\beta = 10°, k = 0.05$.

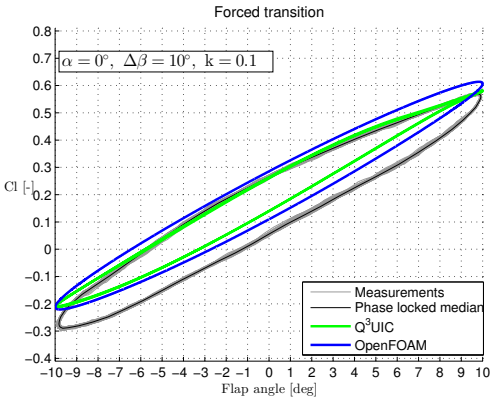

(e) Forced transition, $\alpha = 0°, \Delta\beta = 10°, k = 0.10$.

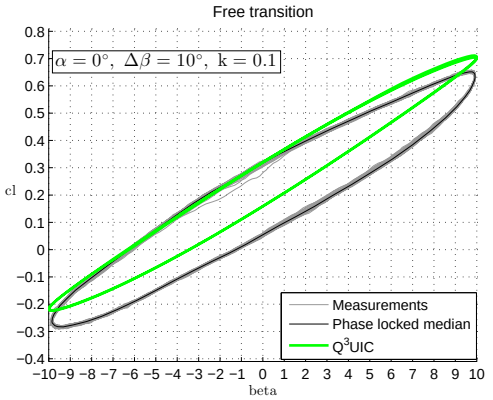

(f) Free transition, $\alpha = 0°, \Delta\beta = 10°, k = 0.10$.

Figure 6.14: *Experimental and numerical* $C_l(\beta)$ *for* $\alpha = 0°, \Delta\beta = 10°$, $k = 0.01, 0.05$ *and* 0.10.

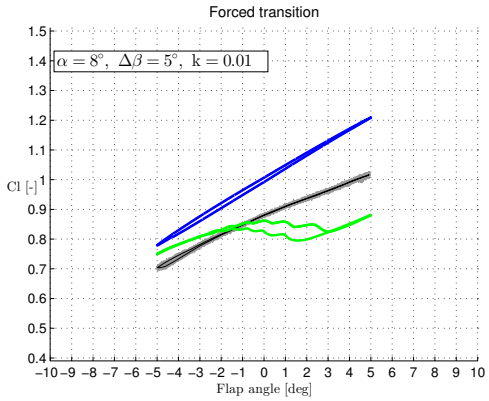

(a) Forced transition, $\alpha = 8°, \Delta\beta = 5°, k = 0.01$.

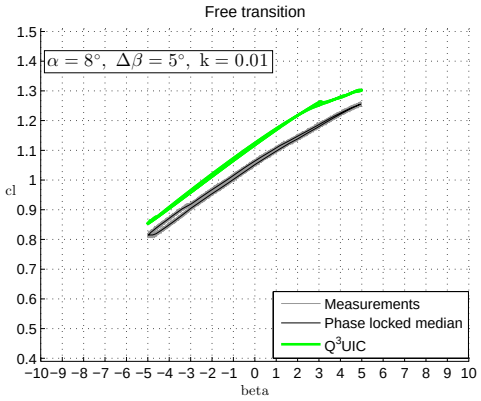

(b) Free transition, $\alpha = 8°, \Delta\beta = 5°, k = 0.01$.

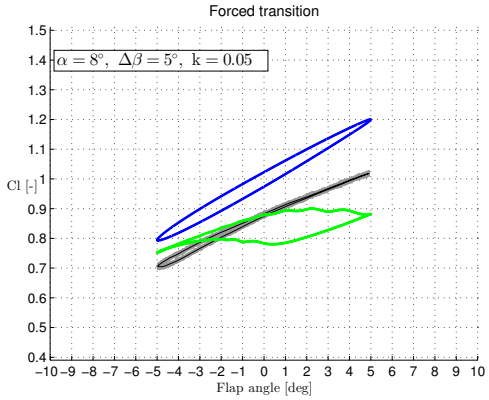

(c) Forced transition, $\alpha = 8°, \Delta\beta = 5°, k = 0.05$.

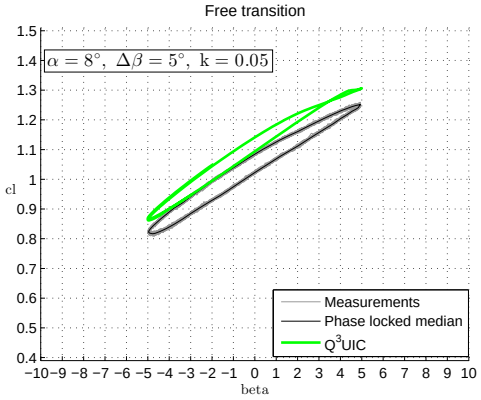

(d) Free transition, $\alpha = 8°, \Delta\beta = 5°, k = 0.05$.

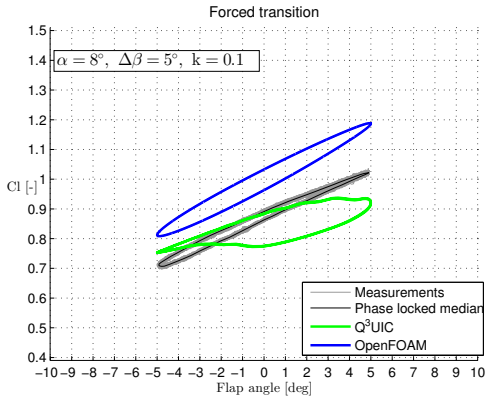

(e) Forced transition, $\alpha = 8°, \Delta\beta = 5°, k = 0.10$.

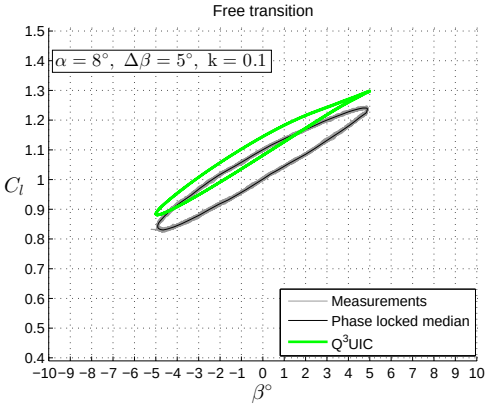

(f) Free transition, $\alpha = 8°, \Delta\beta = 5°, k = 0.10$.

Figure 6.15: *Experimental and numerical* $C_l(\beta)$ *for* $\alpha = 8°, \Delta\beta = 5°$, $k = 0.01, 0.05$ *and* 0.10.

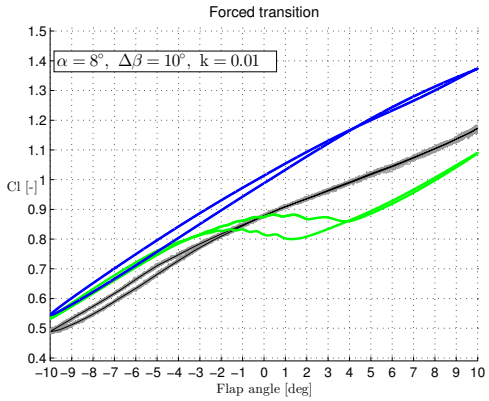

(a) Forced transition, $\alpha = 8°, \Delta\beta = 10°, k = 0.01$.

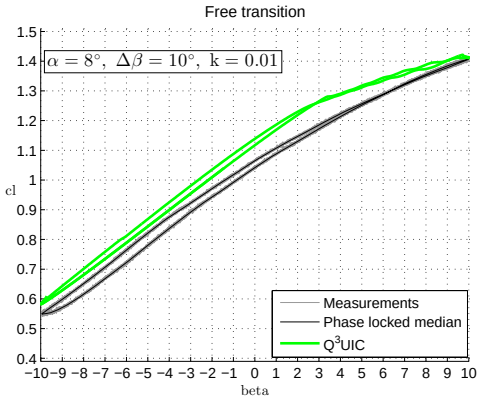

(b) Free transition, $\alpha = 8°, \Delta\beta = 10°, k = 0.01$.

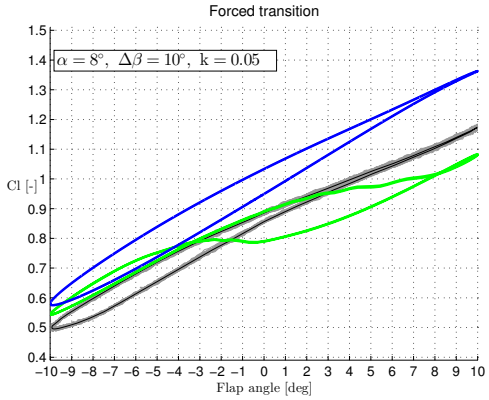

(c) Forced transition, $\alpha = 8°, \Delta\beta = 10°, k = 0.05$.

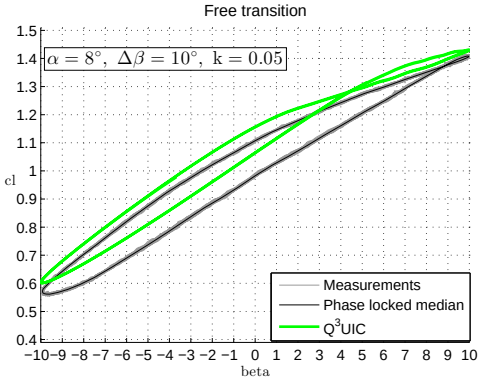

(d) Free transition, $\alpha = 8°, \Delta\beta = 10°, k = 0.05$.

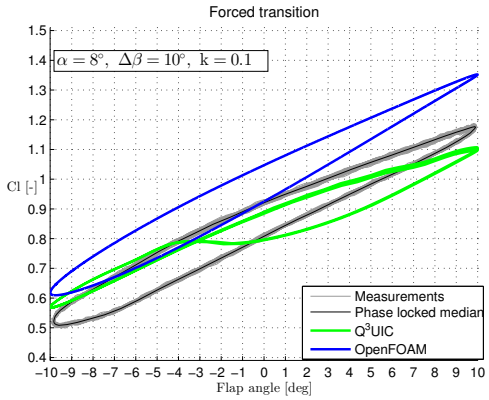

(e) Forced transition, $\alpha = 8°, \Delta\beta = 10°, k = 0.10$.

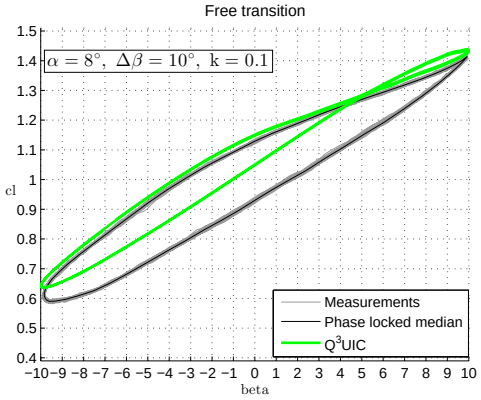

(f) Free transition, $\alpha = 8°, \Delta\beta = 10°, k = 0.10$.

Figure 6.16: *Experimental and numerical* $C_l(\beta)$ *for* $\alpha = 8°, \Delta\beta = 10°$, $k = 0.01, 0.05$ *and* 0.10.

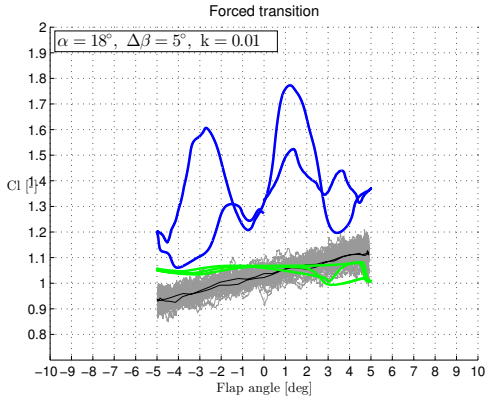

(a) Forced transition, $\alpha = 18°, \Delta\beta = 5°, k = 0.01$.

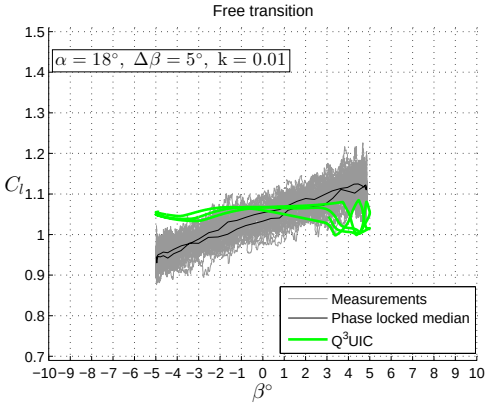

(b) Free transition, $\alpha = 18°, \Delta\beta = 5°, k = 0.01$.

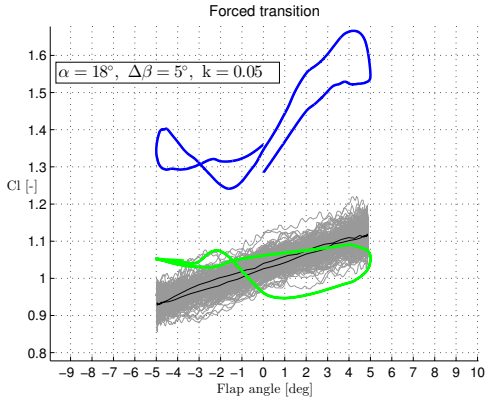

(c) Forced transition, $\alpha = 18°, \Delta\beta = 5°, k = 0.05$.

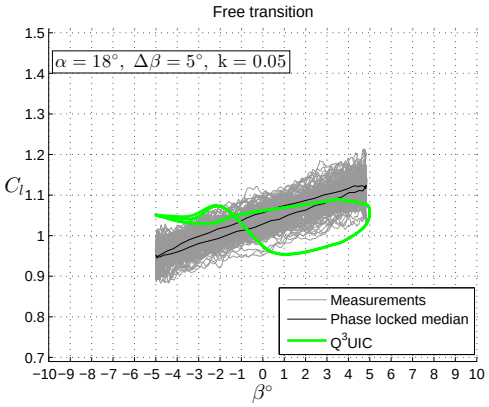

(d) Free transition, $\alpha = 18°, \Delta\beta = 5°, k = 0.05$.

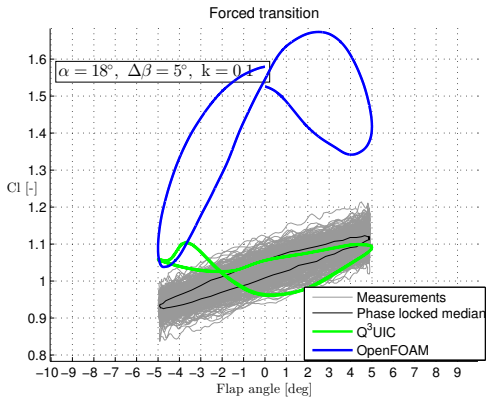

(e) Forced transition, $\alpha = 18°, \Delta\beta = 5°, k = 0.10$.

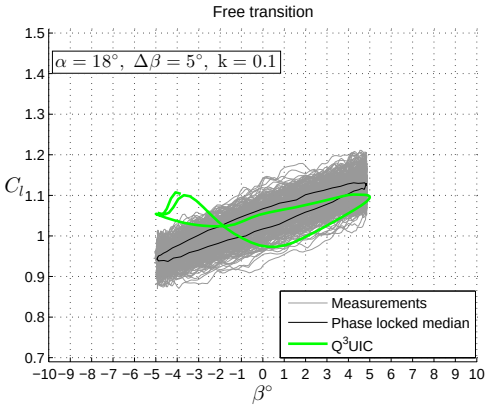

(f) Free transition, $\alpha = 18°, \Delta\beta = 5°, k = 0.10$.

Figure 6.17: *Experimental and numerical* $C_l(\beta)$ *for* $\alpha = 18°, \Delta\beta = 5°$, $k = 0.01, 0.05$ *and* 0.10.

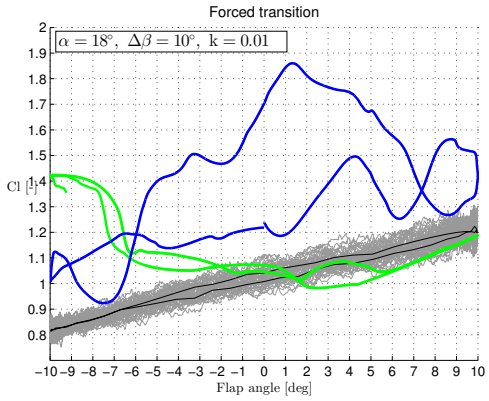

(a) Forced transition, $\alpha = 18°, \Delta\beta = 10°, k = 0.01$.

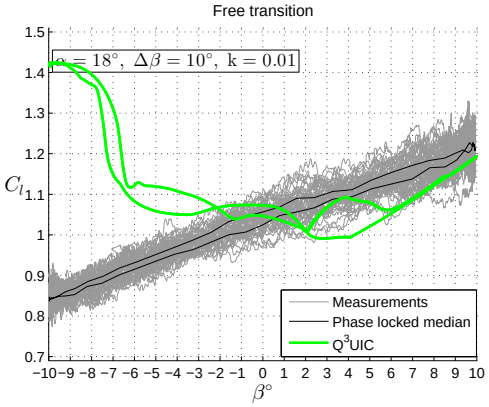

(b) Free transition, $\alpha = 18°, \Delta\beta = 10°, k = 0.01$.

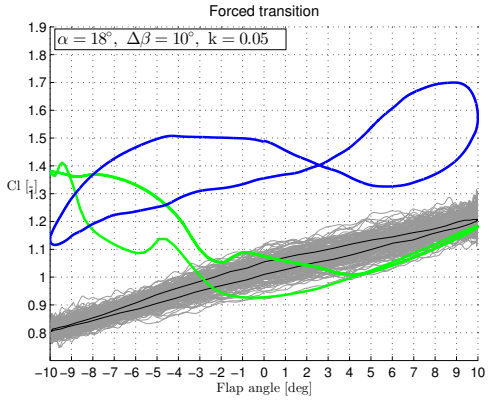

(c) Forced transition, $\alpha = 18°, \Delta\beta = 10°, k = 0.05$.

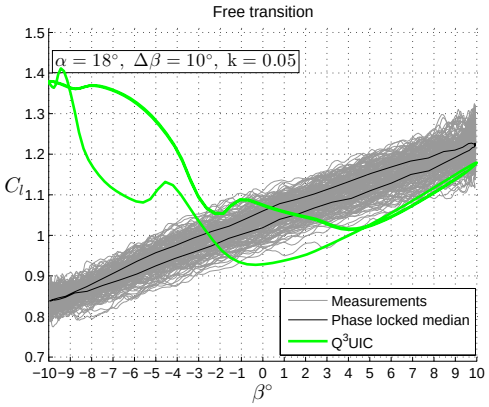

(d) Free transition, $\alpha = 18°, \Delta\beta = 10°, k = 0.05$.

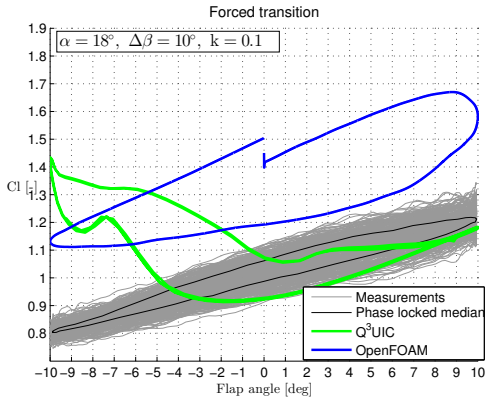

(e) Forced transition, $\alpha = 18°, \Delta\beta = 10°, k = 0.10$.

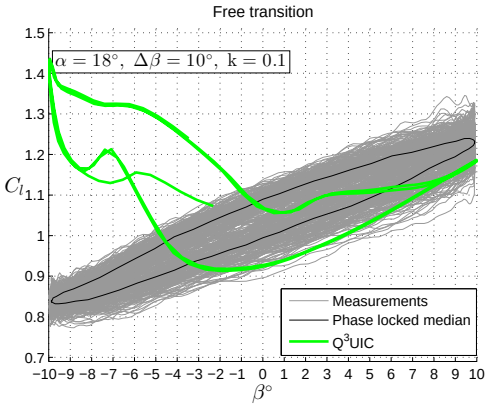

(f) Free transition, $\alpha = 18°, \Delta\beta = 10°, k = 0.10$.

Figure 6.18: *Experimental and numerical* $C_l(\beta)$ *for* $\alpha = 18°, \Delta\beta = 10°$, $k = 0.01, 0.05$ *and* 0.10.

6.3 Conclusive remarks

The unsteady performance of OpenFOAM – i.e. without bringing into consideration the steady state offset from Figure 6.12 – is accurate for 0 and 8 degrees angles of attack. For the highest angle of attack of 18 degrees, a combination of wrong initial conditions and possibly a too coarse mesh in combination with a too large time step, has resulted in the spurious behaviour of the $C_l(\beta)$ loops. The use of k-ω SST Sust or lowRe models might be capable of improving results, especially for the highest angle of attack case of 18 degrees. What also can be done is to construct a finer mesh and run the simulations with a smaller time step.

Q^3UIC already starts to experience problems at 8 degrees, but only so for the forced transition case. This could mean that a forced boundary layer trip in Q^3UIC for this particular angle, is critical. And that a free development of the boundary layer is modelled more accurately. Additionally a finer airfoil discretisation can surely lead to more accurate results. Moreover, an alteration of the unsteady Kutta condition can improve the set of closure relations, enhance the viscous-inviscid coupling and solve viscous effects more accurately.

Chapter 7

Conclusions and recommendations

7.1 Conclusions

The main objective of this thesis was to gather experimental data in unsteady flow conditions and to validate two numerical models by means of comparison with the experimentally obtained wind tunnel pressure measurements. The accuracy of these models is addressed as well as the difference in terms of their strong and weak points.

Q^{3}UIC

The viscous-inviscid interaction code Q^{3}UIC has shown to provide fairly accurate results for the pitching airfoil case. The flap measurements were less well covered.

- To validate Q^{3}UIC, wind tunnel experiments are conducted for free and tripped boundary layer transitions in the open return wind tunnel of DTU as discussed in Chapter 5. During post processing of the experimental data, some errors were found. For instance, a stagnation pressure of $C_p = 1.2$ due to a misalignment of the Pitot tube; an incorrect connection of some pressure tabs and an accidental offset in flap angle. Although an attempt is made to correct for these errors, there are still some unexplainable effects which are believed to be caused by a combination of these issues.

- The steady lift curves are under predicted by Q^{3}UIC for both free and tripped transition. However, the free transition curve shows good agreement in the linear region prior to stall. Remarkable is that the free transition measurements compare well with the applied flap correction, whereas for the tripped transition measurements, the flap correction seems to make Q^{3}UIC under predict all lift values. The reason for this remains not fully known.
  By the same reasoning, the unsteady loops show better agreement between experiments and simulations in the free transition cases. Apart from the offset in the

measurements with a tripped boundary layer, the thickness of the loops and the flow reattachment locations are captured to a reasonable extent in most cases.

- The flap measurements in Chapter 6 show a good comparison for the steady lift curves, for both free and forced transition. Also the unsteady effects at lower angles of attack are captured well. However, around the stall angle of attack of approximately 8 degrees and beyond, the Q^{3}UIC results start to show increasingly large deviations from the measurements. Theoretically, the different unsteady Kutta conditions may have a noticeable influence on the flap deflection cases. The Kutta conditions have been checked and did not show a remarkable difference. Nonetheless, it is still possible that an inaccurate implementation or modelling of the unsteady Kutta condition may be the cause of the spurious behaviour of the results for $\alpha = 8°$ and 18°.

In short it can be said that the worst performance of Q^{3}UIC is found in the DU 95-W-180 case for an angle of attack of 8 degrees in, Figures 6.15 and 6.16. The Q^{3}UIC results show separation where neither OpenFOAM nor the measurements seem to agree. This may be caused by the way in which the unsteady Kutta condition is modelled and implemented, further research is needed to confirm this matter. At higher angles of 18 degrees, differences are to be expected, but are still not far off.

OpenFOAM

OpenFOAM, proved to be accurate for the flap measurements, but less so for the pitching airfoil measurements, especially around the stall angle. A point-wise description of the found results is summarised below.

- The pitch experiments of the NACA 64-418 airfoil compare well with the CFD simulations with respect to the steady lift curve. As expected OpenFOAM over predicts the lift values for angles of attack beyond α_{max}. The lower range until the stall angle, shows good overlap with measurements. Modelling the mean angle of attack that corresponds to the stall angle proved to be the most challenging and did not provide accurate results. The loops stay linear and the up and down stroke show a small difference in lift values, whereas the down stroke values should be considerably lower and thus the loops wider. Various factors may have caused this, ranging from the choice of turbulence model to mesh quality or initial conditions specifications. Lack of time and resources prohibited the quest for optimum settings to accurately capture all effects present in the experimental curves.

- A mean angle of attack of 12 degrees, which is beyond the stall angle, shows more accurate results again. So it can be concluded that for a mean angle of attack of 8 degrees, where the boundary layer constantly switches between attached and separated condition, the flow is most difficult to simulate properly.
  An other factor that may have caused the inaccuracy of the results could also be the low Reynolds number of $4.2 \cdot 10^5$ at which the measurements were performed. As the used k-ω SST turbulence model is more suited for higher meshes with $y^+ > 1$, an adapted version, k-ω lowRe is likely to show better results for this study where $y^+ = 1$.

- By changing the upwinding scheme from second to first order, the error would increase but the resulting set of equations should stabilize, possibly resulting in a more accurately resolved boundary layer around the stall angle, especially in the NACA pitching cases.
- For the DU 95-W-180 flap measurements, OpenFOAM shows a more satisfying overlap, except for the highest angle of attack of 18 degrees. As mentioned by Bertagnolio [33], the accuracy and validity of 2D URANS and k-ω SST is acceptable in the lower angle of attack range, however, when the stall angle is exceeded and most of the flow is separated, results deteriorate and more accurate models such as LES or DES should be used.

OpenFOAM worst performance is clearly the DU 95-W-180 case at angle of attack of 18 degrees, Figures 6.17 and 6.16. However, the error is not due to the inability of the solver, but is believed to be caused by an improper reconstruction of the steady state solution. It is likely that the unreconstructed solution is used to initialise the unsteady run. As a result the unsteady solution shows large deviations and does not tend to stabilise.
The other questionable outcomes of OpenFOAM are the NACA 64-418 cases around the stall angle of 8 degrees in Figure 5.14. The one disadvantage of this OpenFOAM version is that, because of the fact the forced transition model has not been fully validated, a free transition comparison could not be made. This study partly aimed at validating the former model such that in future times, free transition can be implemented.

Final thoughts

The final thoughts on the two numerical models can be summarised in a few words. The speed and ease of calculations and change of input settings of Q^{3}UIC is a major advantage compared to OpenFOAM. However it is not possible to analyse the results in the same way as OpenFOAM. The latter provides the user with many more ways of post processing and viewing the generated results in the form of pressure, velocity or turbulent kinetic energy fields. The complexity of OpenFOAM does not ensure the validity of the outcome. A good example of this is the NACA 64-418 case around the mean angle of attack of 8 degrees, where OpenFOAM fails to show accurate results while Q^{3}UIC does not seem to have any difficulties doing this. Moreover, to get correct results for unsteady and separated flow in the URANS OpenFOAM solver, many parameters and settings can be adjusted and tweaked. Due to the relatively long computation times, the results can not be analysed quickly and the whole process takes long, making it difficult to iterate extensively and frequently. A MSc thesis with a duration of a couple of months is not a long enough period of time to satisfyingly accomplish flawless results.

7.2 Recommendations

Unfortunately, not everything could be solved due to the limited time span of the thesis. It is very likely that with more time, results can be obtained that follow experiments more closely. A brief list of possible advise for future studies is presented below.

- To generate more accurate results with Q^{3}UIC the first advice that arises is to have a look at the improvement of implementing the unsteady Kutta condition. Especially for the flap deflection cases this is likely to provide better results.
- To test Q^{3}UIC for reduced frequencies beyond $k = 0.1$ it is advisable to perform a measurement campaign with higher reduced frequencies than has previously been done.
- An interesting validation method would be to do measurements on a coupled motion between main airfoil and flap, with different phase delays between the two.
- More iterations, changing Q^{3}UIC settings like unsteady Kutta condition and time step variations.
- In order to get more reliable results in OpenFOAM it is advisable to try different turbulence models. k-ω SST is preferred over k-ε due to its better capability to solve boundary layer scale phenomena. Various versions of this model exist which are likely to perform better than the one used in this study. Low Re turbulence models or models that sustain the turbulent inflow parameters exist and are advised to use in similar studies in unsteady flow conditions with separated flow regions.
- Apart from changing turbulence models, it is recommended to look into the effect of changing discretisation schemes from second to first order upwind. Although this may increase the error, it can result in more stable outcomes. The present study did not focus on these specific details, but it is not unthinkable results could in a sense be improved by spending more time and resources into additional research.
- CFD modelling of the flow in the stalled region is challenging because the flow is inherently 3D and can not be modelled accurately using RANS. A LES approach should generally be able to show better results. On the other hand, LES is computationally too expensive to model this type of flow conditions. So depending on the situation a choice has to be made between these two solvers.

Bibliography

[1] John D. Anderson. *Fundamentals of Aerodynamics*. McGraw–Hill, 2001.

[2] Joseph Katz and Allen Plotkin. *Low Speed Aerodynamics*. McGraw–Hill, 1991.

[3] Frank M. White. *Viscous Fluid Flow*. McGraw–Hill, 2006.

[4] Néstor Ramos García. *Unsteady Viscous-Inviscid Interaction Technique for Wind Turbine Airfoils*. PhD thesis, Technical University of Denmark, 2011.

[5] Prof. dr. G.J.W. van Bussel. AE4W21 Wind Turbine Aeroelasticity - Lecture 5. University Lecture TU Delft, 2013.

[6] Sirko Bartholomay. *Implementation of aeroservoelastic effects into a two dimensional unsteady panel code and experimental validation*. Master's thesis, Technische Universität Dresden, 2013.

[7] L.L.M. Veldhuis. *Manual for Windtunnel Test AE2209*. Delfy University of Technology, January 2012.

[8] Adam M. Wickenheiser and Ephrahim Garcia. Aerodynamic modeling of morphing wings using an extended lifting-line analysis. *JOURNAL OF AIRCRAFT*, 44(1):10–16, JAN-FEB 2007.

[9] S. Barbarino, O. Bilgen, R.M. Ajaj, M.I. Friswell, and D.J. Inman. A review of morphing aircraft. *Journal of Intelligent Material Systems and Structures*, 22(9):823–877, 2011.

[10] A.M.O. Smith. High-Lift Aerodynamics. *JOURNAL OF AIRCRAFT*, 12(6):501–530, JUNE 1975.

[11] A.Y.N. Sofla, S.A. Meguid, K.T. Tan, and W.K. Yeo. Shape morphing of aircraft wing: Status and challenges. *Materials and Design*, 31(3):1284–1292, 2010.

[12] C. Thill, J. Etches, I. Bond, K. Potter, and P. Weaver. Morphing skins. *Aeronautical Journal*, 112(1129):117–139, 2008. cited By (since 1996)128.

[13] Stephen Daynes and Paul M Weaver. A morphing trailing edge device for a wind turbine. *Journal of Intelligent Material Systems and Structures*, 23(6):691–701, 2012.

[14] Leonardo Bergami, Vasilis A. Riziotis, and Mac Gaunaa. Aerodynamic response of an airfoil section undergoing pitch motion and trailing edge flap deflection: a comparison of simulation methods. *Wind Energy*, 2014.

[15] R. Pereira et al. Validation of the Beddoes-Leishman Dynamic Stall Model for Horizontal Axis Wind Turbines using MEXICO data. *Wind Energy*, 16(2):207–219, 2013.

[16] Amanullah Choudry et al. An insight into the dynamic stall lift characteristics. *Experimental Thermal and Fluid Science*, 58:188–208, 2014.

[17] M. La Mantia et al. Unsteady panel method for flapping foil. *Engineering Analysis with Boundary Elements*, 33(4):572–580, 2009.

[18] J.L. Hess. Panel methods in computational fluid dynamics. In *Annual Review Fluid Mechanics*, volume 22, pages 255–274, 1990.

[19] J. Sodja. Turbulence models in CFD, March 2007. University of Ljubljana, Faculty for mathematics and physics.

[20] G. Nader et al. Characterization of low turbulence wind tunnel, September 2006. XVIII IMEKO World Congresss, Rio de Janeiro Brazil.

[21] Pressure system. http://www.meas-spec.com/product/t_product.aspx?id=9311. Accessed: September 2014.

[22] W. Timmer and van R. Rooij. Summary of the Delft University Wind Turbine Dedicated Airfoils. *Journal of Solar Energy Engineering*, 125:488–496, 2003.

[23] Dr. ir. L.L.M. Veldhuis. AE4130 Aircraft Aerodynamics - Part I. University Lecture TU Delft, 2013.

[24] B.C. Basu and G.J. Hancock. The unsteady motion of a two-dimensional aerofoil in incompressible inviscid flow. *ournal of Fluid Mechanics*, 87(1):159–178, 1978.

[25] Aung Myo Thu et al. Dynamic Stall Formation of OA-209 Airfoil at Low Reynolds Number. *International Journal of Mechanical, Aerospace, Industrial and Mechatronics Engineering*, 8(2):277–280, 2014.

[26] T. Gillebaart. *Influence of flexibility on the clap and peel movement of the DelFly II.* Master's thesis, TU Delft, September 2011.

[27] F.R. Menter. Two-Equation Eddy-Viscosity Turbulence Models for Engineering Applications. *AIAA Journal*, 32(8):1598–1605, 1994.

[28] C.L. Rumsey et al. Turbulence Model Behavior in Low Reynolds Number Regions of Aerodynamic Flowfields. In *38th AIAA Fluid Dynamics Conference and Exhibit*, 2008. Seattle, WA.

[29] Turbulence model k-ω SST. http://turbmodels.larc.nasa.gov/sst.html. Accessed: 2014-07-10.

[30] Richardson Extrapolation. http://www.math.washington.edu/~greenbau/Math_498/lecture04_richardson.pdf. Accessed: 2May 2014.

[31] J. Selle. *Study on the effectiveness of turbulator tape on boundary-layer transition*, May 1999. University of California at Davis, Department of Mechanical and Aeronautical Engineering.

[32] Initiall cell size and y^+. http://www.pointwise.com/yplus/. Accessed: May 2014.

[33] Franck Bertagnolio. *Numerical Study of the Static and Pitching Risø-B1-18 Airfoil*. Technical report, RisøNational Laboratory, Roskilde, Denmark, January 2014.

Appendix A

Free LTT flap measurements at $\alpha = 10°$

For the case with a free transition of the boundary layer from a laminar to a turbulent state, the stall angle of attack was determined to be $\alpha = 10°$. Therefore, an extra set of unsteady measurements is carried out. This angle of attack is not simulated, nor is it measured in the forced transition.

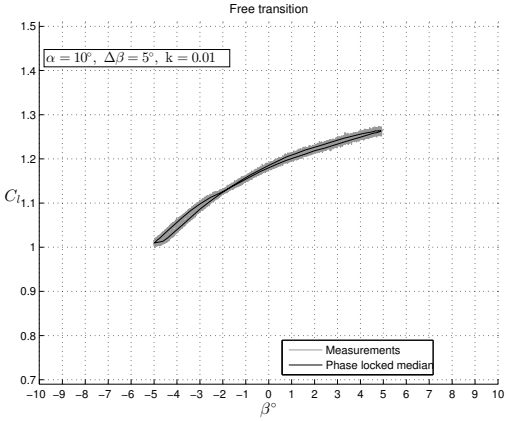

(a) Free transition, $\alpha = 10°, \Delta\beta = 5°, k = 0.01$.

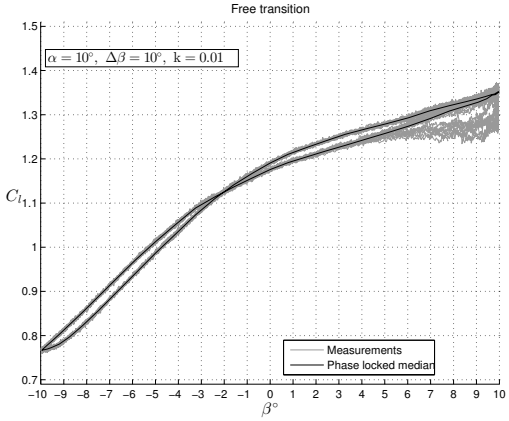

(b) Free transition, $\alpha = 10°, \Delta\beta = 10°, k = 0.01$.

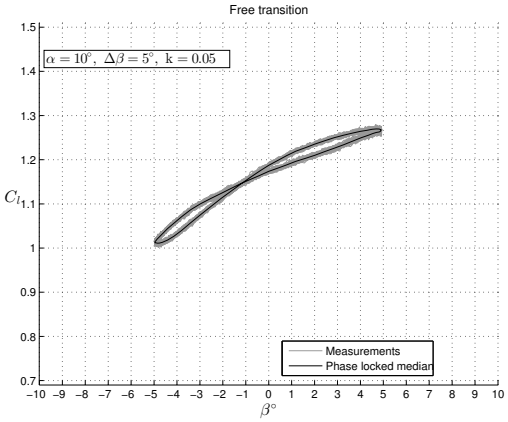

(c) Free transition, $\alpha = 10°, \Delta\beta = 5°, k = 0.05$.

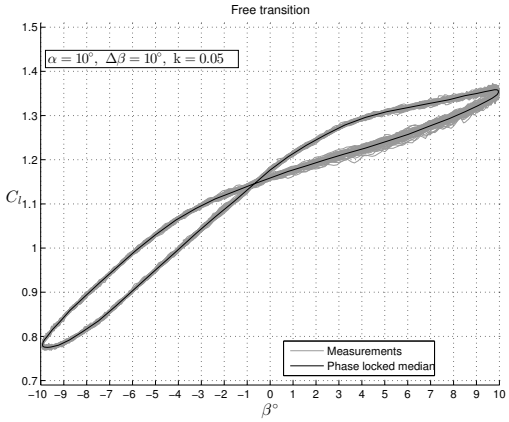

(d) Free transition, $\alpha = 10°, \Delta\beta = 10°, k = 0.05$.

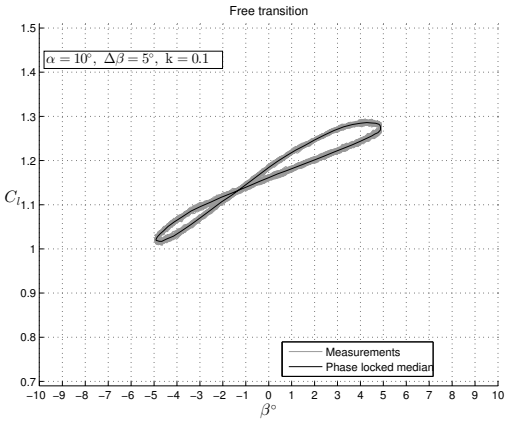

(e) Free transition, $\alpha = 10°, \Delta\beta = 5°, k = 0.10$.

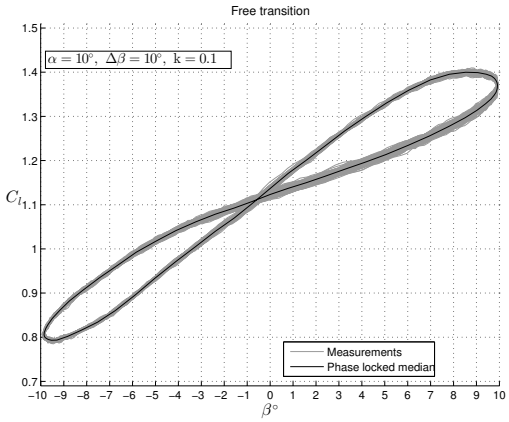

(f) Free transition, $\alpha = 10°, \Delta\beta = 10°, k = 0.10$.

Figure A.1: *$C_l(\beta)$ for $\alpha = 10°, \Delta\beta = 5°$ and $10°$, $k = 0.01, 0.05$ and 0.10. $Re = 10^6$*